Electrochemical Analysis of Natural Aqueous Media



Yanjun Guo

St Johns' College

Supervised by

Professor Richard Compton

A thesis submitted for the degree of
Doctor of Philosophy
in Physical and Theoretical Chemistry

Trinity Term 2021

Acknowledgements

First of all, I would like to express great thanks to my supervisor, Professor Richard Compton, for his exceptional guidance, encouragement and thoughtfulness throughout my DPhil study. Thank you for providing me invaluable opportunities to build up my research skills and confidence in the difficulties. Your enthusiasm for science and positive views deeply influenced me.

Second, my sincere appreciation goes to Dr Christopher Batchelor-McAuley for your generous support and constructive advice which significantly contributed to my study. I would also like to express my thank to Jake (Dr Minjun Yang) and Collin (Dr Ruo-chen Xie) who were such helpful senior group members and friends of mine.

Thirdly, I would like to thank all the Compton Group Members (2018-2021). To Yuanzhe and Ruiyang, it has been so lucky for me to have you going through milestones of the Dphil together. To Archana, Yuanyuan, Yifei, Haotian, Korbua, Lifu, Alex, Rapheal, Bertold, Enno and many other group members of the past and present, it is truly enjoyable to work in such a wonderful and warm group with you.

In particular, I want to thank Danlei (Dr Danlei Li) and Xin (Dr Xin Chang) who are trustable and reliable friends of mine living with me for my Dphil period. The memories with you are priceless and life-changing to me.

Finally, I deeply thank my family for their endless caring, support and love. Thank you for offering such a great experience to me that is extraordinary meaningful and valuable. I become stronger now for the next step.

Table of Contents

Acknowledgements i
Abstract vi
Glossary viii

Chapter 1
Introduction to Electrochemistry 1
1.1 Electrochemical Equilibrium 1
1.2 Electrode Kinetics 7
1.3 Mass Transport 15
1.3.1 Diffusion 15
1.3.2 Convection 18
1.3.3 Migration and Electrical Double Layer 18
1.3.4 Weakly Supported Systems 22
1.4 Electrochemical Methods 24
1.4.1 The Electrochemical Cell 24
1.4.2 Cyclic Voltammetry 26
Bibliography 33
Chapter 2
The Strategy of Natural Waters Analysis 35
2.1 Inorganic Compositions of Seawater and Drinking Water 35
2.2 Research Scope 38
2.3 Key Reactions 40
Bibliography 44
Chapter 3
Methodology 46
3.1 Chemical Reagents and Instruments 46
3.2 Simulation Programs 50
Bibliography 50

Chapter 4

The Oxygen Reduction Reaction at Silver Electrodes in High Chloride Media and the Implications for Silver Nanoparticle Toxicity 51

4.1 Introduction 52

4.2 Experimental 57

4.2.1 Chemical Reagents 57

4.2.2 Electrochemical Analysis 57

4.2.3 Oxygen Reduction Reaction on Macro-electrodes 58

4.3 Results and Discussions 58

4.3.1 O_2 Reduction on Glassy Carbon Electrodes 58

4.3.2 O_2 Reduction on Silver Electrodes 61

4.3.3 Physicochemical Origins of the Peak Splitting 73

4.3.4 Implications for Silver Nanoparticle Toxicology 76

4.4 Conclusions 77

Bibliography 77

Chapter 5

A Bespoke Chloride Sensor for Seawater: Simple and Fast with A Silver Electrode 80

5.1 Introduction 81

5.2 Experimental 85

5.2.1 Chemical Reagents 85

5.2.2 Electrochemical Analysis 86

5.3 Results and Discussions 88

5.3.1 Scan Rate Study of AgCl Formation and Stripping Peaks 91

5.3.2 Chloride Determination in NaCl Solutions 93

5.3.3 Chloride Level Determination in Synthetic Seawater 100

5.3.4 Chloride Level Determination in Natural Seawater 104

5.4 Conclusions 106

Bibliography 106

Chapter 6

Metal Deposition and Stripping under Self-supported Conditions: Experiment and Simulation 109

6.1 Introduction 110
6.2 Experimental 112
6.3 Theory 113
6.3.1 Nernst Plank Poisson (NPP) Equations 115
6.3.2 Boundary Conditions 116
6.3.3 Numerical Methods 118
6.4 Results and Discussions 119
6.5 Conclusions 131
Bibliography 133
Chapter 7 135
A Bespoke Chloride Sensor for Mineral Water 135
7.1 Introduction 135
7.2 Experimental 139
7.2.1 Chemical Reagents 139
7.2.2 Electrochemical Analysis 139
7.2.3 Chloride Detection on A Silver Macro-electrode 140
7.2.4 Chloride Detection with Silver Nanoparticles on a GC Electrode 141
7.3 Results and Discussions 141
7.3.1 Voltammetry under 'Self-support' and 'Low support' Conditions 142
7.3.2 Chloride Determination in Pure KCl Solutions and Tesco Mineral Water KCl Solutions (Tesco-KCl Solutions) 146
7.3.3 Chloride Determinations in Tesco-KCl Solutions Using Silver Nanoparticle Modified Electrodes 149
7.3.4 Chloride Determination in Real Samples 152
7.4 Conclusions 153
Bibliography 155
Chapter 8
Conclusions 156
Appendix A 159
Section 1 Calibration of Electrodes 159

Section 2 Seawater Composition, Oxygen Solubilities and Diffusion Coefficients.....160
Section 3 Oxygen Reduction Reaction on Silver Electrode in KNO_3 and $NaClO_4$.....163
Section 4 Oxygen Reduction Reaction on Silver Electrode in Seawater.....164
Section 5: Digisim Fitting of Oxygen Reduction Reaction on Silver in Synthetic Seawater 165
Section 6: Oxygen Reduction Reaction on Silver in 0.1 M KCl and 0.42 M KCl 166
Appendix B 168
Section 1: The Calibration of the Silver Electrode 168
Section 2 Monolayer Peaks of Silver Chloride.....170
Section 3 The Superoxide Peak Studied in Synthetic Seawater 171
Appendix C 173
Section 1 The Superimposed Voltammetry 173
Section 2 The Simulation Stripping Peak Potential Variation under Different Support Ratios 174

Abstract

This thesis focuses on investigations of electroanalytical methods to study natural aqueous media particularly considering analyte quantification with high chloride levels (seawater) or low electrolyte concentrations (drinking water). The two extremes correspond to different voltammetric regimes where high ionic strength suppresses transport via ionic migration and the voltammetry is said to be 'fully supported' and mass transport is dominated by diffusion, whilst in the near absence of electrolyte diffusion is strongly coupled with migration.

The fundamentals of electrochemistry and the principles of electrochemical methods used in this thesis are introduced in **Chapter 1**. The chemistry of natural water is discussed in **Chapter 2**. Experimental methods and non-electrochemical based techniques including simulation software are described in **Chapter 3**.

The investigations of seawater and drinking water each consist of two chapters. In the study of seawater, **Chapter 4** suggests the possible toxicity of silver nanoparticles in seawater is assessed in the light of studies of the oxygen reduction reaction on a silver electrode where the toxic superoxide was found to be produced as a reaction intermediate with a lifetime on the voltammetric timescale in seawater media. **Chapter 5** builds on the work in **Chapter 4** to realise a bespoke chemical sensor for chloride in seawater based on anodic stripping voltammetry of silver chloride in the very high ionic strength seawater medium.

On the other hand, the research in drinking water aims to sketch a methodology of chloride quantification to overcome current challenges in performing electrochemical experiments under low ionic strength conditions without the addition of extra electrolytes. Prior to sensor development, some fundamental studies were undertaken to characterise stripping voltammetry under low ionic strength conditions. First, the simulation and experimental investigation of the

deposition and stripping voltammetry from ideal fully supported conditions (with a ratio of electrolyte concentration to analyte concentration ~100) to weakly support (electrolyte concentration: analyte concentration <100) and even self-support conditions (in absence of any supporting electrolyte) is discussed in **Chapter 6**. Then, deposition and stripping voltammetry is used in chloride analysis in self-support mineral water solution without added reagents (**Chapter 7**)

Glossary

Table G.1 Roman Symbols

Symbol	Interpretation	Units
A	oxidised form of system $A^{z}_{(aq)} + e^{-}_{(m)} \rightleftharpoons B^{z-1}_{(aq)}$	-
$\boldsymbol{A_{electrode}}$	electrode area	M
$\boldsymbol{a_i}$	activity of species i	-
	coefficient for the polynomial salinity equation	-
B	reductive form of system $A^{z}_{(aq)} + e^{-}_{(m)} \rightleftharpoons B^{z-1}_{(aq)}$	-
$\boldsymbol{c_i}$	concentration of species i	mol m^{-3}
$\boldsymbol{C_i}$	dimensionless concentration	-
$\boldsymbol{c^0}$	the standard concentration	1×10^{-3} mol m^{-3}
$\boldsymbol{c_{i,0}}$	surface concentration of i	mol m^{-3}
$\boldsymbol{c_{i,bulk}}$	bulk concentration of i	mol m^{-3}
Cl	Chlorinity	g kg^{-1}
$\boldsymbol{D_i}$	diffusion coefficient	m^2 s^{-1}
$\boldsymbol{d_i}$	dimensionless diffusion coefficient	-
$\boldsymbol{E}$	applied potential	V
$\boldsymbol{E^o_f}$	formal potential	V
$\boldsymbol{E^o}$	standard potential	V
$\boldsymbol{E_{1/2}}$	half-wave potential	V
$\boldsymbol{F}$	Faraday constant	96,485 C mol^{-1}
$\boldsymbol{G}$	Gibbs energy	kJ mol^{-1}
$\triangle \boldsymbol{G^{\dagger}}$	standard Gibbs energy of activation	kJ mol^{-1}
$\boldsymbol{I_i}$	electrical current	A
$\boldsymbol{I_p}$	peak current	A
$\boldsymbol{I_{ss}}$	steady-state current	A
$\boldsymbol{I_{D,ss}}$	steady-state current under diffusion control system	A
i	Index	-
	a random species	-
$\boldsymbol{J_i}$	molar flux of i though a unit area	mol m^{-2} s^{-1}
$\boldsymbol{J_{m,i}}$	migratory flux	mol m^{-2} s^{-1}
$\boldsymbol{J_{d,i}}$	diffusional flux	mol m^{-2} s^{-1}

Table G.1 (continued).		
$\boldsymbol{K_{15}}$	conductivity ratio	-
K_0	dimensionless electrochemical rate constant	-
$\boldsymbol{k_0}$	standard electrochemical rate constant	m s^{-1}
$\boldsymbol{k_c}$	rate constants of the cathodic process	m s^{-1}
$\boldsymbol{k_a}$	rate constants of the anodic process	m s^{-1}
k_{MT}	mass transport coefficient	m s^{-1}
k_{HET}	heterogeneous rate constant	m s^{-1}
M	molecular or atomic mass of the deposited solid	g mol^{-1}
N	number of spherical nanoparticles	
$\boldsymbol{n_{eff}}$	effective number of electrons	-
$\boldsymbol{P_i}$	partial pressure	N m^{-2}
$\boldsymbol{P^0}$	standard pressure	$\sim 10^5$ N m^{-2}
$\boldsymbol{R}$	gas constant	8.315 J K^{-1} mol^{-1}
	Space coordinate	-
R_s	expending grids	-
$\boldsymbol{R_e}$	Debye length to radius ratio	-
$\boldsymbol{r}$	electrode radius	M
r'	space coordinate	M
S	Salinity	g kg^{-1}
$\boldsymbol{T}$	absolute temperature	K
	dimensionless experimental time	-
t	Time	S
X	dimensionless deposited layer thickness	-
X_{ML}	dimensionless thickness of a single monolayer	-
$\boldsymbol{x}$	distance	M
$\boldsymbol{x_{DL}}$	Debye length	M

Table G.2 Greek Symbols

Symbol	Interpretation	Units
α	electron transfer coefficient of reduction	-
β	electron transfer coefficient of oxidation	-
Γ_i^0	surface coverage of reactant at the electrode surface	-
γ_i	activity coefficient	-
ε_0	permittivity of the free space	F m^{-1}
ε_s	relative permittivity of the solution	F m^{-1}

Table G.1 (continued).		
Θ	dimensionless electrode potential	-
Λ	Matsuda and Ayabe parameter	
μ_i	chemical potential	kJ mol^{-1}
μ_i^o	standard chemical potential of species i	kJ mol^{-1}
$\bar{\mu}_i$	electrochemical potential	kJ mol^{-1}
σ	dimensionless scan rate	-
$\sigma(X)$	surface coverage	-
ν	scan rate	V s^{-1}
ρ	density of the deposited solid	g m^{-3}
Φ	dimensionless electrostatic potential	-
ϕ (V)	electrostatic potential	V
χ	deposited layer thickness	M

Table G.3 Abbreviations

Abbreviations	**Interpretation**
AgNPs	silver nanoparticles
aq	Aqueous
CE	counter electrode
CV	cyclic voltammetry
GC	glassy carbon
HOMO	The highest occupied molecular orbital
IHP	Inner Helmholtz Plane
LUMO	the lowest unoccupied molecular orbital
OHP	Outer Helmholtz Plane
ORR	Oxygen reductive reaction
RDS	rate-determining step
RE	reference electrode
ROS	reactive oxygen species
SCE	saturated calomel electrode
SHE	standard hydrogen electrode
Sup	supporting electrolyte
WE	working electrode

Chapter 1

Introduction to Electrochemistry

Electrochemical analysis has been widely applied in fundamental studies and sensor developments in medical, biological and geochemical studies with distinct advantages in accuracy, portability and cost-efficiency. Before introducing the research scope and featured reactions, this chapter provides some key concepts in electrochemistry relevant to subsequent studies, covering aspects from electrochemical equilibrium, kinetics and mass transport to overviews of electrochemical processes and practical methods.

1.1 Electrochemical Equilibrium

Electrochemistry monitors the interplay of electrical and chemical effects on the electron transfer process at the interface between chemical phases, usually an electrode and the electrolyte.[1]

When a metal electrode is inserted in the aqueous solution of A and B, the electrode may serve as a *source* or *sink* of electrons to promote the redox reaction at the solution-electrode interface.[2, 3] An electrochemical equilibrium may be established at the electrode surface as in **Equation 1.1**.

$$A^{z}_{(aq)} + e^{-}_{(m)} \rightleftharpoons B^{z-1}_{(aq)} \qquad \textbf{(1.1)}$$

where A^z and B^{z-1} comprise a one-electron redox couple in an aqueous solution and the electron comes from the metal electrode.

\\\

The equilibrium in **Equation 1.1** implies that the rate of A^z obtaining an electron, being *reduced* into B^{z-1} and that of B^{z-1} releasing an electron, being *oxidized* backwards to A^z is identical.

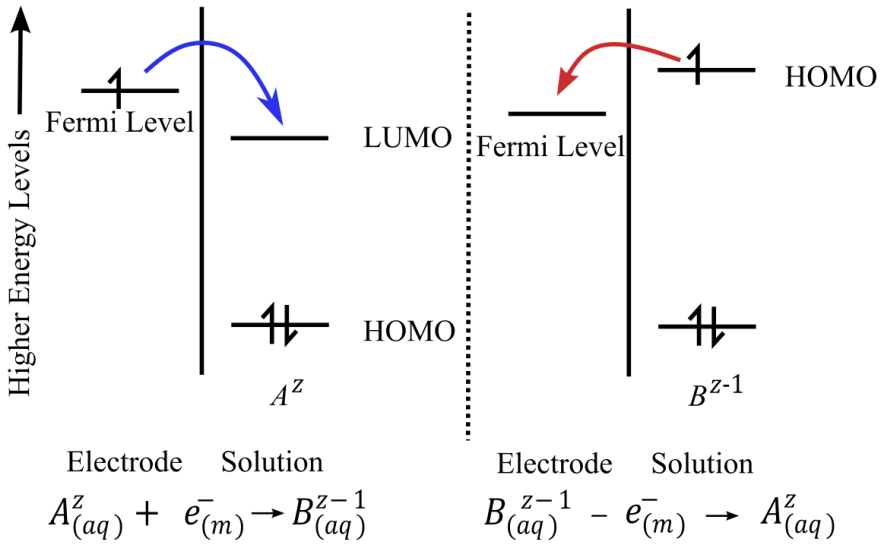


Figure 1.1 Energy levels (not to scale) during reduction of A^z (left) and oxidation of B^{z-1} (right) in the solution.

From a thermodynamic point of view, the equilibrium in **Equation 1.1** can be illustrated as the energy levels balancing at the electrode/solution interface.[1] The continuum energy levels of the electrode, assumed metallic, consist of electronic conduction bands and have an energy maximum known as the Fermi level. In contrast, discrete energy levels are associated with the redox couple in the solution phase due to an unfilled molecular orbital. Consider when the Fermi level is higher than the lowest unoccupied molecular orbital (LUMO) of A^z, as described in the left side of **Figure 1.1**. Consequently, the electron transfer process from the electrode surface to A^z is thermodynamically favourable. At the same time the reduction of A^z decreases the energy level of the electrode as a result of the latter gaining a negative charge from the transferred electron. When the Fermi level is lower compared to the highest occupied molecular

orbital (HOMO) of B^{z-1}, an electron of B^{z-1} can be transferred to the electrode side, in which way B^{z-1} is oxidized into A^z. If the Fermi energy of the electrode sits between the LUMO of A^z and HOMO of B^{z-1}, the reaction in both directions is thermodynamically favourable. Once the kinetic rates for both reduction and oxidation reactions are also identical, the dynamic electrochemical equilibrium can be achieved. Under such a condition, a zero net number of electrons are transferred and the difference in concentrations of $A^z$and B^{z-1} as compared to that before the electrode presented in the solution is negligible since only a little charge transfer is needed to attain equilibrium. Once this is reached there is a charge separation established at the interface and the charge separation between the solution phase and electrode at the point of equilibrium results in a potential difference from which the electrode potential originates.

The electrochemical equilibrium position depends on both chemical and electrical energies. To describe such a process, the electrochemical potential is defined with two terms.

$$\bar{\mu}_i = \mu_i + z_i F\phi \qquad \textbf{(1.2)}$$

where for species i, $\bar{\mu}_i$ is the electrochemical potential, μ_i is the chemical potential, z_i stands for the charge on i, F is the Faraday constant (96485 C mol^{-1}) and ϕ is the potential of the phase of interest.

The first term μ_i describes the chemical potential (molar Gibbs Energy) and the second term $z_i F\phi$ accounts for the electrical energy per mole to match the units of the first term (Gibbs energy per mole). Under constant temperature and pressure, the electrochemical potential for the reactants equals that of the products if the equilibrium is reached and such a system can be analysed with **Equation 1.2**.

For the system stated in **Equation 1.1**, the electrochemical potentials can be described as **Equation 1.3**.

$$\bar{\mu}_{A^z} + \bar{\mu}_{e^-} = \bar{\mu}_{B^{z-1}} \quad \textbf{(1.3)}$$

Therefore,

$$(\mu_{A^z} + zF\phi_s) + (\mu_{e^-} - F\phi_m) = [\mu_{B^{z-1}} + (z-1)F\phi_s] \quad \textbf{(1.4)}$$

where ϕ_s and ϕ_m are the potentials of the solution and the electrode respectively.

The equation can be rearranged into:

$$F(\phi_m - \phi_s) = \mu_{A^z} + \mu_{e^-} - \mu_{B^{z-1}} \quad \textbf{(1.5)}$$

The terms of chemical potential follow the expression:

$$\mu_i = \mu_i^o + RTln(\frac{c_i}{c^0}) \quad \textbf{(1.6)}$$

where μ_i^o stands for the standard chemical potential of species i, R is the gas constant with a value of 8.315 J K^{-1} mol^{-1}, T is the absolute temperature in K, c_i is the concentration of species i in mol dm^{-3} and c^0 is the standard concentration (1 mol dm^{-3}).

For A^z and B^{z-1}, the chemical potentials are:

$$\mu_{A^z} = \mu_{A^z}^o + RTln(\frac{c_{A^z}}{c^0}) \quad \textbf{(1.7)}$$

$$\mu_{B^{z-1}} = \mu_{B^{z-1}}^o + RTln(\frac{c_{B^{z-1}}}{c^0}) \quad \textbf{(1.8)}$$

Thus, the **Equation 1.5** becomes:

$$(\phi_m - \phi_s) = \frac{\triangle\mu^o}{F} + \frac{RT}{F} ln(\frac{c_{A^z}}{c_{B^{z-1}}}) \quad \textbf{(1.9)}$$

where $\triangle \mu^o = \mu^o_{A^z} + \mu_{e^-} - \mu^o_{B^{z-1}}$ (**1.10**)

The term $\triangle \mu^o$ can be considered as a constant when temperature and pressure are both fixed. In particular, **Equation 1.9** shows the form of the Nernst equation which indicates the position of electrochemical equilibrium of A^z / B^{z-1} at the interface, and quantifies the potential differences between the *solution* phase and the solid phase (*the electrode*). If a *gaseous* species i with a partial pressure P_i is involved in the reaction, a standard pressure P^0, ($\sim 10^5$ N m^{-2}) will be used instead of the standard concentration c^0 (1 mol dm^{-3}) in **Equations 1.7** and **1.8**. For pure solid and liquid compounds, the term regarding concentrations or pressures is eliminated and their chemical potential equals the standard potential of the materials.

Notice that **Equation 1.9** is only possible in limited cases where the solutions are ideal where the forces in ion-ion and ion-solvent interactions are similar for both A and B. Non-ideality arises from the difference in inter-particular forces for charged particles, especially when at high concentration.[3] To thermodynamically quantify equilibrium under non-ideal conditions concentrations need to be replaced by activities viz the 'effective' concentration of each component.

$$a_i = \gamma_i c_i \quad \textbf{(1.11)}$$

where a_i is the activity of species i, evaluated from the product between the activity coefficient γ_i and the concentration of i. The equation implies that the solution approaches ideality when the coefficient γ_i is close to 1.

More generally Equation 1.9 becomes **Equation 1.12**.

$$(\phi_m - \phi_s) = \frac{\triangle \mu^o}{F} + \frac{RT}{F} ln(\frac{\gamma_{A^z} c_{A^z}}{\gamma_{B^{z-1}} c_{B^{z-1}}}) \quad \textbf{(1.12)}$$

The Nernst equation now quantifies the electrochemical equilibrium in non-ideal solutions. However, it can only provide *theoretical* estimations of the interfacial potential difference. To perform an experimental measurement, another interface with constant compositions in both phases (a *reference* electrode) is required. Both electrodes need to be connected to a digital voltammeter ('DVM') so that the circuit is closed. Usually, the reference electrodes can be classified into two types, the primary reference electrode which serves as the universal standard in electrochemistry and, the secondary reference electrode which can be applied conveniently in experimental operations.[4]

With any types of reference electrodes, the measured potential difference as recorded on a DVM can be described as:

$$E = (\phi_m - \phi_s)_{test} - (\phi_m - \phi_s)_{reference} \quad \textbf{(1.13)}$$

where $(\phi_m - \phi_s)_{reference}$ is a constant.

In particular, if the reference is the primary reference electrode ie. the standard hydrogen electrode (SHE), the standard electrode potential of the redox couple A^z / B^{z-1} can be determined as E^o. If the value of each ion concentration results in unity in their activities, the natural logarithm term vanishes so that the standard potential can be measured as E^o in **Equation 1.14**.

$$E = E^o + \frac{RT}{F} ln(\frac{\gamma_{A^z} c_{A^z}}{\gamma_{B^{z-1}} c_{B^{z-1}}}) \quad \textbf{(1.14)}$$

where E is measured against SHE, and E^o is the standard electrode potential of A^z/B^{z-1} couple.

The standard electrode potential reflects the Gibbs energy change of the system measured against the SHE. Therefore it has a thermodynamic generality under a constant temperature and pressure regardless of the species concentrations in the solution. In practice, however, it is

still difficult to determine the value of the activity coefficient of a species i of a certain concentration. To avoid this uncertainty the formal potential (E_f^o) is introduced, combining both terms of E^o and activity coefficients

$$E_f^o = E^o + \frac{RT}{F} ln(\frac{\gamma_A{}^z}{\gamma_B{}^{z-1}}) \quad \textbf{(1.16)}$$

The formal potential depends on the temperature, pressure, and concentration of any electrolyte present in the solution where the electrode is immersed in. With the concept of formal potential, the experimental measurement of potential difference can be directly correlated to the concentration of analyte in the reaction of interest.

$$E = E_f^o + \frac{RT}{F} ln(\frac{c_A{}^z}{c_B{}^{z-1}}) \quad \textbf{(1.17)}$$

The value of formal potentials can be approximated from that of the corresponding standard electrode potentials. For aqueous media, values of E^o are measured under a *standard* solution with pH = 0 at 298 K.[2, 5] Under the same temperature, any difference in pH value can induce a change in formal potentials by 0.059 V per pH unit for a single electron transfer process. Moreover, the above derivation of E_f^o assumed the establishment of electrochemical equilibrium and hence fast kinetics for both directions of reaction. The factors controlling electrode kinetics are discussed in the next sections.

1.2 Electrode Kinetics

Electron transfer at the electrode/solution interface leads to the establishment of dynamic equilibrium and electrode potential as discussed in the previous sub-section. To quantitively rationalize the dynamics of such interfacial processes, the theory of electrode kinetics has been developed in several classic models regarding concentrations and potentials as variables.[1] In

this section, two of the most fundamental bases of electrochemistry, the *Butler-Volmer model* and the *Tafel law* will be discussed.

The analysis of electrode kinetics started from quantifications of the current established at the electrochemical interface. Consider a simplified example where A^z is reduced into B^{z-1} via a single electron transfer process in the aqueous solution in the presence of a metal electrode.

$$A^z_{(aq)} + e^-_{(m)} \underset{k_a}{\overset{k_c}{\rightleftharpoons}} B^{z-1}_{(aq)} \quad \textbf{(1.18)}$$

where k_c and k_a are the heterogeneous rate constants of the cathodic and the anodic process respectively.

The electron transfer from the electrode surface to A^z forming B^{z-1} proceeds via quantum mechanical tunneling. Therefore, substrates such as A *must* first diffuse from the bulk solution to a location within 10~20 Å of the electrode surface constrained by the distances over which electrons can tunnel. Consequently, an electrical current is generated through the electrode, which can be determined as **Equation 1.19**.

$$I_i = FA_{electrode}J_i \quad \textbf{(1.19)}$$

where the footnote i stands for any substrate in the electrochemical reaction. I refers to the current that passes through the electrode, F refers to the Faraday constant, $A_{electrode}$ refers to the area of the electrode in m^2 and J_i is the flux of reactant. The latter represents a measure of the interfacial reaction rate of electron transfer to or from species i. By introducing an electrode kinetic rate law, the flux can be expressed as:

$$J_i = k_n c_{i_0}^n \quad \textbf{(1.20)}$$

where n is the order of reaction regards to species i, k_n is the rate constant of 'n'th order reaction and the subscript 0 refers to the concentration of i within the electron tunnelling distance (the *surface concentration*) the magnitude of which is usually different from that in the bulk solution due to depletion due to the electrode reaction and the limitations of mass transport.

For the reaction in **Equation 1.18**, the ***net*** flux can be written as

$$J = k_c c_{A^z,0} - k_a c_{B^{z-1},0} \quad \textbf{(1.21)}$$

where k_c and k_a are rate constants for the cathodic and anodic reactions respectively.

In most cases, the solution phase reaction rate constant is temperature dependant such that ln k varies linearly with $\frac{1}{T}$. The general expression for the electrochemical rate constant follows the Arrhenius Equation, where the rate constant is the product of the probability of a species overcoming the energy barrier to form the product with the available thermal energy and the frequency with which this is attempted.

$$k_c = A_c \exp\left(-\frac{\triangle G_c^{\dagger}}{RT}\right) \quad \textbf{(1.22)}$$

$$k_a = A_a \exp\left(-\frac{\triangle G_a^{\dagger}}{RT}\right) \quad \textbf{(1.23)}$$

where the subscript indicates the direction of the reaction, A is the frequency factor, $\triangle G^{\dagger}$ indicates the thermal energy (*activation energy*) required to surmount the energy barrier, such that the product can be formed following the attainment of the transition state located at the energy maximum between the reactants and products.

The need for activation energy is illustrated in the energy profile alongside the reaction progress (**Figure 1.2**) where the idea of the *transition state theory* is introduced. As reaction processes, the reactant proceeds through a well-defined activated complex at the maximum (†) if $\triangle G_c^{\dagger}$ or $\triangle G_a^{\dagger}$ are supplied. The transition state species may decay into either A^z or B^{z-1} as described in more advanced theories via a transmission coefficient.

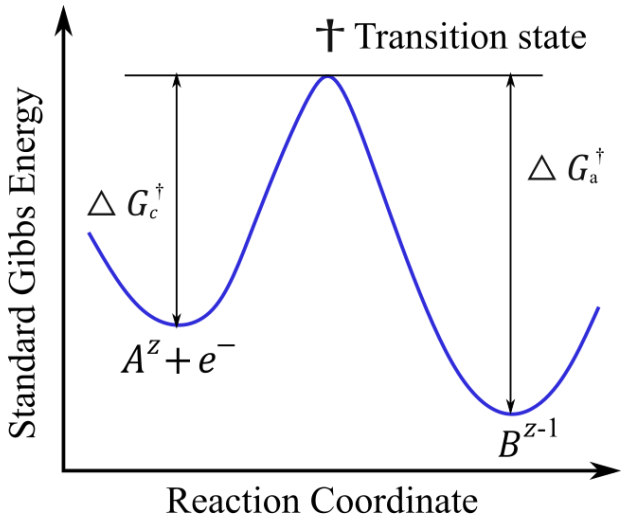


Figure 1.2 Gibbs energy profile (not to scale) during a single electron transfer electrochemical reaction between A^z and B $^{z-1}$.

As discussed in **Section 1.1**, the sum of the electrochemical energy in the reactants or products relates to the potential difference at the interface. Therefore, the activation energy in an electrochemical reaction can be related to and expressed as a function of the interfacial potential difference compared to a standard reference, usually the formal potential E_f^0. The effect of a shift in the potential from the formal potential to a more positive value of the electrode potential *E* for an arbitrary one-step single electron transfer process is depicted in **Figure 1.3**.

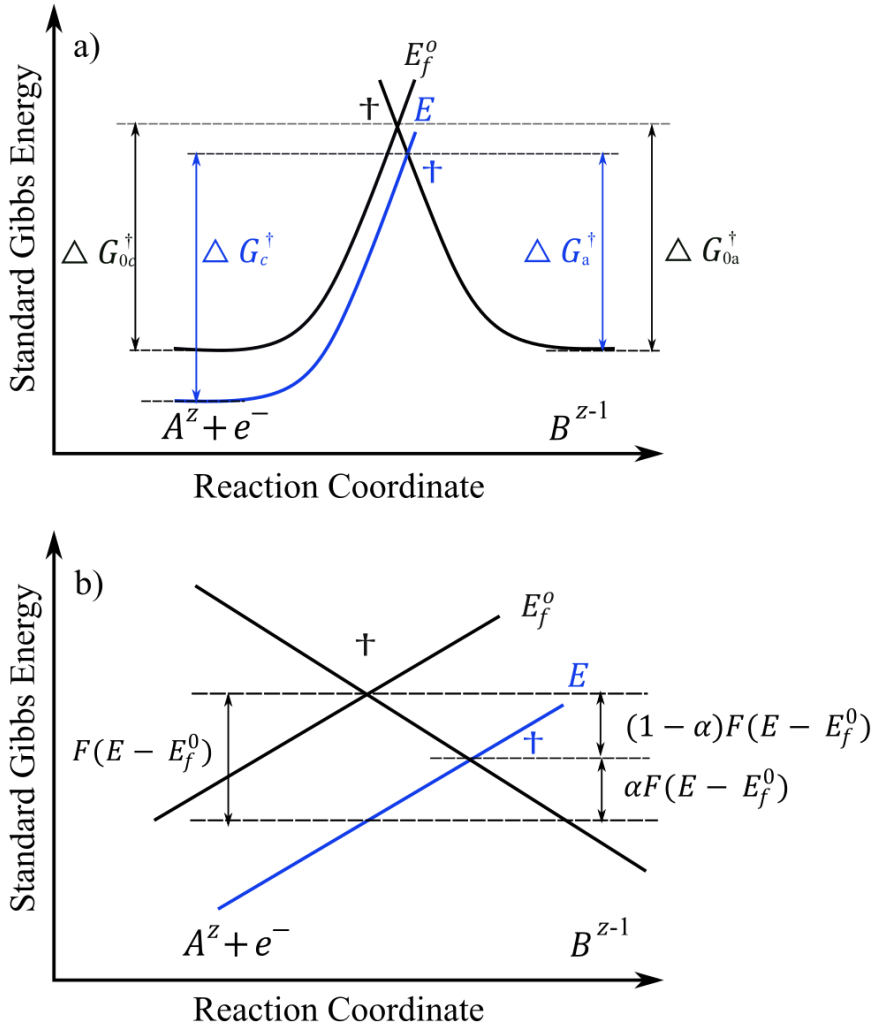


Figure 1.3 The overall Gibbs energy profile for the one-electron reduction of A^z to B^{z-1} when the electrode potential is either E or E_f^0 is illustrated in a) and b) is the magnified plot of the change in a)

In this case, the energy of electrons at the electrode decreased by $F(E - E_f^0)$, thus the energy curve of $A^z + e^-$ shifts downwards. Note however that the overall energy barrier for the oxidation is lowered by only a fraction of $F(E - E_f^0)$. The fraction $(1 - \alpha)$ is defined as the electron transfer coefficient for the oxidation reaction, which is usually written as β.[6] In contrast, α is the electron transfer coefficient for the reduction process. The magnitude of α and β describes the location of the transition state for the reduction and oxidation processes and for a one-electron transfer:

$$\alpha + \beta = 1 \quad \textbf{(1.24)}$$

Consequently, the Gibbs energy for the forward and backward reactions can be expressed as:

$$\triangle G_c^{\dagger} = \triangle G_{0c}^{\dagger} + \alpha F(E - E_f^0) \quad \textbf{(1.25)}$$

$$\triangle G_a^{\dagger} = \triangle G_{0a}^{\dagger} - \beta F(E - E_f^0) \quad \textbf{(1.26)}$$

where $\triangle G_{0c}^{\dagger}$ and $\triangle G_{0a}^{\dagger}$ are the energy barriers for reduction and oxidation before the potential change.

Recall the rate constants in the form of the Arrhenius equation,

$$k_c = A_c \exp\left(-\frac{\triangle G_c^{\dagger}}{RT}\right) = A_c \exp\left(-\frac{\triangle G_{0c}^{\dagger}}{RT}\right) \exp\left(-\frac{\alpha F(E-E_f^0)}{RT}\right) \quad \textbf{(1.27)}$$

$$k_a = A_a \exp\left(-\frac{\triangle G_a^{\dagger}}{RT}\right) = A_a \exp\left(-\frac{\triangle G_{0a}^{\dagger}}{RT}\right) \exp\left(\frac{\beta F(E-E_f^0)}{RT}\right) \quad \textbf{(1.28)}$$

Consider the specific equilibrium condition where the surface concentrations of A^z and B^{z-1} are identical, for which by definition $E = E_f^0$. Consequently, the net flux of reaction becomes zero, $k_c c_{A^z,0} = k_a c_{B^{z-1},0}$, and k_c=k_a, thus,

$$k_c = A_c \exp\left(-\frac{\triangle G_{0c}^{\dagger}}{RT}\right) = k_a = A_a \exp\left(-\frac{\triangle G_{0a}^{\dagger}}{RT}\right) = k_0 \quad \textbf{(1.29)}$$

where k_0 is the standard electrochemical rate constant.

A general form for the rate constants k_c and k_a becomes:

$$k_c = k_0 \exp\left(-\frac{\alpha F(E-E_f^0)}{RT}\right) \quad \textbf{(1.30)}$$

$$k_a = k_0 \exp\left(\frac{\beta F(E-E_f^0)}{RT}\right) \quad \textbf{(1.31)}$$

Recalling **Equations 1.19** and **1.21**, the expression for the net current that flows through the electrode, the full current-potential correlation in **Equation 1.32** is the well-known Butler-Volmer formulation[7, 8].

$$I = FA_{electrode}\left[k_0 \exp\left(-\frac{\alpha F(E-E_f^0)}{RT}\right)c_{A^z,0} - k_0 \exp\left(\frac{\beta F(E-E_f^0)}{RT}\right)c_{B^{z-1},0}\right] \quad \textbf{(1.32)}$$

The Butler-Volmer kinetics model can also be expressed based on electrochemical potential [9, 10], in which way the study of systems with significant double layer effect (such as the dilute electrolyte solution in **Chapter 4**) can be addressed.

Equation 1.32 is built on macroscopic concepts where some microscopic information such as the reactant and product structures and the adsorbed layer on the electrode surface are neglected. Despite the limitations, the Butler-Volmer equation helps gather messages from experimental data for reaction mechanism insights. The use of such a method often requires the known value of charge transfer coefficients, which can be determined by Tafel analysis, as is next described.

For the reaction expressed in **Equation 1.32**, the reaction rate depends on the potential difference between the applied E and the formal potential E_f^0 . By applying extreme values of potential E, the reduction or oxidation term may be negligible.

$$I_c = FA_{electrode}k_0 \exp\left(-\frac{\alpha F(E-E_f^0)}{RT}\right)c_{A^z,0} \qquad \text{if } E \ll E_f^0 \quad \textbf{(1.33)}$$

$$I_a = FA_{electrode}k_0 \exp\left(\frac{\beta F(E-E_f^0)}{RT}\right)c_{B^{z-1},0} \qquad \text{if } E \gg E_f^0 \quad \textbf{(1.34)}$$

where c and a in the subscript refer to the cathodic (reduction) and anodic (oxidation) reactions respectively.

Assuming that the surface concentrations of all species are not significantly different from that in bulk solutions, applying the natural logarithm to **Equation 1.33** and **1.34**,

$$\ln|I_c| = -\frac{\alpha FE}{RT} + constant \quad \textbf{(1.35)}$$

$$\ln|I_a| = \frac{\beta FE}{RT} + constant \quad \textbf{(1.36)}$$

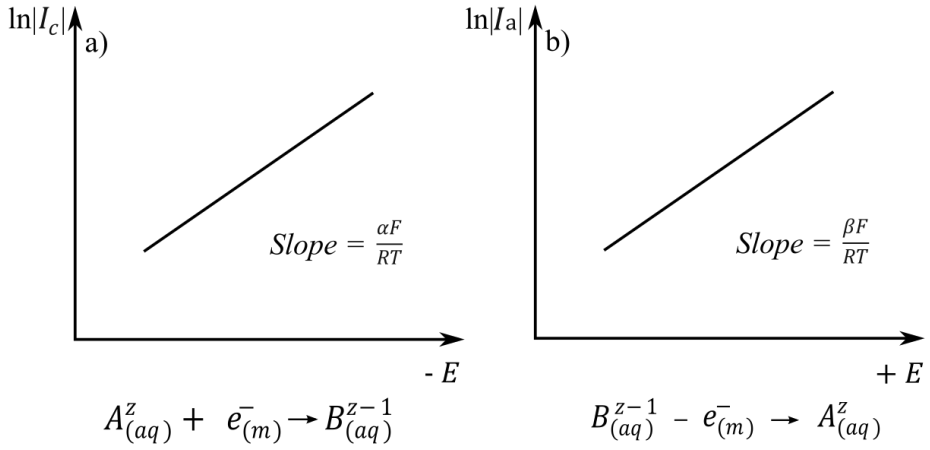


Figure 1.4 Tafel Plots for a single electron transfer reaction a) the reduction process and b) the oxidation process

The transfer coefficient can be obtained from the gradient of the $\ln|I|$ -E plots over a certain range of E (**Figure 1.4**). In particular, the potential range must be carefully selected[11] such that assumption of constant $c_{A^z,0}$ and $c_{B^{z-1},0}$ value made when deriving the equations can be satisfied. Tafel analysis can provide some information of the reaction kinetics, in reality, however, the gradient of $\ln|I| - E$ plot may also suffer the influence from mass transport limitations, especially when the driving force $(\phi_m - \phi_s)$ is lowered within the electrons tunnelling distance due to lack of supporting electrolyte. The importance of mass transport in an electrochemical reaction system is discussed in the next section.

1.3 Mass Transport

Section 1.2 discussed electron transfer at the electrochemical interface, which requires that sufficient reactants are transported from the bulk solution to the electrode surface. The overall observed reaction rate depends on both electrode kinetics and mass transport efficiency. Thus, under fast kinetics, the mass transport of species between the bulk solution and the interface may be the rate-determining step and the measurement cannot indicate the actual rate of the electrochemical reaction. In this section, three generic modes of mass transfer (diffusion, convection and migration)[12] are introduced and their interplay with electrochemical reactions is discussed.

1.3.1 Diffusion

Diffusion is a phenomenon where a species moves from a high concentration to a low concentration environment to maximise the overall entropy. For an electrochemical system, when a potential is applied to the electrode, reactants near the interface are consumed, forming a concentration gradient in the solution phase. The distance that covers the concentration gradient and hence the scale of reactant depletion and product accumulation is referred to as the diffusion layer, as indicated in **Figure 1.5**.

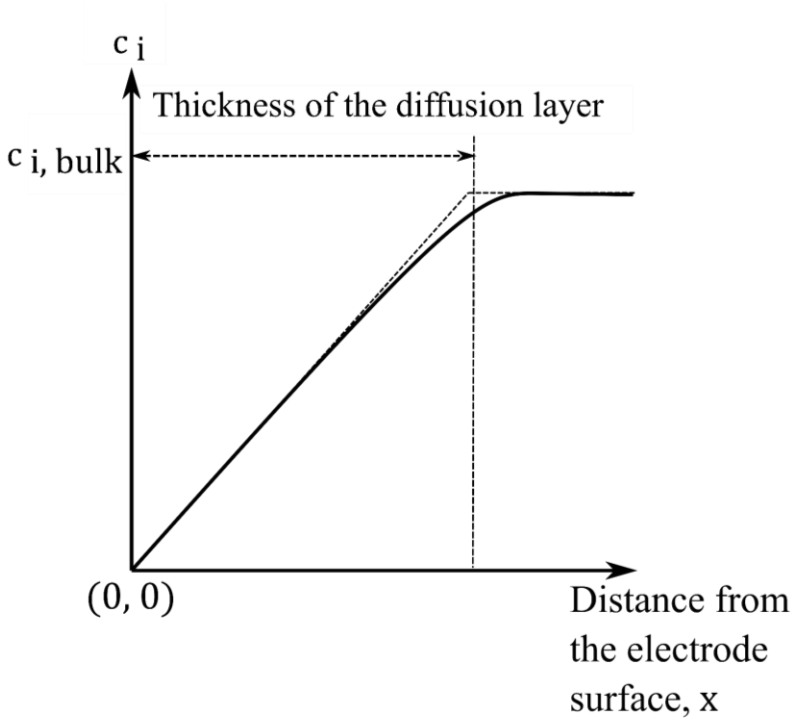


Figure 1.5 An illustrative plot of the Nernst diffusion layer.

The diffusive flux of species i at an arbitrary point x can be quantified by *Fick's first law*:

$$J_i = -D\frac{\partial c_i}{\partial x} \quad \textbf{(1.37)}$$

where J_i describes the number of moles of species i passing through a unit area in unit time in mol m^{-2} s^{-1}, D is the diffusion coefficient in m^2 s^{-1}, $\frac{\partial c_i}{\partial x}$ is the local concentration gradient of i at point x. The direction of the flux down a concentration gradient is indicated by the negative sign.

To describe the rate of concentration change at a certain position, *Fick's second law* can be expressed in one dimension x as:

$$\frac{\partial c_i}{\partial t} = D\frac{d^2 c_i}{dx^2} \quad \textbf{(1.38)}$$

and for a hemispherical electrode, **Equation 1.39** changes into:

$$\frac{\partial c_i}{\partial t} = D\left(\frac{\partial^2 c_i}{\partial r^2} + \frac{2}{r}\frac{\partial c_i}{r\partial r}\right) \quad \textbf{(1.39)}$$

where r is the radial coordinate of the electrode. The 2nd Law is readily derived from the 1st Law via mass conservation.

The physical concept of Fick's law can be explained on a molecular basis. As shown in **Figure 1.6**, consider an arbitrary area A perpendicular to the linear diffusion direction, where the particles of species i move randomly to the right or the left for a distance of δx. The zone adjacent to area A is separated into two even 'slabs' with different concentrations of particles, $c_{i,1}$ and $c_{i,2}$. Thus the amount of particles transferred to the right is $\frac{A\delta x c_{i,1}}{2}$ and $\frac{A\delta x c_{i,2}}{2}$ to the left. In a defined time δt, the net rate of particles transported across the plane A is:

$$rate = \frac{A\delta x(c_{i,1} - c_{i,2})}{2\delta t} \quad \textbf{(1.40)}$$

Thus, the overall flux of species i is:

$$J_i = \frac{\delta x(c_{i,1} - c_{i,2})}{2\delta t} \quad \textbf{(1.41)}$$

As the concentration gradient $\frac{(c_{i,1} - c_{i,2})}{\delta x}$ can be approximated as $-\frac{\delta c_i}{\delta x}$,

$$J_i = -\frac{\delta x^2}{2\delta t}\frac{\delta c_i}{\delta x} \quad \textbf{(1.42)}$$

which is equivalent to Fick's first law when $D = \frac{\delta x^2}{2\delta t}$, mathematically indicating that the diffusion coefficient is a measure of the distance that a molecule can travel within a certain time, and consequently, the diffusion layer thickness is given by **Equation 1.43**.

$$\sqrt{< x^2 >} = 2Dt \quad \textbf{(1.43)}$$

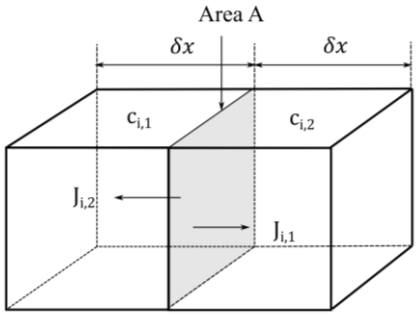


Figure 1.6, Understanding Fick's 1st law on the basis of the random motion of molecules

1.3.2 Convection

The second form of mass transport is convection, including natural and forced types. Natural convection is usually driven by a density gradient such that the flux from a dense region is transported to a dilute region. The density gradient may result from electrolysis or local thermal changes. The effect of natural convection is uncontrollable, irreproducible and usually undesirable; thus, the voltammetry measurements are limited to less than 10-20 seconds to avoid it impacting on nominal diffusion only experiments.

In contrast, forced convection is a controlled movement in the solution phase usually achieved with mechanical methods such as stirring and agitation. The additional mass transport process compresses the diffusion layer where reactants are depleted adjacent to the electrode surface, thus the study can better focus on changes in electrode kinetics and mechanisms.

1.3.3 Migration and Electrical Double Layer

Thirdly, migration refers to the movement of charged species driven by an electrical field (potential gradient). For any species i, the migratory flux can be determined as:

$$J_{m,i} = \frac{z_i F c_i D_i}{RT} \frac{\partial \phi}{\partial x} \quad \textbf{(1.44)}$$

where $J_{m,i}$ is the migratory flux in mol m^{-2} s^{-1}, Z_i is the charge of the species i, D_i is the diffusion coefficient of i in m^2 s^{-1}, c_i is the concentration of i in mol m^{-3} and $\frac{\partial \phi}{\partial x}$ is the potential gradient in V m^{-1}.

In the bulk solution where the concentration gradient of species i is tiny, the species are mainly transported by migration, thus the total flux can be described by **Equation 1.44**. However, when adjacent to the electrode surface, the flux J_i is a combination of the flux with the migration $J_{m,i}$ and the diffusion $J_{D,i}$. Depending on the charge of the species and the electric field, the direction of migratory flux and diffusive flux can be the same or opposite. **Figure 1.7** illustrates three conditions where the particle i is positively charged, negatively charged and uncharged. It is straightforward to understand that the migratory and diffusional fluxes are in the same direction for a cation being reduced at a cathode or an anion oxidized at an anode, while they are in opposite directions when a cation is oxidized at anodes or an anion is reduced at the cathode. Thus the presence of migration may significantly control the current and bring unwelcome complexity to the analysis of the electrochemical signals.

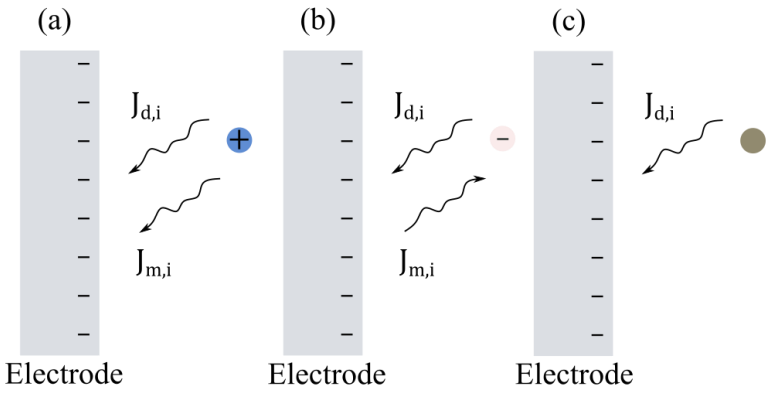


Figure 1.7 Reduction processes with the migratory flux of (a) positively charged species, (b) negatively charged species, (c) uncharged species

Consequently, migration is usually minimized in experiments through the addition of supporting electrolyte consisting of non-electroactive ions at a concentration, usually, 100 times that of the analyte, this is known as the 'full support' condition.[13] Electroanalytical measurements are generally made under conditions of full support to simplify the interpretation of the data and to allow voltammetry to take place at lower overpotential than in the limit of near zero electrolyte ('weak support'). The presence of supporting electrolyte brings three benefits, First, the supporting electrolyte increases the solution phase conductivity and reduces the electrical resistance between the electrode under study and the reference electrode allowing a precise potential to be applied to the former. Second, the electrolyte creates a constant ionic composition in the solution phase and provides uniform ionic strength even under electrolysis, such that the formal potential of the redox couple can be a constant value in the analysed system.

The third and most importantly, supporting electrolyte compresses the potential drop at the interface thus the migratory component with $\frac{\partial \phi}{\partial x}$ vanishes and analytes are transported to the electrochemical interface only by diffusion. At the same time, it compresses the electrical double layer such that most of the potential drop is within an electron tunnelling distance so that the potential applied to the electrode of interest fully serves as the driving force of the electrochemical reaction. **Figure 1.8** illustrates the electrical double layer with anions specifically adsorbed at a positively charged surface in the solution. The potential drop across the double layer can be affected by the scale of the double layer formed, which is measured by the *Debye length*:

$$x_{DL} = \frac{1}{F}\sqrt{\frac{\varepsilon_s \varepsilon_0 RT}{2c_i}} \qquad \textbf{(1.45)}$$

where x_{DL} here is the Debye length for monovalent ion i, ε_s is the relative permittivity of the solution, ε_0 is the permittivity of the free space, R is the gas constant (8.315 J K^{-1} mol^{-1}), T is the absolute temperature in K, F is the Faraday constant (96485 C mol^{-1}). At 298K, values of Debye length for 1×10^{-3} M NaCl and 0.1M NaCl aqueous solutions are 9.6nm and 0.96nm respectively.[14]

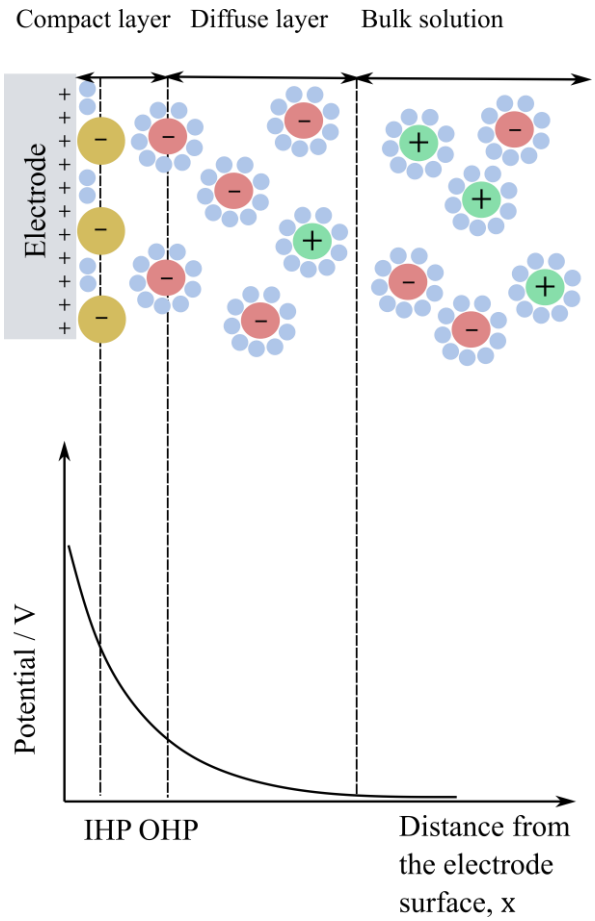


Figure 1.8: Proposed models of the double-layer region with anions specifically adsorbed.

As shown in **Figure 1.8**, when the electrode surface is positively charged relative to that in the solution, anions and dipolar solvent molecules will migrate from solution to adsorb onto the electrode surface driven by the electrostatic forces, forming a closest layer to the electrode

which is known as the Inner Helmholtz Plane (IHP) in which anions are thought to dehydrate. Adjacent to the IHP, the plane where the nearest solvated anions are located via long-range electrostatic forces is called the Outer Helmholtz Plane (OHP). The region between the OHP and the bulk solution is called the diffuse layer where solvated ions are more loosely attracted to the electrode. These layers together form the electrical double layer which creates a zone of overall electrical neutrality at the electrode/solution interface. The potential variation across these layers shows that most of the potential drop from metal to solution-phase occurs within the Helmholtz layer which has a compatible size to the electron tunnelling distance and thus this potential drop is the driving force for electrochemical reaction to occur.

Last but not the least, the specifically adsorbed ions in the double layer, such as halide ions on a silver electrode surface, though they may not be involved in the reaction equation, can significantly change the electrochemical responses even when it is under 'full support'. One such example will be fully discussed in **Chapter 5**.

1.3.4 Weakly Supported Systems

Section 1.3.3 introduced the importance of supporting electrolytes in experimental measurements. There are, however, some cases where the addition of an excess amount of supporting electrolyte are not favourable. For example, the extra electrolyte may influence some redox couples by increasing the ionic strength or by masking processes of interest.[15] Solutions with supporting electrolyte concentrations less than required for diffusion only transport (usually less than 0.1M) are termed 'weakly supported', some natural examples are rainwater and drinking water. Analysis in weakly supported solutions can make detection of analytes reagent free and can facilitate the electroanalysis as described in **Chapter 6**.

One of the major concerns in low support systems is the significant migration of charged ions[16-19]. The potential profile under full support and low support conditions are illustrated in **Figure 1.9**. In the presence of enough supporting electrolyte, the driving force for the electron occurs over a short distance so that electrons can tunnel experiencing the full driving force and the region beyond the compact layer can be assumed as 'zero-field'. If the supporting electrolyte is less than sufficient, the potential drop is over a much longer distance and the driving force $\Delta\phi$ for electron transfer is less. More importantly, due to the lack of ions to 'neutralise' the charged electrode surface, the charged analyte may suffer from migration and the mathematical expression of such a flux has to be revised from **Equations 1.37** and **1.44**. Assuming the activity coefficient is constant, the flux J_i of species i under both migration and diffusion can be modelled with the *Nernst-Planck* equation:

$$J_i = D_i\left(\frac{z_i F c_i}{RT}\frac{\partial \phi}{\partial x} + \frac{\partial c_i}{\partial x}\right) \quad \textbf{(1.46)}$$

where z_i is the charge of species i, F is the Faraday constant (96485 C mol^{-1}), c_i is the concentration of i, R is the gas constant (8.315 J K^{-1} mol^{-1}), T is the absolute temperature in K, $\frac{\partial \phi}{\partial x}$ stands for the electric field and $\frac{\partial c_i}{\partial x}$ is the concentration gradient. In particular, the diffusion coefficient D_i follows the Einstein relation:

$$D_i = \frac{RTu_i}{|z_i|F} \quad \textbf{(1.47)}$$

where u_i is the chemical potential of i, as introduced in **Section 1.1**.

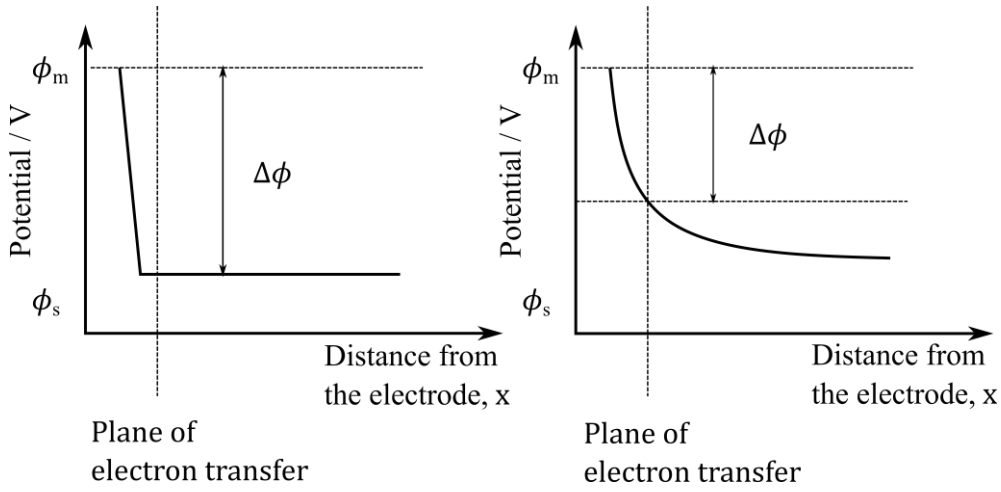


Figure 1.9 The potential drop in the solution phase with full support (left) and low support (right)

1.4 Electrochemical Methods

Important theoretical concepts have been introduced in the above sections. This section consists of practical electrochemical methods from the electrochemical cell to the well-known experimental approach: cyclic voltammetry.

1.4.1 The Electrochemical Cell

A typical electrochemical experiment is performed with an electrochemical cell, the structure of which is shown in Figure 1.11. The cell includes three electrodes: a working electrode (WE), a reference electrode (RE) and a counter electrode (CE), all of them are connected to a '*potentiostat*', which imposes a potential on the working electrode against the reference one.

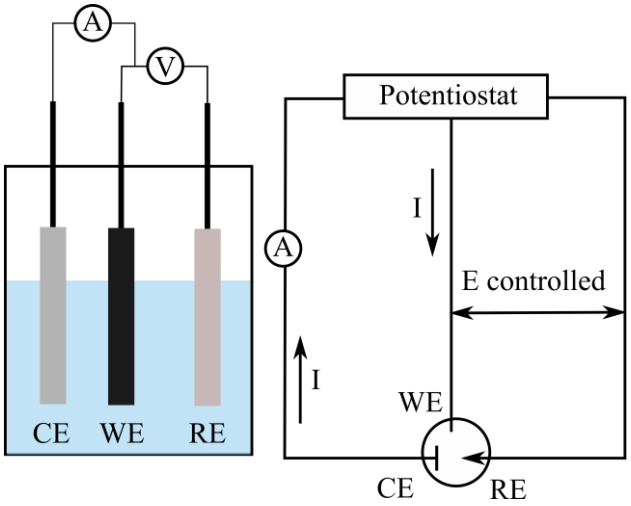


Figure 1.10 Cell and set-up illustrations. (WE: working electrode; RE reference electrode; CE: counter electrode)

The working electrode is the electrochemical interface under analysis, different materials and geometry of the electrode have significant influences on the result signals. Next, the reference electrode, as mentioned in **Section 1.1**, helps to control the potential applied to the working electrode. However, when the current passes by the reference electrode, the chemical composition inside the RE will change and a potential drop builds up between the RE and WE due to the solution resistivity.

To maintain the unchanged potential on the reference electrode, the counter electrode is introduced. Counter electrodes are usually made of materials with excellent electrical conductivity.[20] Once the current is generated in a closed circuit, the potentiostat will control the counter electrode under a certain potential to pass the same amount of current that passed through the working electrode.

Last but not least, electrochemical measurements are possible with only working and reference electrodes when a micro-size working electrode is used. Due to the small radius, only nanoamp

scale current will pass the reference electrode, causing negligible chemical changes and tiny potential drop. Thus, the counter electrode is needless.

1.4.2 Cyclic Voltammetry

One of the most popular electrochemical methods is cyclic voltammetry[21], where the potential on the working electrode is changed linearly under a certain scan rate ν (V s^{-1}) from E_1 to E_2 and reversed. Usually, E_1 is a potential where Faradaic current is negligible, and E_2 is a potential where the electrochemical reaction is diffusionally controlled. The 'linear' ramp is typically controlled digitally and so consists of a vast number of small potential steps each representing an identical amount of potential change. (as shown in **Figure 1.11**). The current is measured at a constant position of each potential step. The results of each measurement are presented as a voltammogram where the current is plotted against the applied potential.

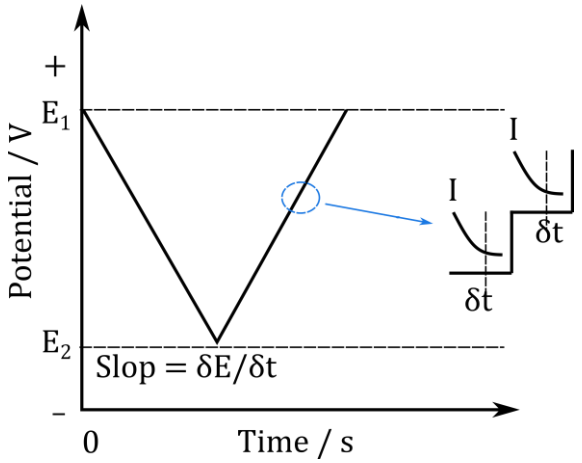


Figure 1.11 The potential-time profile in cyclic voltammetry.

The shape of the voltammogram depends on mass transport, electrode kinetics and the reaction mechanism. Herein four factors will be discussed: the electrode geometry, the electrolyte support level, the electrochemical reversibility and coupled adsorption processes.

First, the geometry of the working electrode is the key factor which affects the diffusion profile adjacent to the electrode surface. Two widely used electrodes are presented in **Figure 1.12** with their diffusion patterns and voltammogram shape illustrated, both of them are demonstrated by the magnitude of the working electrode radius and the diffusion layer thickness.

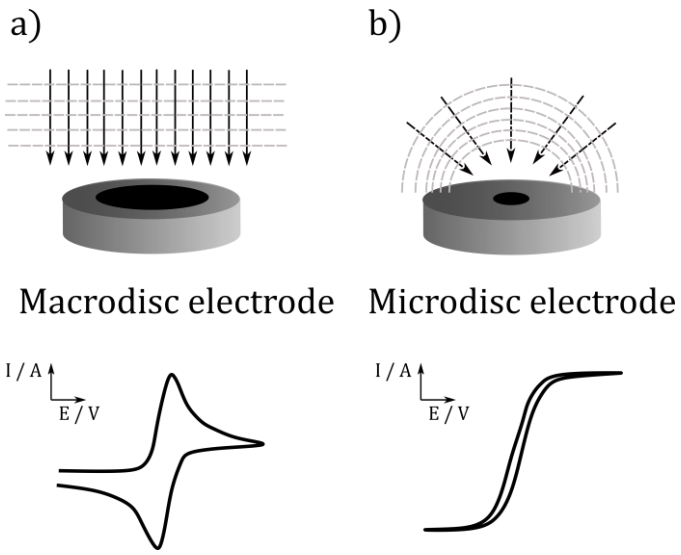


Figure 1.12 Diffusion profile and voltammogram shape on macrodisc (a) and microdisc (b) electrodes.

For a macro electrode with a radius on the scale of cm or mm, the electrode radius is much larger than the thickness of the diffusion layer. Linear diffusion dominates within a typical experimental time scale (**Equation 1.43**). Recall the single electron transfer process in **Equation 1.1**.

$$A^{z}_{(aq)} + e^{-}_{(m)} \rightleftharpoons B^{z-1}_{(aq)} \qquad \textbf{(1.1)}$$

For the reduction process, when the reactant A^z adjacent to the interface is consumed, a fresh feed is required from the bulk solution via diffusion, which results in a thicker diffusion layer and a decay in current, shown as a peak and the same in the reverse scan of a voltammogram.

However, for a micro electrode (with a radius on the μm scale), the diffusion layer is large in comparison with the electrode radius and convergent diffusion dominates with a hemispherical diffusion layer rapidly developed. By this means, species are diffused far more rapidly as compared to that at macro electrodes, thus a steady-state current can be measured.

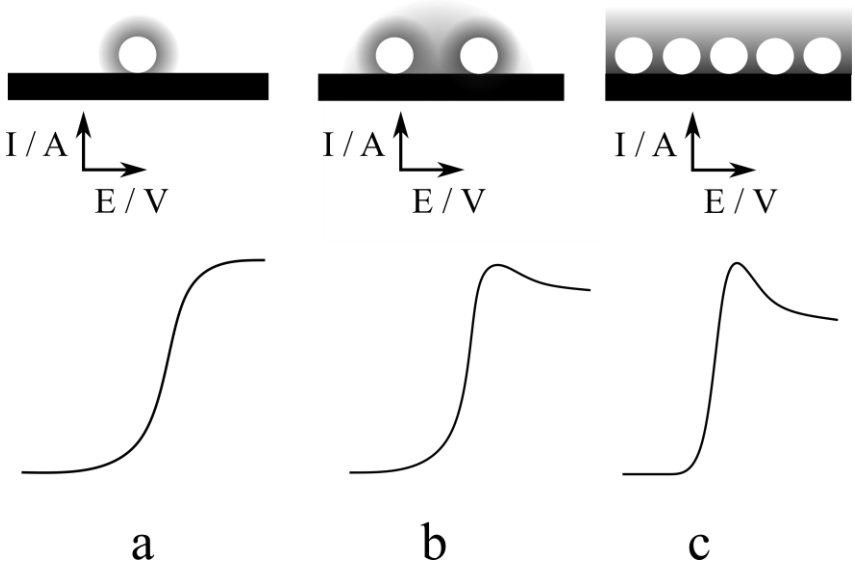


Figure 1.13 Diffusion profile and voltammogram shape (not to scale) on a nanoparticle-modified macrodisc electrode with (a) low particles coverage, (b) medium particles coverage and (c) dense particles coverage in the monolayer. It is assumed that the reaction is fully reversible and the electrode surface is non-active for this reaction

The above discussion summarises differences in diffusion profile from a macro or micro disc electrode surface. With increasing interests in electrode modification especially with nanomaterials[22-31], it is also important to consider the diffusion profile of modified electrodes with various nanoparticle surface coverage. **Figure 1.13** shows how the voltammetric responses change with increasing nanoparticle density on a non-active electrode. In case **a**, the nanoparticle monolayer is sparse thus individual particles serve as independent spherical electrodes and the analyte undergoes convergent diffusion. Consequently, the current reaches steady-state limits, similar to that at a micro electrode. As the number of particles in the monolayer increases, adjacent diffusion profiles merge until a planar diffusion profile is

achieved with a close-packed monolayer (case **c**).[32-34] The surface coverage of such a layer can be described by

$$\sigma = \frac{N \pi r^2}{A_{electrode}} \quad (\mathbf{1.48})$$

where σ is the coverage of an electrode by spherical particles, N is the number of particles with a radius of r and $A_{electrode}$ is the electrode area.

Secondly, a lack of supporting electrolytes can also affect the voltammogram as a consequence of the 'ohmic drop' in the liquid phase. A lower concentration ratio between the supporting electrolyte and the analyte (SR) usually results in a prolonged period to build the driving force at the interface, thus the voltammetric peak can be significantly broadened.[35] For a macro electrode, the broadening becomes detectable with the SR less than 100. Due to fast convergent diffusion, this limit is extended into lower conductive solutions with micro electrodes, which have been widely used in low support medium studies.

Thirdly, electrochemical reversibility is another controlling parameter for the voltammogram shape. The reversibility of an electrochemical process corresponds to the comparison between electrode kinetics and mass transfer rate. Reversible voltammetry requires very fast kinetics relative to the mass transfer, while irreversible voltammetry requires kinetics far slower than the mass transfer rate. For macro electrodes, a mathematical measurement of reversibility was determined and named after the inventors Matsuda and Ayabe[36] Λ, which can be expressed as:

$$\Lambda = \frac{k_0}{\sqrt{\frac{DFv}{RT}}} \quad (\mathbf{1.49})$$

where Λ is the *Matsuda and Ayabe* parameter, k_0 is the standard electrochemical rate constant, D is the diffusion coefficient, F is the Faraday constant (96485 C mol^{-1}), υ is the scan rate, R is the Gas Constant (8.315 J K^{-1} mol^{-1}) and T is the absolute temperature in K.

For a micro electrode, the boundary conditions are defined with a parameter κ_0 [1]

$$\kappa_0 = \frac{r\,k_0}{D} \qquad (\mathbf{1.50})$$

where r is the electrode radius in m, and the other parameters have been defined previously.

The boundary conditions for both electrode scales are listed in **Table 1.1** where all the parameters have been defined in previous sections.

Table 1.1 Boundary conditions for different electrode scales.

	Macro electrodes	**Micro electrodes**
reversible	$\Lambda \geq 15$ $k_0 \geq 0.3\upsilon^{0.5}\ cm\ s^{-1}$	$\kappa_0 \geq 10$
quasi-reversible	$15 \geq \Lambda \geq 10^{-3}$ $0.3\upsilon^{0.5} \geq k_0 \geq 2\times10^{-5}\upsilon^{0.5}\ cm\ s^{-1}$	$10 \geq \kappa_0 \geq 10^{-2\alpha}$
irreversible	$\Lambda \leq 10^{-3}$ $k_0 \leq 2\times10^{-5}\upsilon^{0.5}\ cm\ s^{-1}$	$\kappa_0 \leq 10^{-2\alpha}$

Typical voltammograms for different levels of reversibility of the electrochemical process on a macrodisc electrode and a microdisc electrode are summarized in **Figure 1.14**. The reduction of A is performed in the voltammetry, from a potential E_1 ($E_1 > E_f^0$) where the reaction scarcely happens to E_2 ($E_2 < E_f^0$) where the reaction is nearly complete, then returned to E_1.

For a macro-electrode, the voltammograms with increasing irreversibility are shown in curves from red to yellow, where the peak-to-peak separation increases and peak currents decrease. For a microelectrode, the voltammogram is broadened with increasing irreversibility and the

half-wave potential $E_{1/2}$ where the current equal to half of the steady-state current shifts to a less positive value.

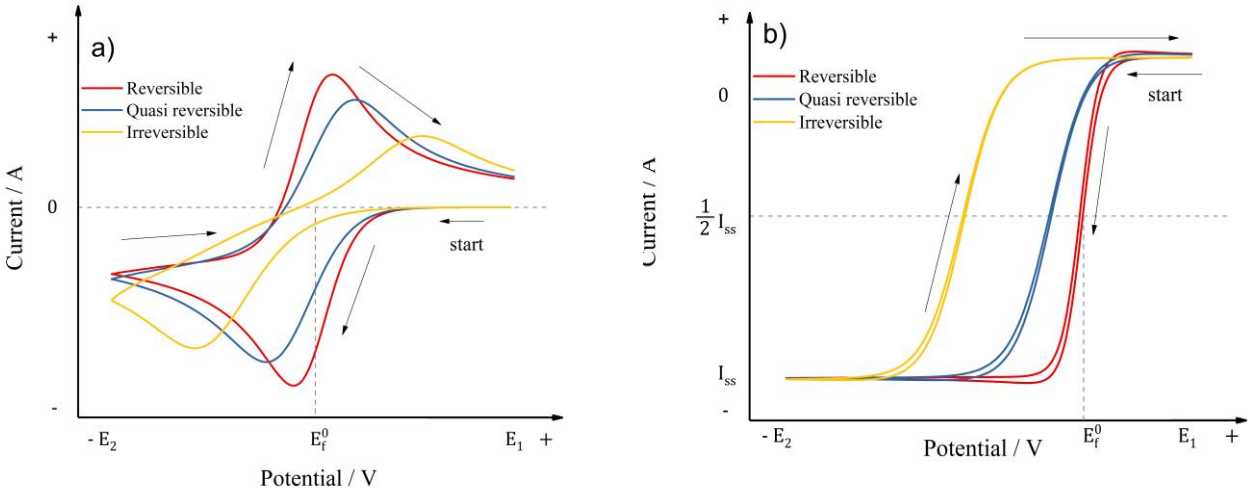


Figure 1.14 Voltammogram with increasing reversibility on (a) macrodisc (b) and microdisc electrodes.

The peak current of a one electron process in the voltammogram at a macro electrode can be described via the *Randles-Ševčík* equations (at 298 K)

$$\text{Reversible } I_p = -0.446FA_{electrode}c_{i,bulk}\sqrt{\frac{F\nu D_i}{RT}} \quad \textbf{(1.51)}$$

$$\text{Irreversible } I_p = -0.496\sqrt{\alpha}FA_{electrode}c_{i,bulk}\sqrt{\frac{F\nu D_i}{RT}} \quad \textbf{(1.52)}$$

where I_p is the peak current, α is the transfer coefficient, F is the Faraday constant, $A_{electrode}$ is the electrode surface area in m^2, $c_{i,bulk}$ is the concentration of species in bulk solution in mol m^{-3} and i stands for A or B. ν is the scan rate in V s^{-1}, D is the diffusion coefficient for species i in m^2 s^{-1}, R is the gas constant and T is the absolute temperature in K.

The voltammogram (at 298 K) with a micro electrode is characterised by:

$$\text{Reversible: } E_{1/2} = E_f^0 + \frac{RT}{2F}\ln\left(\frac{D_B}{D_A}\right) \quad \textbf{(1.53)}$$

Irreversible: $E_{1/2} = E_f^0 + \frac{RT}{\alpha F}\ln\left(\frac{r\,k_0}{D_A}\right)$ (**1.54**)

Under both cases, $I_{ss} = 4nFDc_{i,bulk}r$ (**1.55**)

where $E_{1/2}$ is the half-wave potential in V, E_f^0 is the formal potential in V, r is the radius of the electrode and k_0 is the standard electrochemical rate constant.

Fourth, when the reaction is coupled with specific adsorption of reactant and product on the electrode surface, the voltammetry differs from that of the diffusive species.[37] The voltammetric response of a surface-bound species in processes with different reversibility is displayed in **Figure 1.15**. During a fully reversible process, the voltammetric wave is symmetric. Both reduction and oxidation peak potentials occur at the formal potential E_f^0 of the redox couple and after each peak the current decays to zero due to a finite amount of adsorbed reactive species. With the species already adsorbed, the wave shape in the I-E chart only depends on the rate of electron transfer. With slow kinetics, the signal (red curve) is distorted and two asymmetric waves shift to either side of the formal potential with decreasing peak current. The peak current I_p under reversible and irreversible processes of the surface-bound species can be described as:

$$I_p = \frac{F^2}{4RT}\nu A_{electrode}\Gamma_A^0 \quad (\textbf{1.56})$$

$$I_p = \frac{\alpha F^2}{2.718RT}\nu A_{electrode}\Gamma_A^0 \quad (\textbf{1.57})$$

where Γ_A^0 is the surface coverage of reactant at the electrode surface. Other terms have been defined in previous sections.

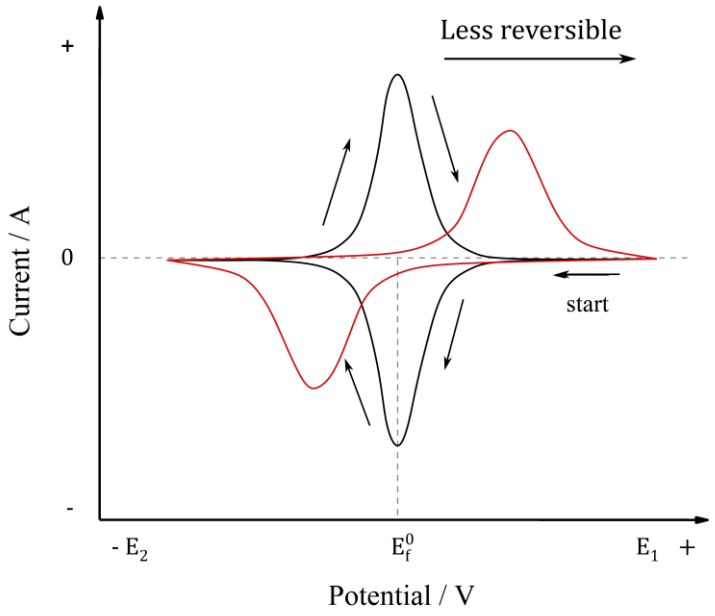


Figure 1.15 The voltammogram of a surface-bound electrochemical reaction with increasing irreversibility.

Hitherto some fundamental aspects of the electrochemistry used in the following chapters have been introduced. The importance of analysis in natural water especially with electrochemistry methods will be discussed in the next chapter.

Bibliography

1. A. J. Bard and L. R. Faulkner, *Electrochemical methods: fundamentals and applications*, Wiley, New York, 2 edn., 2001.
2. R. G. Compton and C. E. Banks, *Understanding voltammetry*, World Scientific, New Jersey, 3rd edn., 2018.
3. R. G. Compton and G. H. W. Sanders, *Electrode potentials*, Oxford University Press, Oxford; New York, 1996.
4. H. Kahlert, in *Electroanalytical Methods*, Springer, Berlin, Heidelberg, 2010, pp. 291-308.
5. A. J. Bard, R. Parsons, J. Jordan, P. International Union of and C. Applied, *Standard potentials in aqueous solution*, M. Dekker, New York, 1985.
6. K. J. Vetter, *Z. Naturforsch. A*, 1952, **7**, 328-333.
7. T. Erdey-Grúz and M. Volmer, *Z. Phys. Chem.*, 1930, **150A**, 203-213.
8. J. A. V. Butler, *Transactions of the Faraday Society*, 1924, **19**, 729-733.
9. K. J. Vetter, *Electrochemical kinetics; theoretical and experimental aspects*, Academic Press, New York, 1967.

10. T. Erdey-Grúz, *Kinetics of electrode processes*, Wiley-Interscience, New York, 1972.
11. D. Li, C. Lin, C. Batchelor-McAuley, L. Chen and R. G. Compton, *J. Electroanal. Chem.*, 2018, **826**, 117-124.
12. A. Survila, in *Electrochemistry of Metal Complexes*, 2015, pp. 33-59.
13. E. J. F. Dickinson, J. G. Limon-Petersen, N. V. Rees and R. G. Compton, *The Journal of Physical Chemistry C*, 2009, **113**, 11157-11171.
14. A. M. Smith, A. A. Lee and S. Perkin, *The Journal of Physical Chemistry Letters*, 2016, **7**, 2157-2163.
15. Y. Wang, E. O. Barnes, E. Laborda, A. Molina and R. G. Compton, *J. Electroanal. Chem.* , 2012, **673**, 13-23.
16. C. Amatore, M. R. Deakin and R. M. Wightman, *J. Electroanal. Chem. Interf. Electrochem.*, 1987, **225**, 49-63.
17. Y. Zhang, B. Zhang and H. S. White, *J. Phys. Chem. B*, 2006, **110**, 1768-1774.
18. E. J. F. Dickinson, J. G. Limon-Petersen and R. G. Compton, *J. Solid State Electrochem.*, 2011, **15**, 1335-1345.
19. C. Batchelor-McAuley, E. Kätelhön, E. O. Barnes, R. G. Compton, E. Laborda and A. Molina, *ChemistryOpen*, 2015, **4**, 224-260.
20. P. Westbroek, in *Analytical Electrochemistry in Textiles*, eds. P. Westbroek, G. Priniotakis and P. Kiekens, Woodhead Publishing, 2005, pp. 3-36.
21. N. Elgrishi, K. J. Rountree, B. D. McCarthy, E. S. Rountree, T. T. Eisenhart and J. L. Dempsey, *J. Chem. Educ.*, 2018, **95**, 197-206.
22. Y. Tang and W. Cheng, *Langmuir*, 2013, **29**, 3125-3132.
23. S. R. Belding, F. W. Campbell, E. J. F. Dickinson and R. G. Compton, *Physical Chemistry Chemical Physics*, 2010, **12**, 11208-11221.
24. X. Dai, O. Nekrassova, M. E. Hyde and R. G. Compton, *Analytical Chemistry*, 2004, **76**, 5924-5929.
25. K. Crowley, E. O'Malley, A. Morrin, M. R. Smyth and A. J. Killard, *Analyst*, 2008, **133**, 391-399.
26. J. Luo, S. Jiang, H. Zhang, J. Jiang and X. Liu, *Analytica Chimica Acta*, 2012, **709**, 47-53.
27. M. Tominaga, T. Shimazoe, M. Nagashima and I. Taniguchi, *Electrochemistry Communications*, 2005, **7**, 189-193.
28. N. Ben Messaoud, M. E. Ghica, C. Dridi, M. Ben Ali and C. M. A. Brett, *Sensors and Actuators B: Chemical*, 2017, **253**, 513-522.
29. M. L. Mena, P. Yáñez-Sedeño and J. M. Pingarrón, *Analytical Biochemistry*, 2005, **336**, 20-27.
30. B. J. Sanghavi, S. M. Mobin, P. Mathur, G. K. Lahiri and A. K. Srivastava, *Biosensors and Bioelectronics*, 2013, **39**, 124-132.
31. P. H. Robbs and N. V. Rees, *Physical Chemistry Chemical Physics*, 2016, **18**, 24812-24819.
32. H. S. Toh, C. Batchelor-McAuley, K. Tschulik, M. Uhlemann, A. Crossley and R. G. Compton, *Nanoscale*, 2013, **5**, 4884-4893.
33. I. Streeter, R. Baron and R. G. Compton, *The Journal of Physical Chemistry C*, 2007, **111**, 17008-17014.
34. T. J. Davies, S. Ward-Jones, C. E. Banks, J. del Campo, R. Mas, F. X. Muñoz and R. G. Compton, *Journal of Electroanalytical Chemistry*, 2005, **585**, 51-62.
35. X. Li, C. Batchelor-McAuley, E. Laborda and R. G. Compton, *Chem. Eur. J.*, 2017, **23**, 15222-15226.
36. I. Ruić, A. Barić and M. Branica, *J. Electroanal. Chem. Interf. Electrochem.*, 1971, **29**, 411-416.
37. D. Menshykau, C. Batchelor-McAuley and R. G. Compton, *J. Electroanal. Chem.* , 2011, **651**, 118-130.

Chapter 2

The Strategy of Natural Waters Analysis

The previous sections introduced the basic fundamental concepts underpinning electrochemical analysis. This chapter provides broad information on natural aqueous media of interest together with a brief discussion on the research scope and features of this study.

2.1 Inorganic Compositions of Seawater and Drinking Water

Natural waters consist of a range of aqueous media among which two extreme cases are seawater and drinking water.

Seawaters are very salty solutions that contain high levels of dissolved sodium chloride with pH ranges from 8.0 to 8.25.[1] **Table 2.1** shows concentrations of major inorganic ions in Pacific Ocean surface seawater, as reviewed by Quinby-Hunt *et al.*, assuming seawater density is 1.025 kg L^{-1} at 293 K.[2] Significant figures in column 2 come from measurements in the literature.[3]

Table 2.1 Major compositions in Pacific Ocean at 293 K

Ions	**Concentration kg L^{-1}**	**Molar mass kg mol^{-1}**	**Concentration mol L^{-1}**
Na^+	10.781	22.99	0.46
Mg^{2+}	1.284	24.31	0.05
K^+	0.399	39.10	0.01
Ca^{2+}	0.4176	40.08	0.01
Cl^-	19.353	35.45	0.53
SO_4^{2-}	2.712	96.07	0.03

Due to the complexity in seawater compositions, 'salinity', *S*, was introduced to provide a measure of overall dissolved salts in a unit mass of seawater (g kg^{-1}, ‰, or ppt). The common range of the surface seawater salinity (SSS) in an open ocean is 32‰ to 37‰[4] (**Figure 2.1**).

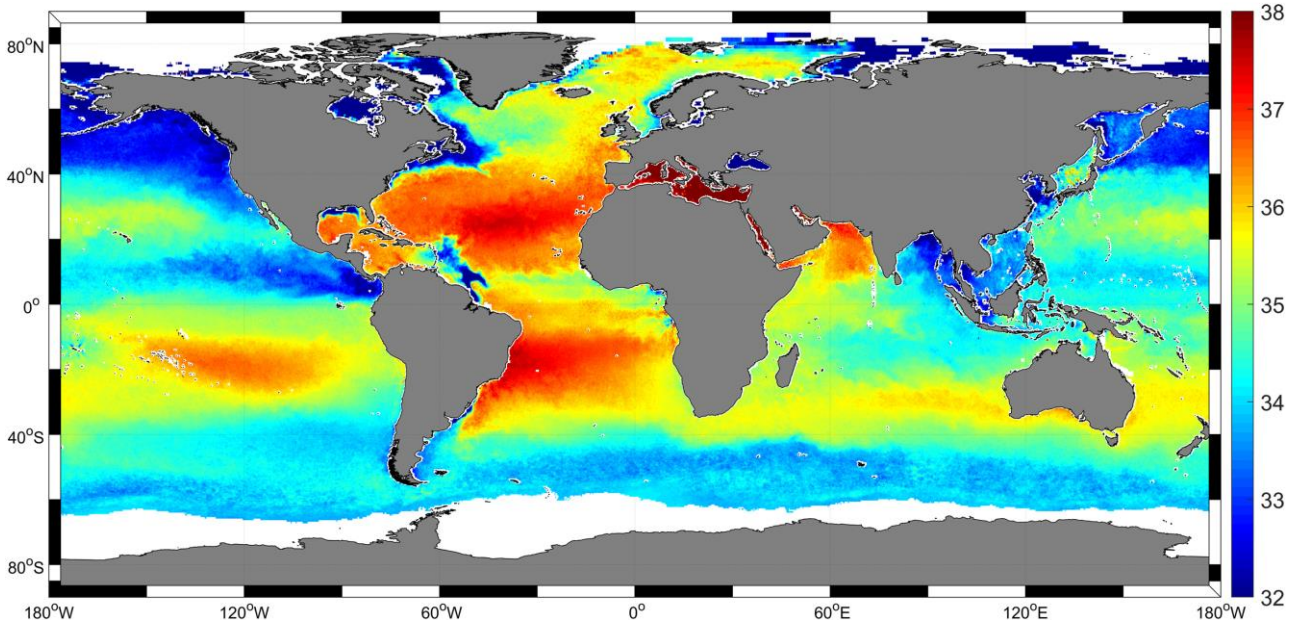


Figure 2.1 Map of the ocean surface salinity average levels in July 2015 generated by the ESA Climate Change Initiative project.[5]

Herein, seawater around the UK and Bermuda is particularly considered, including both surface seawater and deep seawater. Three samples were from three different locations (**Figure 2.2**). Sample 1 is surface seawater from Scotland, supplied by SAMS, sample 2 is Plymouth surface seawater offered by Dr. Samuel Barton. Sample 3 was collected 1 km deep in the ocean around Bermuda and donated by Prof. Heather Bouman. These samples introduce typical levels of trace metals and nutritions to the experiments such that the electrochemical analysis results can be applied to realistic use in seawater.

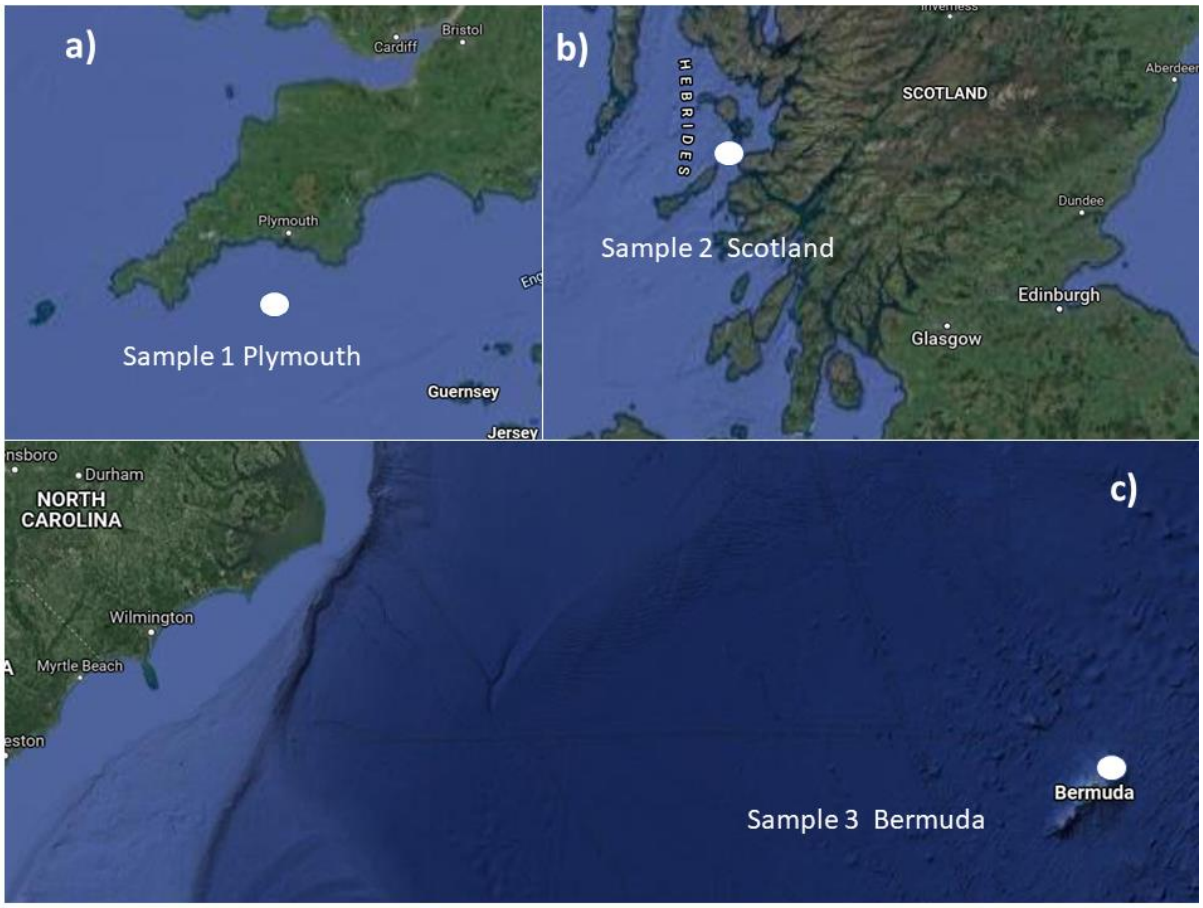


Figure 2.2 Regions for seawater collection.

In contrast to seawater, drinking waters are usually dilute solutions with low mineral contents. Compositions in eight brands of bottled mineral water are listed in **Table 2.2**. Most drinking waters can be classified as neutral low support media with an ionic strength dominated by calcium, sodium, bicarbonate and chloride. However, natural mineral waters such as Borjomi can be quite salty. This study considers both typical bottled water (Tesco and Volvic) and natural mineral water (Borjomi) to validate the research for general applications in a broad range of drinking waters.

Table 2.2 Concentrations of major compositions in drinking waters / mM L^{-1}

	Buxton	**Evian**	**Aqua Pura**	**Tesco Ashbeck**	**Nestle**	**Highland**	**Volvic Sports**	**Nestle Pure Life**	**Borjomi**
Ca^{2+}	1.37	2.00	0.47	0.27	0.67	1.01	0.30	1.47	1.50
Mg^{2+}	0.78	1.07	0.16	0.14	0.43	0.42	0.33	0.41	2.06
Na^{+}	1.04	0.28	0.48	0.43	1.54	0.24	0.52	0.52	67.42
HCO_3^{-}	4.06	0.59	0.82	0.41	3.47	2.46	1.21	3.03	63.91
Cl^{-}	1.04	0.28	0.42	0.39	0.21	0.17	0.42	0.51	10.72
SO_4^{2-}	0.14	0.15	0.15	0.11	0.10	0.06	0.09	0.10	0.52
NO_3^{-}	0.00	0.06	0.32	0.24	0.00	0.05	0.12	0.00	
pH at source	7.4	7.2	6.4	6.2	7.8		7	6.5	6.5

2.2 Research Scope

As discussed above, two typical features of natural waters are the distinct chloride contents and the varied ionic conductivity.

Chloride is one of the major components of seawater and drinking water. The concentration of chloride is a fundamental parameter in water quality and coastal structures. First, chloride concentration usually dominates the rate of metal or concrete corrosion. Second, the level of chloride may accelerate the dissolution of toxic metals such as silver, copper and mercury which can be harmful to aquatic life and human health. Consequently, measurement of chloride levels is essential to both corrosion and toxicology studies.

Apart from chloride levels, the salinity change within various water bodies is a crucial factor when analysing them electrochemically, especially for drinking water which has extremely low total soluble salts content, equivalent to 1-4 mM KNO_3 equivalent via conductivity. As discussed in **Chapter 1**, the facile and low-cost electrochemical methods require sufficient supporting electrolytes to eliminate ohmic drop and migration effects. However, to expand the

application of electrochemistry in water analysis, it is desirable to research the effect of voltammetry under low support conditions and establish a suitable sensor methodology.

General methods of chloride qualifications in natural waters include indirect measurement with salinity approximation or direct determinations via titrations, electrochemistry and chromatography. The indirect method with salinity approximation based on the equation:

$$S = 1.80665\, Cl \qquad (\mathbf{2.1})$$

where S (g kg^{-1}) is solution salinity that can be converted from measured conductivity, Cl (g kg^{-1}) is the chlorinity represents the weight in grams of silver that will react with the halides in 328.5233 g of seawater. Due to the approximation of seawater as standard KCl solution of various chloride concentrations in salinity/conductivity conversions, evaluation of chloride level from salinity may not be reliable.

On the other hand, direct quantifications of chloride in natural waters can reach a lower limit in the scale of μM, though these techniques require trained hands, additional (toxic) reagents and/or expensive instruments.[6, 7]

Recently, electrochemical analysis of chloride has been widely reported utilising silver chloride deposition and stripping signals. Simultaneous detections of chloride, bromide and iodide were performed with silver nanowires with a chloride detection range from 0.2 mM to 20.2 mM by Qin *et al.*[8] Similarly, chloride levels in sweat were detected by silver nanoparticles modified glassy carbon electrode and screen printed electrodes.[9] Still, most of those studies are under 'full support' conditions and samples (sweat or serum) require specific dilution with electrolyte solutions, suggest the need for a robust and facile methdology of chloride analysis directly in natural media capable with low support conditions.

Herein, an electrochemical methodology of natural water analysis in both seawater and drinking water is proposed which specifically considers chloride levels and weakly support conditions. First, this thesis considers the influence of chloride on seawater toxicology (**Chapter 4**), then presents methods for seawater chloride determination (**Chapter 5**) and for the analysis of low support media (**Chapter 6**) whilst the development of a direct chloride sensor in drinking water is reported in **Chapter 7**.

2.3 Key Reactions

Apart from **Chapter 6** which studies the Ag/Ag^+ redox couple under low support conditions, the key voltammetric signals analysed in this thesis are plotted in **Figure 2.2**. The voltammetry was obtained experimentally in air-saturated NaCl solution (0.564M) on a silver macrodisc electrode with a scan rate of 0.02V s^{-1}. The potential started from -0.2 V, swept negatively to perform ORR reactions, and generates superoxide at **Peak 1** and peroxide at **Peak 2**. At -0.75 V, the potential was reversed for silver chloride deposition and stripping. First, the monolayer silver chloride was formed at **Peak 3**. Second, the rapid bulk AgCl formation proceeded and was forced to reverse at **Peak 4** (+0.086V) before significant electrode dissolution. The reversed potential was scanned cathodically through stripping of bulk and surface AgCl at **Peaks 5** and **6** respectively and terminates at -0.2V.

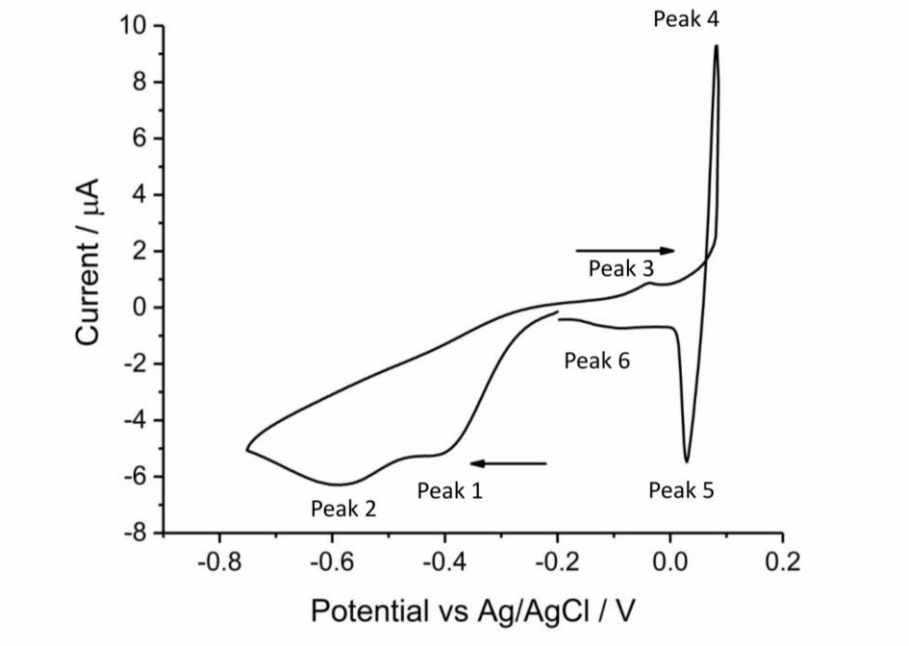


Figure 2.2 AgCl formation and stripping voltammetry after a scan first embracing ORR at 0.1 Vs^{-1} in air-saturated 0.564 M NaCl solution at a silver macro-disc electrode r=1.13 mm at 298 K, scanning from -0.20 V to -0.75 V followed by a reverse scan to +0.086 V then back to -0.20 V.Voltammetric peaks of interests are labelled as peak X (X = 1, 2, 3, 4, 5 or 6).

The relevant reactions are as follows:

Oxygen reduction

Peak 1: $O_2 + e^- \rightleftharpoons O_2^{\cdot -}$; $E^o = -0.284$ V **(2.2)**[10]

Peak 2: $O_2^{\cdot -} + H_2O + e^- \rightleftharpoons HO_2^- + OH^-$; $E^o = -0.0649$ V (pH > 11.6) **(2.3)**[10, 11]

Silver chloride deposition and stripping

Peak 3-6: $AgCl \; + \; + (n\text{-}1)\; Cl^- \rightleftharpoons AgCl_n^{-(n-1)}$ **(2.4)**[12]

where n = 2, 3, 4 [13]

Peaks 1 and **2** are studied in **Chapter 4** where the production of superoxide indicated possible nanotoxicology of silver nanoparticles in seawater. Afterwards, **Peaks 1-6** are fully described

in **Chapter 5** towards the development of a chloride sensor with **Peak 4** in non-diluted seawater with an inbuilt electrochemical activation process (**Peaks 1** and **2**). Afterwards, the method is applied in **Chapter 7** where chloride quantification was studied with **Peak 4** in drinking water, the main difference is that under low chloride concentration, peaks 1 and 2 merge into a single peak for a 2 e^- transfer process forming peroxide species.

Peak 1' $O_2 + 2e^- + 2H^+ \rightleftharpoons H_2O_2,\ E^o = 0.695\ V$ (**2.5**)[10]

or $O_2 + 2e^- + H^+ \rightleftharpoons HO_2^{\cdot-}$, (pH > 11.6) (**2.6**)[10, 11]

Due to the pH and temperature variation in natural water samples, it is essential to clarify how far **Reactions 2.2-2.6** depends on these factors. For pH variations in water samples, both ocean acidification and drinking water ranges are considered. Ocean acidification has been reported widely[1, 14-19], which can lead to continuous pH decrease in global surface seawater from 8.1 to 7.7 in 100 years, as estimated by Jiang *et al*.[1] Consider the pH range for raw water (6.5 ~ 8)[20], the overall pH range for natural seawater and drinking water is 6.5 to 8.25.[1, 20]

Figure 2.4 shows an E-pH diagram regarding oxygen reduction reactions (lines 1-6). As silver chloride deposition and stripping reactions are not pH-dependent, chloride detections across this pH range will remain accurate. For oxygen reduction reactions, however, the overall 4 e^- transfer (line 1) and 2e^- transfer (line 2) processes are pH dependant. Known that the superoxide redox couple is pH-independent (line 4), theoretically, **Peak 1** will be stable unless oxygen concentration and chloride concentration changes (details in **Chapter 4**). When considering **Reactions 2.3, 2.5** and **2.6**, it is important to notice that, without sufficient pH buffer, the depletion of proton near electrode surface will continuously shift the local pH to alkaline conditions, such that **Reaction 2.3** can happen during oxygen reduction in natural seawater with a pH value of 8.2. This means pH changes of samples (the red region in **Figure 2.4**) are

relatively small compared to those during reactions. Even if any significant changes in pH are present, the pH value will not directly change the potential of **Peak 1** in chloride rich media, although the magnitude of **Peak 1** may be affected by the shift of **Peak 2**. Thus the potential of **Peak 1** can be a stable internal reference of the system which will be fully examined in **Chapter 5**. In chloride limited media (drinking water or lake water), the oxygen reduction **Peak 1'** will change according to the pH of the testing sample, thus the peak can only be used for electrode surface activation.

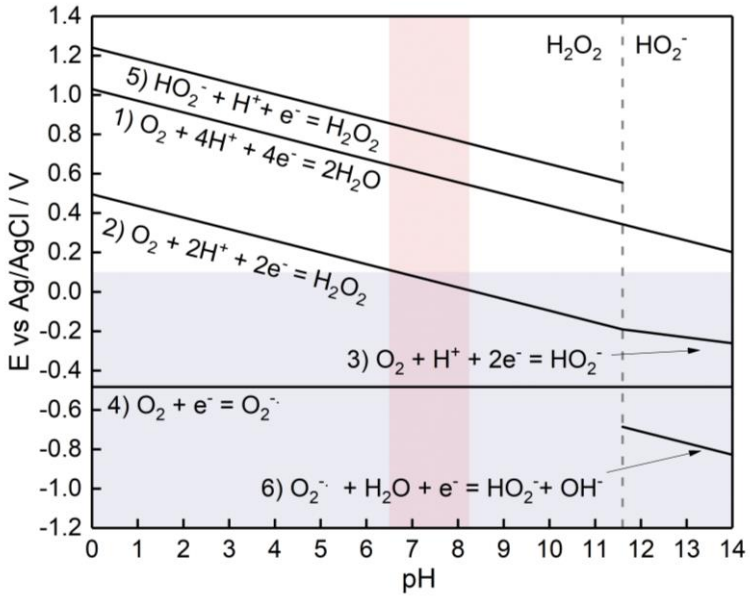


Figure 2.4 E-pH diagram for ORR reactions. The dash-line indicates dissociation of hydrogen peroxide at pKa=11.6. The red region shows the range of pH this method was designed for and the grey region shows the potential range of study (excludes **Chapter 6** where Ag/Ag+ redox couple was studied). Calculations are based on the standard potential of reactions in literature[10], assuming p_{O_2}= 1 atm, $\log\left(\frac{p_{O_2}}{c_{O_2^-}}\right) = 0$, $\log\left(\frac{p_{O_2}}{c_{H_2O_2}}\right) = 0$ and $\log\left(\frac{p_{O_2}}{c_{HO_2^-}}\right) = 0$.

Ocean heating,[21] on the other side, has limited influence on chloride quantifications. In order to ensure unchanged diffusion coefficients and electrochemical kinetics, all samples tested here are under 298 K. Despite limitations in portability, the temperature range of natural water before thermostat control will not affect the final detections. Future work may focus on

regenerating data under various temperatures to satisfy the need for a real potable sensor on site.

The above sections include all the essential background and scope of the research. Generic experimental and simulation methodology will be discussed in the next chapter.

Bibliography

1. L. Jiang, B. R. Carter, R. A. Feely, S. K. Lauvset and A. Olsen, *Scientific Reports*, 2019, **9**, 18624.
2. M. E. Q. Pilson, *An Introduction to the Chemistry of the Sea*, Cambridge University Press, Cambridge, 2 edn., 2012.
3. M. S. Quinby-Hunt and K. K. Turehian, 1983, **64**, 130-130.
4. C. Elachi, and J. v. Zyl, *Introduction to the Physics and Techniques of Remote Sensing*, John Wiley & Sons, Inc., Canada, 2 edn., 2006.
5. N. Reul, S. A. Grodsky, M. Arias, J. Boutin, R. Catany, B. Chapron, F. D'Amico, E. Dinnat, C. Donlon, A. Fore, S. Fournier, S. Guimbard, A. Hasson, N. Kolodziejczyk, G. Lagerloef, T. Lee, D. M. Le Vine, E. Lindstrom, C. Maes, S. Mecklenburg, T. Meissner, E. Olmedo, R. Sabia, J. Tenerelli, C. Thouvenin-Masson, A. Turiel, J. L. Vergely, N. Vinogradova, F. Wentz and S. Yueh, *Remote Sensing of Environment*, 2020, **242**, 111769.
6. P. Quevauviller and K. C. Thompson, 2006.
7. L. S. Clesceri, A. E. Greenberg and A. D. Eaton, *Standard Methods for the Examination of Water and Wastewate*, APHA American Public Health Association, USA, 20th edn., 1998.
8. X. Qin, H. Wang, Z. Miao, X. Wang, Y. Fang, Q. Chen and X. Shao, *Talanta*, 2011, **84**, 673-678.
9. H. S. Toh, C. Batchelor-McAuley, K. Tschulik, M. Uhlemann, A. Crossley and R. G. Compton, *Nanoscale*, 2013, **5**, 4884-4893.
10. A. J. Bard, R. Parsons, J. Jordan, P. International Union of and C. Applied, *Standard potentials in aqueous solution*, M. Dekker, New York, 1985.
11. B. B. Blizanac, P. N. Ross and N. M. Markovic, *Electrochimica Acta*, 2007, **52**, 2264-2271.
12. M. F. L. de Mele, R. C. Salvarezza, V. D. Vasquez Moll, H. A. Videla and A. J. Arvia, *J. Electrochem. Soc.* , 1986, **133**, 746-752.
13. R. D. Giles, *J. Electroanal. Chem. Interf. Electrochem.*, 1970, **27**, 11-19.
14. O. Hoegh-Guldberg, P. J. Mumby, A. J. Hooten, R. S. Steneck, P. Greenfield, E. Gomez, C. D. Harvell, P. F. Sale, A. J. Edwards, K. Caldeira, N. Knowlton, C. M. Eakin, R. Iglesias-Prieto, N. Muthiga, R. H. Bradbury, A. Dubi and M. E. Hatziolos, 2007, **318**, 1737-1742.
15. J. M. Guinotte and V. J. Fabry, *Annals of the New York Academy of Sciences*, 2008, **1134**, 320-342.
16. H. Pörtner, *Marine Ecology Progress Series*, 2008, **373**, 203-217.
17. V. J. Fabry, B. A. Seibel, R. A. Feely and J. C. Orr, *ICES Journal of Marine Science*, 2008, **65**, 414-432.
18. S. C. Doney, V. J. Fabry, R. A. Feely and J. A. Kleypas, 2009, **1**, 169-192.
19. B. Hönisch, A. Ridgwell, D. N. Schmidt, E. Thomas, S. J. Gibbs, A. Sluijs, R. Zeebe, L. Kump, R. C. Martindale, S. E. Greene, W. Kiessling, J. Ries, J. C. Zachos, D. L. Royer, S. Barker, T. M. Marchitto, R. Moyer, C. Pelejero, P. Ziveri, G. L. Foster and B. Williams, 2012, **335**, 1058-1063.

20. J. DeZuane, *Handbook of Drinking Water Quality*, John Wiley & Sons, Inc., Canada, 2 edn., 2007.
21. B. Bronselaer and L. Zanna, *Nature*, 2020, **584**, 227-233.

Chapter 3

Methodology

In this chapter, experimental and simulation details used throughout this thesis will be introduced.

3.1 Chemical Reagents and Instruments

All the chemical reagents used in experiments reported in this thesis are listed in **Table 3.1**. Solutions were prepared using deionised water (Millipore Water Systems, UK) with a measured resistivity of 18.2 MΩ cm at 298 K unless otherwise stated. The concentrations of specific solutions are described in **Chapters 4-7**.

Table 3.1 Chemical reagents

Chemical names	**Formula**	**Purity grade**	**Supplier**
Oxygen	O_2	99.5%	BOC Gases plc
Nitrogen	N_2	99.998%	BOC Gases plc
Silver trifluoromethanesulfonate	Ag (CF_3SO_3)	≥99.95%	Sigma-Aldrich
Silver nitrate	$AgNO_3$	>99%	Sigma-Aldrich
Potassium nitrate	KNO_3	≥99%	Honeywell Fluka
Potassium chromate	K_2CrO_4	≥99.0%	Sigma-Aldrich
Ultrapure water	H_2O	Spectrophotometric grade	Alfa Aesar
Sodium perchlorate	$NaClO_4$	98.0%	Sigma-Aldrich
Hexaammineruthenium(III) chloride	$[Ru(NH_3)_6]Cl_3$	98%	Sigma-Aldrich
Potassium chloride	KCl	99%	Sigma-Aldrich
Sodium chloride	NaCl	≥99.5%	Sigma-Aldrich
Calcium chloride dihydrate	$CaCl_2$ $2H_2O$	>99.0%	Sigma-Aldrich
Magnesium chloride hexahydrate	$MgCl_2$ $6H_2O$	≥99.0%	Sigma-Aldrich
Sodium bicarbonate,	$NaHCO_3$	99.5-100.5%	Sigma-Aldrich
Sodium sulfate	Na_2SO_4	≥99.0%, anhydrous	Sigma-Aldrich

Table 3.1 (continued).

Potassium bromide,	KBr	>99%	Sigma-Aldrich
Sodium fluoride	NaF	>99.0%	Sigma-Aldrich
Boric Acid	H_3BO_3	≥99.5%	Sigma-Aldrich
Strontium chloride hexahydrate	$SrCl_2 \cdot 6H_2O$	99%	Sigma-Aldrich
Tesco Ashbeck water (2000 mL)	N/A	N/A	Tesco
Volvic natural Mineral Water (1500 mL)	N/A	N/A	Volvic
Borjomi sparkling mineral water (500 mL)	N/A	N/A	Borjomi
Quasi-spherical silver nanoparticles (ca.100 nm diameter)	AgNPs	Nanoxact, 0.02 mg mL^{-1} silver, 2 mM sodium citrate	Nanocomposix
Natural seawater samples	1. Collected at inner seas off the West Coast of Scotland		SAMS
	2. Collected off the coast of Plymouth (Western Channel Observatory)		Dr. Samuel Barton, Department of Earth Science, Oxford University.
	3. Collected from Bermuda 2 km deep in the sea		Prof. Heather Bouman, Department of Earth Science, Oxford University.

Electrochemical experiments were performed with a μAutolab Type III potentiostat or an in-lab built potentiostat[1], using a standard three-electrode setup in a grounded Faraday cage. The electrochemical cell was thermostated at 298 (±0.5) K unless otherwise stated through the use of either a conventional water bath or a home-made optimised thermostated system as described in the literature.[2] Electrodes and their geometry are listed in **Table 2.2**. Glassy carbon and gold working electrodes were calibrated electrochemically by analysing the reduction wave (macro electrodes) or the steady-state current (micro electrodes) of 1.0 mM hexaaminеruthenium(III) chloride (ruhex), 0.1 M potassium chloride aqueous solution. The

diffusion coefficient used to evaluate electrode radii was 8.4×10^{-10} $m^2 s^{-1}$ for $[Ru(NH_3)_6]^{3+}$ (at 298 K).[3-6] The silver macro electrode 1 used in **Chapter 3** was calibrated with the same 'ruhex' solution as above. However, due to the adsorption of chloride found on the silver electrode, the silver macro electrode 2 used in **Chapters 4** and **6** were calibrated with the peak height of oxygen reduction reaction in oxygen saturated 0.1 M KNO_3 solutions. The oxygen diffusion coefficient and oxygen solubility used to evaluate the electrode radius was 1.96×10^{-19} $m^2 s^{-1}$ [7] and 1.26 mM[8] at 298 K. Calibration of electrodes with voltammograms may introduce errors from the wide range of oxygen solubility and diffusion coefficient in aqueous solutions (see **Section 2** in **Appendix A**). In **Table 3.2**, the calibrated radii of silver electrodes 1 and 2 are more than 10% higher than their nominal scales which is typical given that the electrodes are sold with a 'nominal' radius'. Electrochemical characterisation of electrode radii is a standard protocol in the field where the dangers of using the nominal values supplied by the manufacturers are widely appreciated. Meanwhile, direct measurements with a travelling microscope were also performed as references for the values of electrochemical cabiration radii.

Table 3.2 Electrode specifications

	Specification	**Manufacture**
Working electrodes		
Glassy carbon macrodisc electrode (GC)	Radius: 1.5 mm (nominal)； 1.49 mm (calibrated); (measured) 1.49 mm	BASi
Polycrystalline silver macrodisc electrode (Ag) 1	Radius: 1 mm (nominal)； 1.36 mm (calibrated); (measured) 0.99 mm	Home-made
Polycrystalline silver macrodisc electrode (Ag) 2	Radius: 1 mm (nominal)； 1.13 mm (calibrated) (measured) 1.00 mm	Home-made
Gold microdisc electrode	Radius: 5 μm (nominal); 5.4 μm (calibrated)	ALS Co. Ltd.

Table 3.2 (continued).

Reference electrodes		
Ag/AgCl	Saturated KCl solution, or 3.4 M KCl solution	Home-made
SCE	Saturated KCl solution	ALS Co. Ltd.
Silver wire	1 mm (radius), 99.99% purity.	Alfa Aesar
$Ag/AgNO_3$	10 mM $AgNO_3$, 90 mM KNO_3	Home-made
Counter electrodes		
Platinum wire	N/A	Alfa Aesar

All working electrodes were polished using a sequence of 1.0, 0.3 and 0.05 μm alumina lapping compounds (Bucher, Germany) before use unless otherwise stated. The calibration of the $Ag/AgNO_3$ reference electrode will be discussed in **Chapter 7**.[9] In particular, a platinum wire was used as a counter electrode instead of a graphite electrode due to the difficulty to completely remove metal or organic contamination that been absorbed in the graphite porous structure. However, when the potential goes very negative (ie.-1.0V vs Ag/AgCl) in **Chapters 5** and **7**, the experiments are at risk of Pt dissolution (E^0= 1.188 V)[10]. Herein the Pt wire was cleaned with a hydrogen bunsen burner followed by a roughening process with 1400 grid sandpaper. The use of sandpaper can maximise the electrode surface area to conduct currents without significant dissolution of platinum and its corresponding redeposition process on the working electrode surface.

Last but not least, the experimental apparatus for the well-established argentometric method[11] consisted of a 50.0 mL glass burette with a stand, a 250 mL glass conical flask and measuring cylinders. Reagents are specified in **Table 3.1** and the concentrations in **Chapter 5**.

3.2 Simulation Programs

Two simulation programs were used in this thesis. First, the commercial software DigiSim® was used to simulate the oxygen reduction reaction in **Chapter 4**. [12, 13] Second, a home-written program was developed by Dr Christopher Batchelor-McAuley for metal deposition and stripping voltammetry with a variable amount of supporting electrolyte as employed in **Chapter 6**.

Bibliography

1. C. Batchelor-McAuley, J. Ellison, K. Tschulik, P. L. Hurst, R. Boldt and R. G. Compton, *Analyst*, 2015, **140**, 5048-5054.
2. D. li, D.phil., University of Oxford, 2020.
3. Y. Wang, J. G. Limon-Petersen and R. G. Compton, *J. Electroanal. Chem.*, 2011, **652**, 13-17.
4. Y. Guo, M. Yang, C. Batchelor-McAuley and R. G. Compton, *J. Electroanal. Chem.*, 2019, **849**, 113370.
5. Y. J. Guo, M. J. Yang, R. C. Xie and R. G. Compton, *Chem. Sci.*, 2021, **12**, 397-406.
6. Y. Guo and R. G. Compton, *Talanta*, 2021, **232**.
7. C. C. M. Neumann, E. Laborda, K. Tschulik, K. R. Ward and R. G. Compton, *Nano Res.*, 2013, **6**, 511-524.
8. K. Shimizu, L. Sepunaru and R. G. Compton, *Chem. Sci*, 2016, **7**, 3364-3369.
9. Y. Guo and R. G. Compton, *Analyst*, 2021, **146**, 4700-4707.
10. A. J. Bard, R. Parsons, J. Jordan, P. International Union of and C. Applied, *Standard potentials in aqueous solution*, M. Dekker, New York, 1985.
11. L. S. Clesceri, A. E. Greenberg and A. D. Eaton, *Standard Methods for the Examination of Water and Wastewate*, APHA American Public Health Association, USA, 20th edn., 1998.
12. A.W. Bott, S.W. Feldberg and M. Rudolph, *Curr. Sep.*, 1996, **15**, 67-71.
13. A. W. Bott, *Curr. Sep.*, 1999, **18**, 9-16.

Chapter 4

The Oxygen Reduction Reaction at Silver Electrodes in High Chloride Media and the Implications for Silver Nanoparticle Toxicity

Electrochemical analysis in natural aqueous media provides environmentally important information and new physiochemical insights to encourage further applications. In this thesis, two distinct media, seawater and drinking water are analysed, covering the full range of voltammetric signals from extremely high ionic strength to near electrolyte free. For both media, a sensor was established allowing facile and fast detection of chloride. To begin with, seawater was analysed first using the oxygen reduction reaction (ORR) on a silver electrode.

The ORR at neutral pH in various aqueous chloride-containing solutions was investigated voltammetrically. In particular, the ORR was performed in high chloride containing aqueous media including authentic and synthetic seawater under oxygen saturated conditions and compared with that in aqueous nitrate and perchlorate media. The experimental voltammograms revealed a two-electron process forming hydrogen peroxide in low chloride media. In contrast, high concentration chloride solutions, including both synthetic and authentic seawater showed an increase of overpotential, accompanied by a splitting of the voltammetric peak into two one-electron features indicating the formation of superoxide in the first step and its release from the silver-solution interface. The implications for silver nanoparticle toxicology were discussed given the markedly greater toxicity of superoxide

over peroxide and the high levels of chloride in biological media as well as in seawater. This work presented in this chapter has been published as a first author paper in *Chemical Science* and was carried out in collaboration with Dr. Minjun Yang and Ruo-chen Xie.[1]

4.1 Introduction

Provoked by increasing concern over environmental changes much attention is currently focussed on sustainable energy investigations. One such focus concerns those fuel cells where the Oxygen Reduction Reaction (ORR) has been extensively studied as the cathodic reaction. In general, the ORR can be either a 4-electron transfer process (**Reaction 4.1**) or a 2 + 2 electron - double step process involving hydrogen peroxide (H_2O_2) formation (**Reaction 4.2-4.3**).[2-6] This production of hydrogen peroxide as an intermediate or product decreases the overall cell efficiency, but precious metals (notably Pt) are required as a catalyst layer to realise the former route, which increases the capital cost of energy devices.[3]

$$O_2 + 4e^- + 4H^+ \rightleftharpoons 2H_2O \quad \textbf{(4.1)}$$

$$O_2 + 2e^- + 2H^+ \rightleftharpoons H_2O_2 \quad \textbf{(4.2)}$$

$$H_2O_2 + 2e^- + 2H^+ \rightleftharpoons 2H_2O \quad \textbf{(4.3)}$$

Accordingly attention has been turned to alternative materials, among which silver is considered a potential catalyst for anion exchange membrane fuel cells.[7] The replacement of Pt catalysts usually requires alkaline conditions to achieve lower overpotentials for the O_2/ $O_2^{\cdot-}$ redox couple.[8-10] In the low pH region, the reaction on silver involves both $2e^-$ and $4e^-$ pathways with less H_2O_2 generated as the overpotential increases. In alkaline solution, however, the overpotential drops significantly and reaction follows a $4e^-$ pathway

predominately.[11-13] The first electron transfer to oxygen regardless of pH is recognized as the rate determining step (RDS).[14, 15]

It is clearly evidenced that H_2O_2 formation is involved in the ORR on Ag in neutral solution, though the mechanism is sensitive to the surface oxidation state and morphology as well as the electrode potential.[16] In particular, the produced peroxide may undergo catalytic decomposition alongside or as an alternative, rapid electroreduction to water (**Reaction 4.4-4.8**).[17]

$$O_2 + e^- \rightleftharpoons O_2^{\cdot-} \text{ (RDS)} \qquad (\mathbf{4.4})$$

$$O_2^{\cdot-} + H_2O + e^- \rightleftharpoons HO_2^- + OH^- \qquad (\mathbf{4.5})$$

$$HO_2^- + H_2O \rightleftharpoons H_2O_2 + OH^- \qquad (\mathbf{4.6})$$

The formation of hydrogen peroxide is followed by catalytic decomposition

$$H_2O_2 \xrightarrow{Ag} H_2O + \frac{1}{2}O_2 \qquad (\mathbf{4.7})$$

or electroreduction:

$$H_2O_2 + 2H^+ + 2e^- \longrightarrow 2H_2O \qquad (\mathbf{4.8})$$

Note that **Reaction 4.5** might occur directly as written or as a CE (homogeneous chemical reaction followed by an electron transfer step) sequence in which superoxide first reacts with water to form $HO_2^{\cdot}$ and OH^- followed by reduction of $HO_2^{\cdot}$.

The European consumption of AgNPs reached 35 tons per year in 2014 with global demand steadily increasing towards an estimated value of 600 tons per year in 2020.[18] The main applications of AgNPs exploit their antiviral, antimicrobial and anti-inflammatory properties[19-24] but the extensive scale of use has driven concerns on its toxicity to the natural

environment given the likely release of large quantities of silver nanoparticles into the environment. At the nanoscale, the ORR on silver is especially interesting in so far that it concerns the nanotoxicology of silver nanoparticles (AgNPs). This in turn has led to mechanistic studies of nanoparticle dissolution and antibacterial behaviour.[25]

AgNPs kill bacteria via damaging membrane structures and intracellular biomolecules by possible mechanisms including AgNPs attachment to the membrane, catalytic formation of reactive oxygen species (ROS) and silver ion dissolution[26-28]. All of those are sensitive to the local chemical environment. The oxidative dissolution of AgNPs in aqueous solution can be favoured by the presence of Cl^-, I^- and phosphate anions[29] although the release of Ag^+ can however simultaneously be inhibited by trace amounts of chloride due to formation of AgCl layers at the nanoparticle surface.[30] The combined anion effects influencing *both* thermodynamics and kinetics hint at the complexity of silver nanotoxicology in natural media where, for example, it is observed that AgNPs are relative stable with less Ag^+ dissolution and ROS formed in environments such as authentic human saliva.[31]

Does size matter? It is generally believed that AgNPs have higher antibacterial activity[32] compared to bulk silver - which is thought not toxic at all. One explanation of the size dependence of the toxicity of silver is in terms of the change of ORR pathways resulting from competition between the particle-size-controlled mass transport and the heterogeneous decomposition rate. Batchelor-McAuley *et al*.[33] proposed a mechanism for the size dependency based on the insight that the dissolution of Ag as Ag^+ cations is coupled with the reduction of oxygen at the surface of the dissolving nanoparticle. As noted above in **(Reaction 4.4 – 4.8)**, the ORR on Ag proceeds via the formation of hydrogen peroxide followed by the further heterogeneous chemical decomposition of this intermediate to form

water. By comparing the rate of the hydrogen peroxide transformation into water with the rate of its diffusion away from the particle it was concluded that a switchover in products occurred when the two rates matched. Note that the size dependence arises since the mass transport coefficient (k_{MT}) for the loss of hydrogen peroxide is given by D/r where D is the diffusion coefficient of H_2O_2 and r is the particle radius. Thus, hydrogen peroxide 'escapes' more easily from smaller particles than from larger ones (**Reaction 4.9 - 4.11**).

$$O_2 + 2e^- + 2H^+ \rightarrow H_2O_2 \quad (\mathbf{4.9})$$

$$H_2O_2 \xrightarrow{k_{HET}} H_2O + \frac{1}{2}O_2 \quad (\mathbf{4.10})$$

$$H_2O_2 \xrightarrow{k_{MT}} \text{Bulk} \quad (\mathbf{4.11})$$

Cyclic voltammetry data for the ORR on silver provided the relevant heterogeneous rate constant ($k_{HET} = 0.013$ cm s^{-1} at 298 K) for the formation of water. This allowed estimation of the particle radius, r, for the switch over from hydrogen peroxide formation to water formation to be in the region of ca. 10 microns consistent with independent observations.[16, 33, 34]

The analysis leading to **Reaction 4.9 – 4.11** proposed by Batchelor-McAuley *et al.* assumes that the products of the ORR on silver are either water or hydrogen peroxide. From a toxicity point of view, it is to note that, H_2O_2 is less reactive compared to other ROS in the absence of light or trace metal ions such as iron and copper (**Reaction 4.12 – 4.13**) [35].

$$Fe^{II} + H_2O_2 \rightarrow Fe^{III} + OH^{\cdot} + OH^- \quad (\mathbf{4.12})$$

$$Cu^{I} + H_2O_2 \rightarrow Cu^{II} + OH^{\cdot} + OH^- \quad (\mathbf{4.13})$$

In contrast the superoxide radical ion, $O_2^{\cdot-}$, although not as reactive as its protonated form, $HO_2^{\cdot}$ (pKa=4.8), is highly toxic at physiological pH; the reaction of $O_2^{\cdot-}$ with H_2O_2 and reactions with nitric oxide radical (**Reaction 4.14 – 4.16**) can lead to formation of a short-lived and highly aggressive ROS, hydroxyl radicals $OH^{\cdot}$.[36-38] The $OH^{\cdot}$ radical, with a reduction potential reported at 2.31V [39], is a strongly oxidizing reagent and can *kill* a diverse range of single-cellular phytoplankton at a near-mass-transport limited rate.[40]

$$\cdot ON + O_2^{-\cdot} \longrightarrow ONOO^- \quad (\mathbf{4.14})$$

$$ONOO^- + H^+ \longrightarrow OH^{\cdot} + NO_2\cdot \quad (\mathbf{4.15})$$

$$H_2O_2 + O_2^{-\cdot} \longrightarrow O_2 + OH^{\cdot} + OH^- \quad (\mathbf{4.16})$$

Moreover, superoxide $O_2^{\cdot-}$ and hydroxyl radicals $OH^{\cdot}$ react with most biomolecules in their path including lipids, proteins, and DNA. In reactions with saturated compounds, hydroxy radicals $OH^{\cdot}$ can abstract hydrogen atoms from carbon–hydrogen bonds forming a stronger OH bond and radical propagation (**Reaction 4.17 – 4.18**). [35-37, 41] An example is the lipid peroxidation, the product of which is harmful to membrane-associated proteins[42], causing damage to cell structures and their functionality until the reaction terminates.[43]

$$RH + OH^{\cdot} \longrightarrow R^{\cdot} + H_2O \quad (\mathbf{4.17})$$

$$RC(O)H + OH^{\cdot} \longrightarrow RC(O)\cdot + H_2O \quad (\mathbf{4.18})$$

Given the enhanced reactivity of $O_2^{\cdot-}$ and $OH^{\cdot}$ as compared to hydrogen peroxide H_2O_2, it is interesting to focus further on the nature of the chemistry involved in the ORR at silver since this lies at the heart of Ag nanoparticle toxicology. In particular the issue of whether the process leads to H_2O_2 *or* $O_2^{\cdot-}$ (protonated or otherwise) may have toxicological implications. Herein a fundamental understanding of the ORR in chloride containing media including

seawater was generated to explore the possible fate of silver nanoparticles in those media. Also, the fact that biological systems contain high levels of chloride, for example, saliva (10 to 43 mM)[44] and blood (96 to 106 mM)[45] was recognised, and the likely associated chemistry was focused on.

Thus, this chapter aims to explore ORR in aqueous chloride media including seawater on bulk silver electrodes, compare it with other aqueous salt solutions and assess any implications for the nanotoxicology of silver nanoparticles. Furthermore, the change of mechanism and of overall chemistry revealed below has implications for the effects of the silver in biological media which typically contain high chloride levels as well as in seawater.

4.2 Experimental

4.2.1 Chemical Reagents

All chemicals used are listed in **Table 3.1** and solutions were prepared with deionized water as stated in **Chapter 3**. Solutions were degassed with nitrogen gas (N_2) or oxygen gas (O_2) for 15 min prior to each voltammetric experiment. The gas flow during degassing was sufficiently fast such that the voltammetric features corresponding to a saturated level of N_2 or O_2 was consistently observed for each experiment.

4.2.2 Electrochemical Analysis

A Glassy Carbon macro-electrode (GC, radius 1.49 mm, BAS, Technical, UK) and a silver macro-disc electrode (Ag, homemade, radius 1.36 mm) were calibrated as described in **Appendix A** and used as working electrodes. The electrode preparation and the experimental set-up are fully described in **Section 3.1**.

4.2.3 Oxygen Reduction Reaction on Macro-electrodes

Cyclic voltammetry at various scan rates was performed to measure the kinetics of oxygen reduction on a macro glassy carbon and a macro silver WE. The experiments were conducted in the following freshly prepared solutions; oxygen saturated 0.1 M sodium perchlorate, 0.1 M potassium nitrate, 0.1 M and 0.42 M potassium chloride, simple synthetic seawater solution (0.42 M sodium chloride, 9.39 mM potassium chloride and 54.6 mM magnesium chloride) and synthetic seawater prepared using a standard recipe in literature.[46, 47] The analysed potential range was 0 V to –0.7 V for the potassium nitrate solution and 0 to –1.0 V for other solutions.

4.3 Results and Discussions

The ORR at both glassy carbon and silver electrodes was explored considering aqueous electrolyte ranging from chloride free to high chloride media such as seawater. The presence of chloride was shown to profoundly alter the mechanism of the reaction at silver electrodes with the formation of superoxide rather than hydrogen peroxide. The implications for nano-toxicology were assessed in the light of the inferred changed chemistry.

4.3.1 O_2 Reduction on Glassy Carbon Electrodes

Reduction of oxygen saturated solution (c_{O_2}=1.26 mM)[48] was performed on a glassy carbon macroelectrode in a simple synthetic seawater. The composition of the latter is given in **Table A.1** in **Appendix A** along with the composition of authentic seawater[46, 47] from which it can be seen that the solution studied contained the major components of seawater but that

minor components were excluded. Voltammograms were recorded for scan rates varying from 0.02 V s^{-1} to 0.4 V s^{-1} (**Figure 4.1**) and revealed broad irreversible reduction peaks at -0.5 V and −1.0 V at 0.05 V s^{-1} measured relative to a Ag/AgCl (c_{cl^-}= 3.5 M) reference electrode indicating the probable formation of hydrogen peroxide and water respectively in the two voltammetric features. This first voltammetric wave in seawater solution is consistent with the fully electrochemically irreversible Randles–Ševčík equation, assuming that the first electron transfer is rate-determining, where the variation of the peak current (I_p) with the square root of the scan rate (v) is:

$$I_p = 2.99 \times 10^5 n_{eff} \alpha^{1/2} A_{electrode} {D_{O_2}}^{1/2} c_{O_2} v^{1/2} \quad \textbf{(4.19)}$$

where n_{eff} is the effective number of electrons; α is the transfer coefficient of the rate-determining first electron transfer step; $A_{electrode}$ is the area of electrode surface; c_{O_2} is the concentration of oxygen and D_{O_2} is the diffusion coefficient of oxygen.

The square root dependence (**Figure 4.1a** inlay) suggests that the wave is largely diffusional in character. The solubility of pure oxygen was taken as 1.26 mM[48] and the transfer coefficient was evaluated as 0.61 (**Figure 4.1b**), giving the product of the effective number of electrons transferred and the square root of diffusion coefficient ($n_{eff} \cdot {D_{O_2}}^{0.5}$) a value of 1.50×10^{-5} m $s^{-0.5}$. The inlay of **Figure 4.1a** suggests that the second voltammetric wave is also largely diffusional.

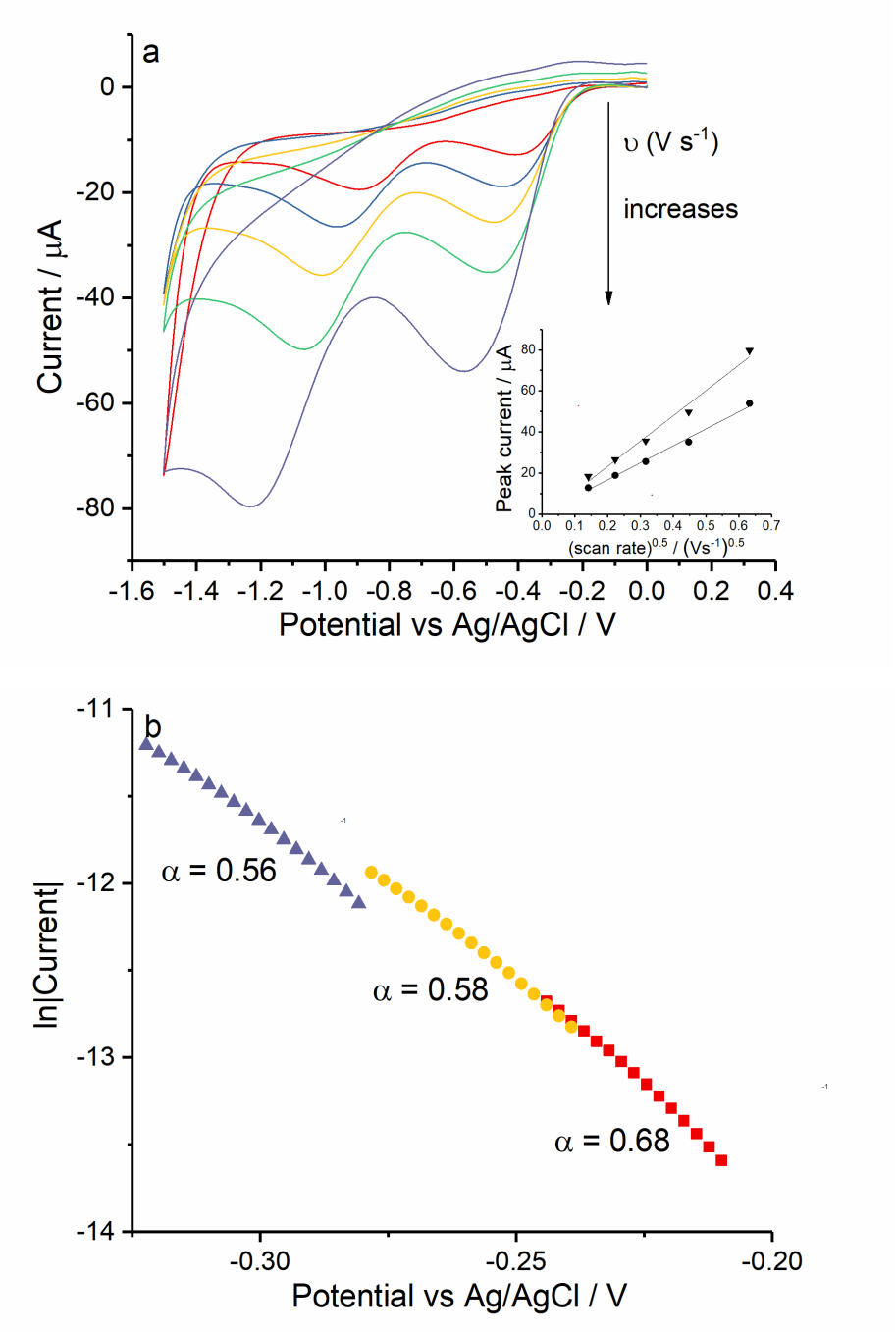


Figure 4.1 Oxygen reduction on glassy carbon in simple synthetic seawater (0.42 M NaCl, 9.39 mM KCl and 54.6 mM $MgCl_2$). a) Voltammograms from 0 V to -1.5 V at 0.02 V s^{-1}, 0.05 V s^{-1}, 0.1 V s^{-1}, 0.2 V s^{-1} and 0.4 V s^{-1}, the inlay shows the peak current varied with square root of scan rate for the first step (●) and the second (▼); b) The Tafel analysis for 0.02 V s^{-1}(red), 0.1 V s^{-1}(yellow) and 0.4 V s^{-1}(purple).

The diffusion coefficients of oxygen in various aqueous media are given in **Table A.2** (**Appendix A**). The values vary widely discouraging further quantitative analysis including

the separation of the number of electrons transferred and the diffusion coefficient. Moreover and in particular, comparison of experiment with the literature on the basis of GC electrodes is challenging due to the complexity of the pH dependency and the surface sensitivity of ORR pathways on a glassy carbon electrode. The influence of carbon centres at the electrode surface on mechanism and its pH responses has been reported by Zhang *et al.*[49], which not only presents the vital importance of the amount and oxidative condition of adsorption sites but also the possibility of parallel mechanisms under different pH conditions. In particular for synthetic seawater during the reduction process, hydroxide ions are generated near the electrode and since no buffer is present the local pH can be markedly changed which likely alters the mechanism as a function of both potential and possibly scan rate. Thus, quantitative analysis based on the simple Randles–Ševčík equation and associated Tafel analysis is potentially misleading. In the following section silver electrodes were studied where surface adsorption of reactive oxygen species is less likely.

4.3.2 O_2 Reduction on Silver Electrodes

The study of the ORR in seawater at silver electrodes mixes a potentially complex electrochemical mechanism, as discussed above, with a medium containing many different chemical species as is evident from **Table A.1** (**Appendix A**). The first step towards examining the reaction in seawater is to simplify the problem by analysing signals in electrolytes such as alkali metal nitrate and perchlorate solutions as is discussed in the following section.

(i) O_2 reduction on Ag electrodes in 0.1 M KNO_3 and 0.1 M $NaClO_4$

Reductive voltammetry studies in oxygen saturated 0.1 M KNO_3 and 0.1 M $NaClO_4$ were performed on a silver macroelectrode with varying scan rates from 0.02 V s^{-1} to 0.4 V s^{-1} (**Figure A.2, Appendix A**). Voltammograms for 0.05 V s^{-1} are plotted in **Figure 4.2**.

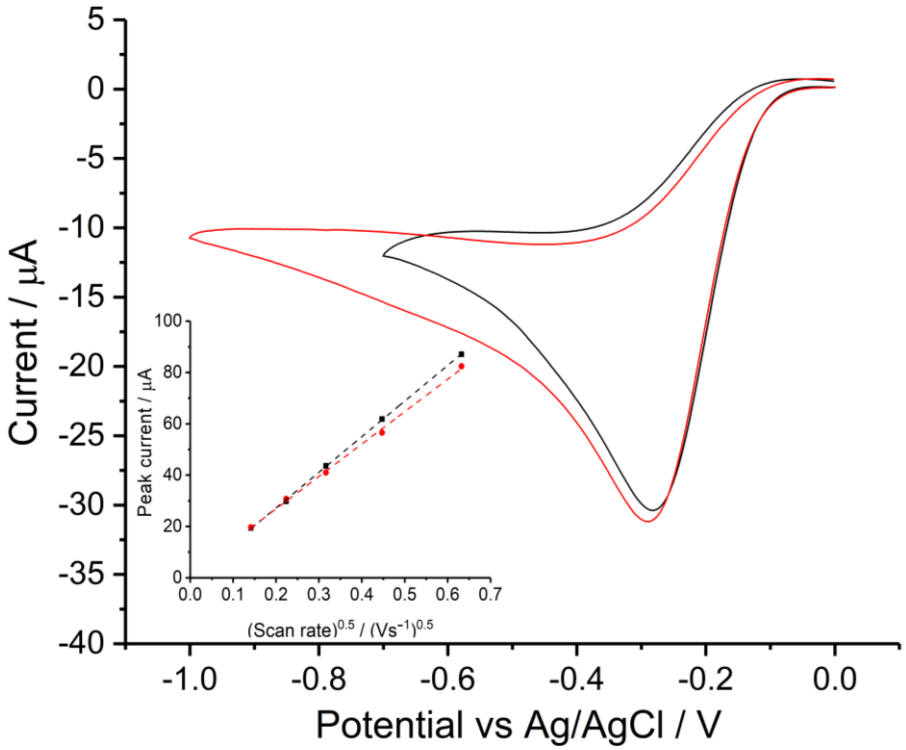


Figure 4.2 Oxygen reduction voltammograms at 0.05 V s^{-1} on bulk silver electrode. Cyclic voltammetry in 0.1 M KNO_3 (black) and 0.1 M $NaClO_4$ (red), inlay shows the peak current variation with square root of scan rate for 0.1 M KNO_3 (■) and 0.1 M $NaClO_4$ (●)

Consistency was found between the irreversible (voltammetrically and chemically)[50] peak in inert supporting electrolyte solutions of pure sodium perchlorate and pure sodium nitrate; both achieved a maximum current at -0.3 V vs Ag/AgCl (c_{Cl^-} = 3.5 M). Transfer coefficients were evaluated as 0.75 ± 0.03 and 0.69 ± 0.04 in KNO_3 and $NaClO_4$, respectively. The dependence of the peak current on scan rate followed the irreversible form of Randles–

Ševčík equation (**Figure 4.2** inlay). Analysis using the diffusion coefficient of $1.96\times10^{-9}m^2s^{-1}$[16] and oxygen solubility (1.26 mM) whilst noting the wide range of values in **Tables A.2 and A.4** (**Appendix A**) suggests a likely $2e^-$ transfer for the first reductive peak.

The results are consistent with a proposed mechanism with a rate-determining step producing superoxide followed by its fast reaction with water (**Reaction 4.4** and **4.5**) with a further electron transfer. Interestingly, whilst the use of pure oxygen to saturate the solution suggest the operation of a two-electron process, it has been noticed that in air-saturated solutions, containing roughly one fifth the level of dissolved oxygen, a larger number of electrons, n_{eff} =3.3[16] , is observed. A heterogeneous disproportionation of hydrogen peroxide leads to some water formation.[16] The difference may reflect different levels of proton release or a change in the silver surface the morphology of which is likely to markedly influence the heterogeneous disproportionation.

On the basis of the investigations obtained from simple electrolyte solutions, explorations of the ORR in authentic and synthetic seawater were next carried out.

(ii) O_2 reduction in seawater

To investigate the ORR mechanism in seawater, reduction of oxygen on a silver macro-disc electrode was carried out in standard synthetic seawater and filtered authentic seawater from Scotland (see **Table A.1** for chemical compositions) with varying scan rates from 0.02 V s^{-1} to 0.4 V s^{-1} (**Figure A.3** in **Appendix A**). Blank experiments in N_2 saturated both seawater solutions were performed at 0.4 V s^{-1}, overlaid with measurements in O_2 saturated solutions showing no significant Faradaic signals presenting without oxygen. (**Figure A.4** in **Appendix A**). Voltammograms for 0.05 V s^{-1} are plotted in **Figure 4.3**. The synthetic

seawater suitably mimics the authentic seawater sample. However, in comparison with the reduction wave observed in nitrate and perchlorate solutions, both voltammetric signals here are shifted to a higher overpotential by ca. 0.1 V and most interestingly split into separated peaks at -0.4 V and -0.6 V vs Ag/AgCl (c_{Cl^-} = 3.5 M).

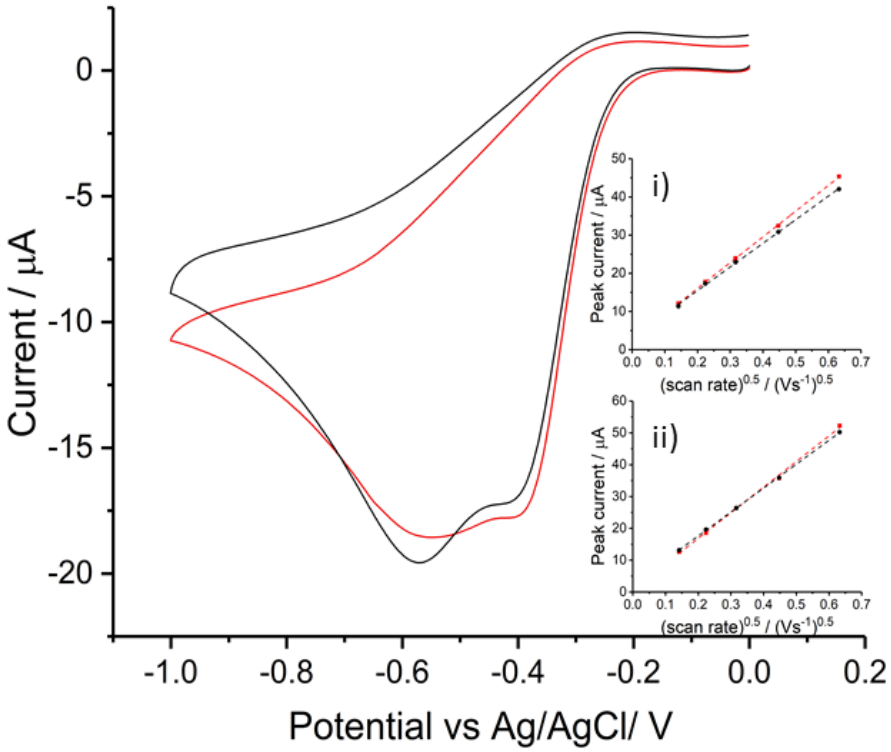


Figure 4.3 Oxygen reduction on silver in seawater. Voltammograms measured at a scan rate of 0.05 V s^{-1} in Scottish seawater (black) and synthetic seawater (red). Inlay figures present peak current varied with square root of scan rate for the first peak in i) and the second in ii)

Tafel analysis of the initial part of the voltammetric waves gave transfer coefficients of 0.71±0.05 in authentic seawater and 0.68±0.01 in synthetic seawater. This is in excellent agreement with Neumann *et al.*[16] who found that α = 0.7 in 0.1 M $NaClO_4$. Comparison of the magnitudes of the peak currents for oxygen saturated solutions between **Figure 4.2** and **4.3** suggests that the two-electron feature seen for the simple nitrate and perchlorate

electrolytes has split into two partly overlapping one electron features in addition to being shifted to higher overpotential. The first peak, necessarily approximately given the overlapping with the second peak, was analysed using the Randles-Sevcik equation. Using the above estimates of D_{O_2}=1.96×10^{-9} m^{2}s^{-1} [16] and c_{O_2} =1.26 mM together with the transfer coefficient values above, a *single* electron transfer process at -0.4 V in seawater was inferred. Similarly, values of n_{eff} = 1.05±0.07 (authentic seawater) and n_{eff} = 1.05±0.04 (synthetic seawater) for the second reduction reaction were inferred. Thus the two electron voltammetric wave seen for nitrate and perchlorate electrolytes splits into two waves in seawater and seawater-like media with the formation of superoxide inferred as the product of the first wave.

(iii) Digisim modelling of the voltammetry in synthetic seawater

Next, the commercial simulation software DigiSim[51] were used to confirm the split of a two-electron transfer process into two one-electron transfer peaks and investigate associated kinetic parameters. Experimental cyclic voltammograms as presented in **Figure 4.4** for synthetic seawater were modelled using the mechanism in **Reaction 4.4** and **4.5**.

Due to overlapping of peaks, the choice of values of the transfer coefficient and standard electrochemical rate constant data reported in **Table 4.1** correspond to the best-fit approximation of the cyclic voltammograms obtained over the full scan rate range in **Figure 4.4** using these parameters to fit each voltammogram. Notice that the second reduction process is irreversible and modelled within the Butler–Volmer formalism the current response is described by a combined parameter $k_0 \exp\left(\frac{\alpha E_f^0 F}{RT}\right)$[52, 53] where k_0 and E_f^0 are the electrochemical constant and formal potential for each reduction step.

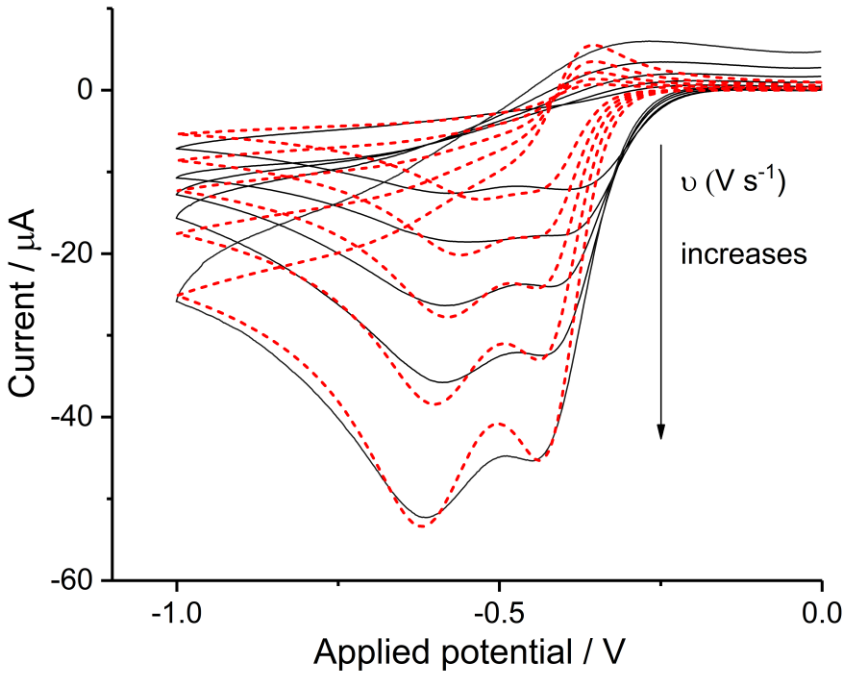


Figure 4.4 Digisim analysis of ORR in seawater. The fit of synthetic seawater cyclic voltammetry of scan rate at 0.02 V s^{-1}, 0.05 V s^{-1}, 0.1 V s^{-1}, 0.2 V s^{-1} and 0.4 V s^{-1}. Digisim fitting is plotted in red and experimental data in black.

A satisfactory fit of experimental (solid line) and simulated (dot line) is obtained with standard electron transfer rate constants k_0 of 1.0 cm s^{-1} and $k_0 \exp\left(\frac{\alpha E^0 F}{RT}\right) = 4.9 \pm 1.8\times10^{-11}$ cm s^{-1} for the 1st and 2nd peak respectively. The significant error in the latter value was from simulation of voltammogram at 0.02 V s^{-1}. In particular for the first wave, the high rate constant gave an apparent electrochemically quasi-reversible behaviour so that the value of 0.5 in **Table 4.1** simply reflects the modelling of the voltammetry rather than being a measurement of the Tafel coefficient. Herein, the precise value of transfer coefficient used is less important since in the limit of full reversibility the apparent transfer coefficient tends to unity.[54] The combination of a high k_0 and the assumed transfer coefficient gives a qualitatively good fit and the peak potential was well described by the set formal potential

i.e. -0.4 V vs Ag/AgCl, especially during fast scan rates. A consistent value of $E^0(O_2/O_2^{-\cdot})$ = - 0.395 V vs Ag/AgCl was reported by Baxendale *et al.*[55], similarly, $E^0(O_2/O_2^{-\cdot})$ = -0.385±0.02 V vs Ag/AgCl was determined for neutral solutions by Hoppenol *et al.* [56] Noticeably, the value of $E^0(O_2/O_2^{-\cdot})$ applied here is pH independent, and the follow up chemistry results in proton consumption.

Table 4.1. Electron transfer kinetics of the oxygen reduction at bulk silver at 298 K in synthetic seawater. [i]

Step 1		**Step 2**	
$\boldsymbol{\alpha}$	0.5	$k = k_0 \exp\left(\frac{\alpha E_f^0 F}{RT}\right)$ cm s^{-1}	$4.9 \pm 1.8\times10^{-11}$
$\boldsymbol{k_0}$ / cm s^{-1}	1.0		
$\boldsymbol{E_f^0}$ / V	-0.4		

Overall the voltammetry is consistent with the interpretation, as suggested in the previous section, of two partly overlapping diffusional voltammetric peaks corresponding first to the formation of superoxide and second to peroxide. The possible chemical cause for the split is considered in the next section which focusses on the role of the chloride ions present in seawater.

[i] k_0 and E_f^0 refer to the kinetic constant and the formal potential of each step; the values of k_0 and α for the first step are arbitrary to model a quasi-reversible behaviour.

(iv) The Cl^- concentration effect on the ORR at Ag electrodes

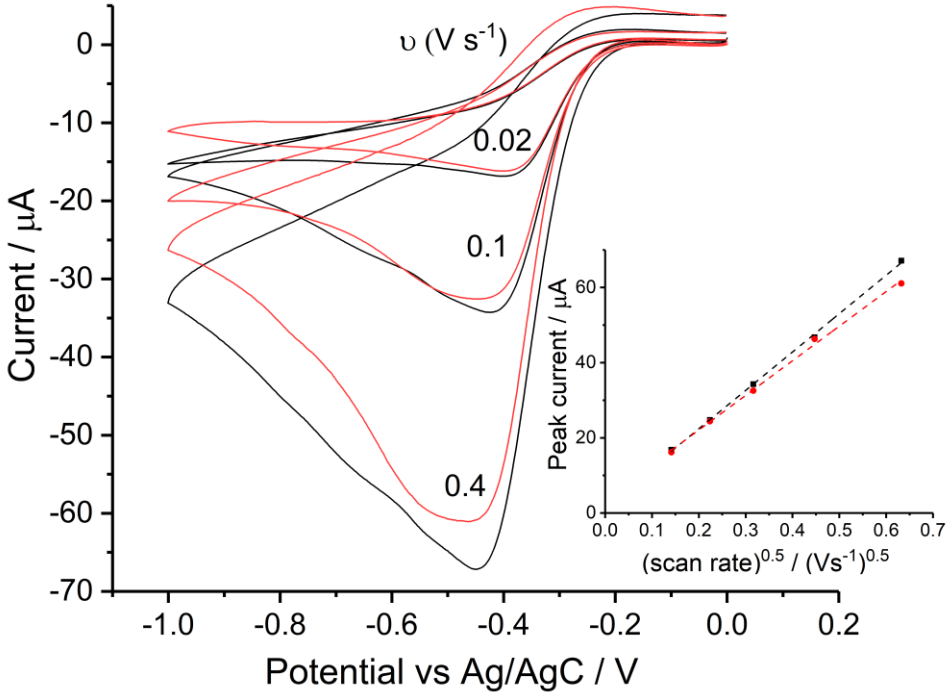


Figure 4.5 ORR on silver in potassium chloride solutions. Voltammograms measured at different scan rates in 0.1 M KCl (black) and 0.42 M KCl (red), inlay shows peak current varied with square root of scan rate for the signal.

In the light of the differences between the data shown in **Figure 4.2** and **Figure 4.3** in which the solution composition varied from chloride free to chloride rich, the reduction of oxygen on a silver macro-disc electrode was carried out first in aqueous potassium chloride solutions of 0.1 M and 0.42 M. Second solutions containing 0.42 M NaCl with KCl solution were studied and third a solution containing 0.42 M NaCl, 9.39 mM KCl and 54.6 mM $MgCl_2$. The latter corresponds to the levels of chloride, sodium, magnesium and potassium in seawater. Finally, oxygen reduction was conducted in 0.54 M KCl solution corresponding

to the total chloride level seen in seawater so as to clarify the role of chloride in the absence of Mg^{2+}.

Voltammograms in KCl solutions were recorded with varying scan rates from 0.02 V s^{-1} to 0.4 V s^{-1} as plotted in **Figure 4.5**. where in both solutions, despite the different chloride concentrations the reductive currents were essentially the same although there is a broadening of the peak at the higher chloride concentrations. Tafel analysis gives almost identical transfer coefficients of the two concentrations as listed in **Table 4.2**. Using the values of c_{O_2}=1.26 mM and D_{O_2}=1.96×10^{-9} m^2s^{-1}(assuming these are salinity independent in this modelling), the effective number of electrons transferred in 0.42 M KCl is noticeably smaller (1.33±0.15) as compared to 1.47±0.02 in 0.1 M KCl. Apart from the decrease in electrons transferred, the peak shifted to higher overpotential in 0.1 M KCl (-0.42±0.02 V) and 0.42 M KCl (-0.44±0.03V) as compared to the value of -0.30±0.05 V as observed in 0.1 M KNO_3 and -0.29±0.02 V in 0.1 M $NaClO_4$. Consequently, the clear split of the voltammetric peak seen in seawater was inferred to relate to additional species present in the latter, in addition to 0.42 M NaCl. Hence seawater level concentrations of KCl and $MgCl_2$ were added stepwise into 0.42 M NaCl solution.

Firstly, experiments were conducted in solution consisting 0.42 M NaCl and 9.39 mM KCl (**Figure 4.6 a**) and then with addition of 54.6 mM $MgCl_2$ (**Figure 4.6 c**) under the same scan rate range as above. As can be seen, a single reductive peak was recorded for all scan rates in the first solution whereas the further addition of magnesium chloride caused the splitting into two peaks. Given that the transfer coefficient is almost a constant in both cases (**Figure 4.6 b, d**), the only change observed in the voltammetric response was the decrease in

effective number of electrons transferred at the potential of the first peak, n_{eff} at -0.4 V (from 1.35±0.13 to 0.93±0.04).

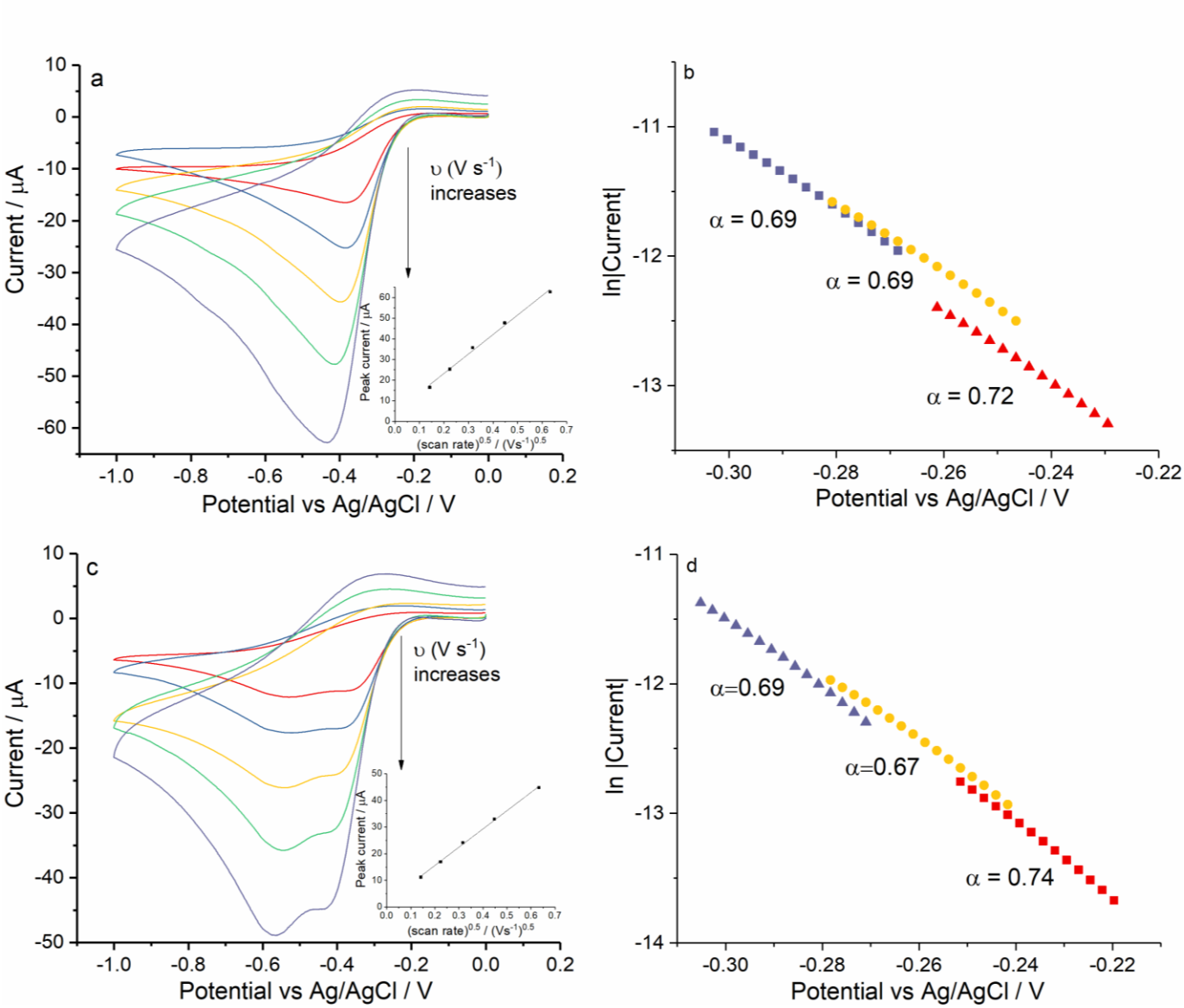


Figure 4.6 ORR at Ag electrodes for compositions approaching those of seawater. a) Voltammograms recorded in 0.42 M NaCl and 9.39 mM KCl or c) for 0.42 M NaCl, 9.39 mM KCl and 54.6 mM $MgCl_2$, measured at scan rates of 0.02 V s^{-1}, 0.05 V s^{-1}, 0.1 V s^{-1}, 0.2 V s^{-1} and 0.4 V s^{-1}. Inlay figures show the peak current variation with square root of scan rate for the signal, b) and d) show the Tafel analysis at 0.2 V s^{-1}, 0.1 V $s^{-1}$and 0.4 V s^{-1} for a) and c), respectively.

Table 4.2 Cl^- effect on Ag ORR reduction step.

Solution composition	c_{cl^-} / M	α	n_{eff}	Number of peaks
0.1 M KNO_3	0.00	0.75±0.03	1.64±0.03	1
0.1 M $NaClO_4$	0.00	0.69±0.04	1.65±0.02	1
0.1 M KCl	0.10	0.65±0.02	1.47±0.02	1
0.42 M KCl	0.42	0.66±0.05	1.33±0.15	1
0.42 M NaCl, 9.39 mM KCl, 54.6 mM $MgCl_2$	0.54	0.70±0.04	0.93±0.04	2
0.54 M KCl	0.54	0.67±0.02	1.07±0.10	2

Table 4.2 summarises the above described ORR results on silver and correlates the progressive increase in the chloride concentration with a decrease in the effective number of electrons transferred. Note that the transfer coefficient remains approximately constant throughout and suggestive of the quasi-reversible formation of superoxide. The apparent number of electrons transferred drops steadily with increased chloride concentration again signalling the developing formation of the superoxide ion ultimately in a distinct one electron wave. Overall, data in **Table 4.2** is consistent with a quasi-reversible formation of superoxide (**Reaction 4.4**) prior to the slowing of the **Reaction 4.5** followed up until the extent that in seawater two peaks appear. Interestingly the voltammetric waves seen in nitrate and perchlorate media are seen at less negative potentials than in chloride media. This suggests that the following chemical step occurs very rapidly under these conditions and the voltammetric reduction wave is shifted to less negative potentials. [52, 53]

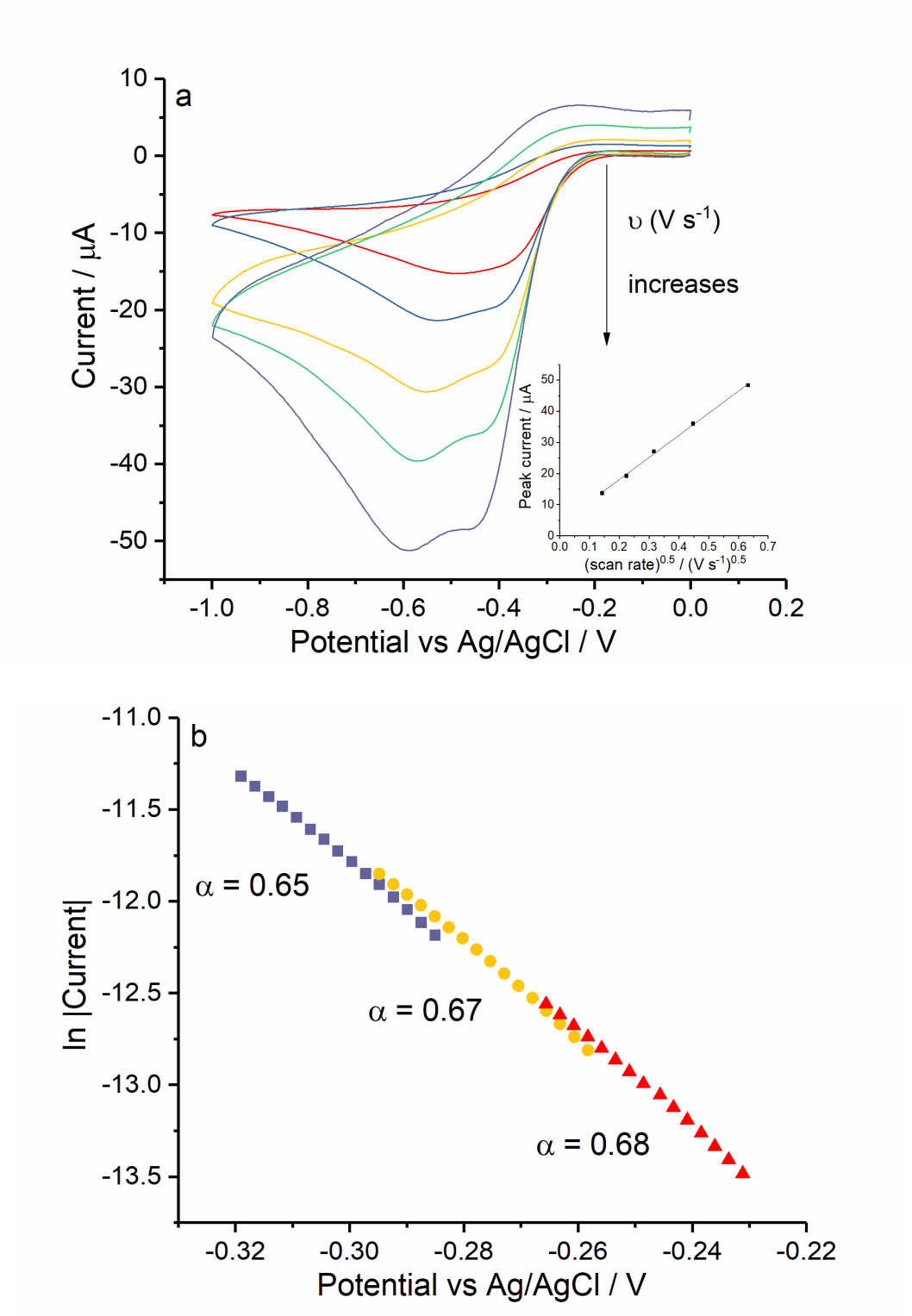


Figure 4.7 ORR at Ag electrodes in 0.54 M KCl. a) Voltammograms recorded in 0.54 M KCl measured at scan rates of 0.02 V s^{-1}, 0.05 V s^{-1}, 0.1 V s^{-1}, 0.2 V s^{-1} and 0.4 V s^{-1}, inlay shows the peak current variation with the square root of scan rate for the signal. b) The Tafel analysis for 0.02 V s^{-1}(red), 0.1 V s^{-1}(yellow) and 0.4 V s^{-1}(purple).

Lastly, control experiments in chloride concentrations equivalent to **Figure 4.6 d** (ca. 0.54 M KCl) were conducted in **Figure 4.7** to clarify if the peak splitting is due to the increased chloride level or the presence of Mg(II). Importantly, the splitting of the reduction wave and the potential of the first electron transferred in pure KCl solution are in line with that in the mixed solution (**Figure 4.6 d**). The transfer coefficient is comparable in 0.54 M KCl solution (0.67 ± 0.02) to that in the magnesium containing solution (0.70 ± 0.04), and the effective number of electrons transferred has a value of 1.07 ± 0.10 at -0.4 V. Moreover, possible effects from high ionic strength were excluded by performing the reduction of oxygen in 0.54 M KNO_3 at 0.02 V s^{-1} and 0.4 V s^{-1} where only a single two-electron wave was seen at a silver electrode (data not shown). Overall these experiments confirm that the presence of two peaks on silver is due to the chloride rich conditions rather than the presence of magnesium cations.

4.3.3 Physicochemical Origins of the Peak Splitting

The peak splitting requires the presence of very high concentrations of chloride for silver electrodes. It was noticed that chloride adsorption on silver has been widely reported.[57-60] The chloride can form adlayers on the silver electrode surface and significantly increase the double-layer capacitance.[58] Hence it is not surprising to find voltammetric signals at silver electrodes affected in concentrated chloride solutions like seawater (ca. 0.54 M Cl^-). However, since capacitive effects are apparent even at low concentrations of 1 mM, the simplest explanation of the effect is a slower follow up reaction[57-60] and the escape of the superoxide from the interface. The superoxide is formed at electrode potentials immediately negative of the thermodynamic reduction potential consistent with the quasi-reversible character of the observed voltammetry of the first peak in the split wave. The second peak

at ca -0.6 V in cyclic voltammetry reflects the change of the electrode mechanism. It is proposed that **Reaction 4.5** involves first a chemical step in which superoxide reacts with water to form hydroxide and $HO_2^{\cdot}$ radicals followed by electron transfer to $HO_2^{\cdot}$. If this chemical step is slowed at the chloride rich interface then this is consistent with the observation of electrochemically reversible superoxide formation. It is also consistent with the development of an overpotential as compared to chloride-free media (since the follow-up reactions which shift the reversible oxygen/superoxide wave to less negative potentials occur more slowly with high chloride concentrations). Finally, the absence of $HO_2^{\cdot}$ (and OH^- [61]) in the vicinity of the electrode prevents the second step from leading to hydrogen peroxide. Rather a different route to the formation of the latter occurs, at a more negative potential possibly as given in **Reaction 4.22** and **Figure 4.8**.

$$O_2 + e^- \rightleftharpoons O_2^{\cdot-} \quad (-0.4V) \qquad \textbf{(4.20)}$$

$$O_2^{\cdot-} \longrightarrow \text{Bulk (Diffusion)} \qquad \textbf{(4.21)}$$

$$O_2^{\cdot-} + H_2O + e^- \rightleftharpoons HO_2^- + OH^- \quad (-0.6V) \qquad \textbf{(4.22)}$$

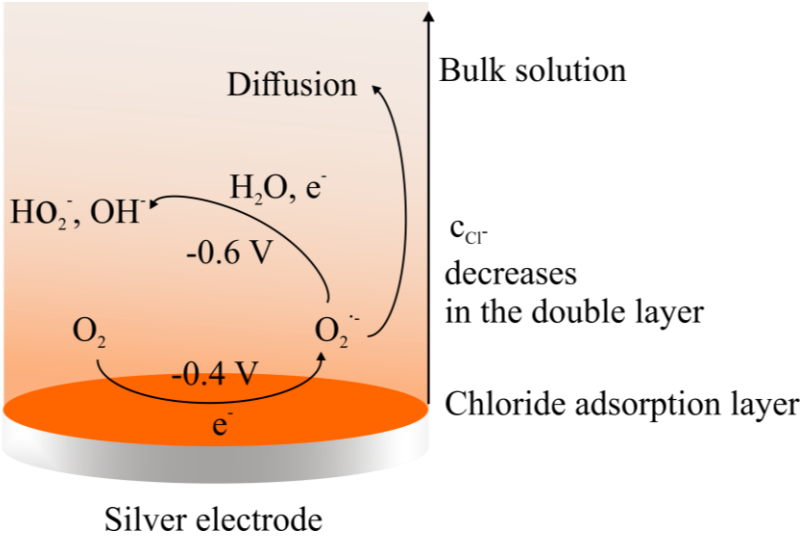


Figure 4.8 Schematic mechanism of the ORR on silver in chloride rich solutions

The above hypothesis relies on the detection of peak separation of ORR signals. There are also several additional methods that can detect superoxide to support the proposed mechanism during future work. First is the rotating ring disk electrochemistry (RRDE).[62]The RRDE consists of two electrodes separated by an insulator in between: a disc electrode locates at the centre and a ring electrode fitted outside it. Feng *et al.* detected superoxide intermediates during ORR reactions on a glassy carbon central disc with a gold ring electrode. [63] In this study of seawater, a silver central disc will be used to generate superoxide but the ring electrode requires specifically modification to capture superoxide under a fast diffusion rate and exclude the influence of chloride adsorption. The second possibility might be to couple *Infrared spectroscopy* or *Raman spectroscopy* with electrochemistry and detects intermediates simultaneously.[64] The in situ observation of adsorbed superoxide OOH_{ad} on Pt was achieved with IR spectra by Nayak *et al.* Comparation between spectra in seawater and 0.1M KNO_3 can possibly support the accelerated diffusion of superoxide in chloride solutions.

Another important question is to what extent can this mechanism be applied to silver electrodes with other surface morphology. It has been well studied that the ORR mechanism is sensitive to electrode surface morphology which demonstrates the surface coverage of adsorbed OH_{ad} during the reaction.[65] An example is the single-crystal silver which has a periodically repeating atomic structure as opposed to the polycrystalline one. The ordered surface means fewer defects that interact strongly with adsorbed OH_{ad} species thus the adsorption site for oxygen is sufficient to achieve higher electron transfer efficiency.[66] In particular, different silver single-crystal surfaces also influence the thermodynamics of the reduction reaction, with the activity increases in the order of $Ag(100) \leq Ag(111) < Ag(110)$[67]

Consequently, the findings from polycrystalline can not directly indicate possible observations for a single crystal silver electrode. However, some similarities may share between silver nanoparticles and the bulk silver electrode based on the significant amount of defects present at their multi-facets surfaces.

4.3.4 Implications for Silver Nanoparticle Toxicology

The above experiments show that the reduction of oxygen on silver results in most electrolyte solutions in an overall two-electron process leading to the formation of hydrogen peroxide. However in seawater which contains high levels of chloride the formation of superoxide ions has been evidenced. The mechanism proposed in the previous section on polycrystalline silver electrodes, in turn, suggests the likely release of superoxide in seawater during Ag nanoparticles dissolution and photoredox processes. It is noted that a previous study confirmed that the high concentration of chloride not only promotes dissolution of AgNPs by forming $AgCl_x^{(1-x)}$ [33] but also correlates to higher nanoparticle toxicity consistent with superoxide formation rather than the generation of the less toxic hydrogen peroxide. In addition, the dissolution of AgNPs under UV irradiation confirmed higher bacteria death rates in 0.5 M chloride solution as compared to the solution containing less chloride.[68] Despite fast aggregation of particles reported under high chloride concentration, the higher oxidative stress observed by Li *et al.* is thus possibly attributed to the increased production of superoxide, the major precursor of other ROS. Overall, silver nanoparticles in the presence of concentrated chloride may likely be more toxic, consistent with above-discussed experiments in seawater, though interpretations should be, of course, made very carefully when considering nanotoxicology in real cases.

4.4 Conclusions

The mechanistic study of oxygen reduction reaction in neutral chloride solution in particular seawater was conducted on a silver macrodisc electrode via cyclic voltammetry. Compared to alkaline metal nitrate solution, the reduction in seawater is shifted to higher overpotential and split into 2 steps. Simulation results from Digisim suggest the mechanism in seawater involves quasi reversible formation of the superoxide ion. Depending on the concentration of chloride present, further reduction of superoxide was slowed at least locally to the extent that superoxide escapes from the interface before it can react further on the voltammetric timescale, thus, ultimately for chloride levels above 0.5 M two peaks emerge signalling the formation of superoxide. Unlike ORR in nitrate or perchlorate solutions, the proposed mechanism implies superoxide formation in seawater, and indicates the likelihood of enhanced nanotoxicology of AgNPs in marine and in biological systems, which are typically of high chloride concentration. The findings of chloride sensitive voltammetric signals on a silver electrode spiked the idea of developing a particular chloride sensor for direct seawater in the next chapter

Bibliography

1. Y. J. Guo, M. J. Yang, R. C. Xie and R. G. Compton, *Chem. Sci.*, 2021, **12**, 397-406.
2. C. Hu and L. Dai, *Angew. Chem. Int. Ed. Engl.*, 2016, **55**, 11736-11758.
3. Y. Nie, L. Li and Z. Wei, *Chem. Soc. Rev.*, 2015, **44**, 2168-2201.
4. M. Shao, Q. Chang, J. P. Dodelet and R. Chenitz, *Chem. Rev.*, 2016, **116**, 3594-3657.
5. L. Dai, Y. Xue, L. Qu, H. J. Choi and J. B. Baek, *Chem. Rev.*, 2015, **115**, 4823-4892.
6. X. Ge, A. Sumboja, D. Wuu, T. An, B. Li, F. W. T. Goh, T. S. A. Hor, Y. Zong and Z. Liu, *ACS Catal.*, 2015, **5**, 4643-4667.
7. H. Erikson, A. Sarapuu and K. Tammeveski, *ChemElectroChem*, 2019, **6**, 73-86.
8. M. Chatenet, L. Genies-Bultel, M. Aurousseau, R. Durand and F. Andolfatto, *J. Appl. Electrochem.*, 2002, **32**, 1131-1140.
9. B. B. Blizanac, P. N. Ross and N. M. Marković, *J. Phys. Chem. B*, 2006, **110**, 4735-4741.
10. N. Ramaswamy and S. Mukerjee, *Adv. Phys. Chem.*, 2012, **2012**, 491604.

11. J. M. Linge, H. Erikson, A. Kasikov, M. Rähn, V. Sammelselg and K. Tammeveski, *Electrochim. Acta*, 2019, **325**, 134922.
12. L. Tammeveski, H. Erikson, A. Sarapuu, J. Kozlova, P. Ritslaid, V. Sammelselg and K. Tammeveski, *Electrochem commun*, 2012, **20**, 15-18.
13. A. Treshchalov, H. Erikson, L. Puust, S. Tsarenko, R. Saar, A. Vanetsev, K. Tammeveski and I. Sildos, *J. Colloid Interface Sci.*, 2017, **491**, 358-366.
14. D. Sepa, M. Vojnovic and A. Damjanovic, *Electrochim. Acta*, 1970, **15**, 1355-1366.
15. A. Qaseem, F. Y. Chen, X. Q. Wu and R. L. Johnston, *Catal. Sci. Technol.*, 2016, **6**, 3317-3340.
16. C. C. M. Neumann, E. Laborda, K. Tschulik, K. R. Ward and R. G. Compton, *Nano Res.*, 2013, **6**, 511-524.
17. P. K. Adanuvor, *J. Electrochem. Soc.*, 1988, **135**, 2509-2517.
18. J. Pulit-Prociak and M. Banach, *Open Chem.*, 2016, **14**, 76-91.
19. S. M. Dizaj, F. Lotfipour, M. Barzegar-Jalali, M. H. Zarrintan and K. Adibkia, *Mater. Sci. Eng. C*, 2014, **44**, 278-284.
20. G. Franci, A. Falanga, S. Galdiero, L. Palomba, M. Rai, G. Morelli and M. Galdiero, *Molecules*, 2015, **20**, 8856-8874.
21. A. J. Huh and Y. J. Kwon, *J. Control Release*, 2011, **156**, 128-145.
22. H. H. Lara, E. N. Garza-Treviño, L. Ixtepan-Turrent and D. K. Singh, *J. Nanobiotechnology*, 2011, **9**, 30.
23. R. Vazquez-Muñoz, B. Borrego, K. Juárez-Moreno, M. García-García, J. D. Mota Morales, N. Bogdanchikova and A. Huerta-Saquero, *Toxicol. Lett.*, 2017, **276**, 11-20.
24. P. L. Nadworny, J. Wang, E. E. Tredget and R. E. Burrell, *J. Inflamm.*, 2010, **7**, 13.
25. P. A. Holden, J. P. Schimel and H. A. Godwin, *Curr. Opin. Biotechnol.*, 2014, **27**, 73-78.
26. S. Tang and J. Zheng, *Adv. Healthc. Mater.*, 2018, **7**, 1701503.
27. N. Beyth, Y. Houri-Haddad, A. Domb, W. Khan and R. Hazan, *Evid. Based Complementary Altern. Med.*, 2015, **2015**, 246012.
28. C. Marambio-Jones and E. M. V. Hoek, *J Nanopart Res*, 2010, **12**, 1531-1551.
29. D. V. Navolotskaya, H. S. Toh, C. Batchelor-McAuley and R. G. Compton, *ChemistryOpen*, 2015, **4**, 595-599.
30. B. J. Plowman, K. Tschulik, E. Walport, N. P. Young and R. G. Compton, *Nanoscale*, 2015, **7**, 12361-12364.
31. K. Ngamchuea, C. Batchelor-McAuley and R. G. Compton, *Nanotoxicology*, 2018, **12**, 305-311.
32. Y. N. Slavin, J. Asnis, U. O. Häfeli and H. Bach, *J. Nanobiotechnology*, 2017, **15**, 65.
33. C. Batchelor-McAuley, K. Tschulik, C. Neumann, E. Laborda and R. G. Compton, *Int. J. Electrochem. Sci.*, 2014, **9**, 1132.
34. F. W. Campbell, S. R. Belding, R. Baron, L. Xiao and R. G. Compton, *J. Phys. Chem. C*, 2009, **113**, 9053-9062.
35. J. Lee, N. Koo and D. B. Min, *Compr Rev Food Sci F*, 2004, **3**, 21-33.
36. R. A. Larson and J. M. McCord, *Crit Rev Environ Sci Technol*, 1978, **8**, 197-246.
37. A. M. Pisoschi and A. Pop, *Eur. J. Med. Chem.*, 2015, **97**, 55-74.
38. H. J. Forman and N. Haugaard, *Trends Biochem Sci*, 1982, **7**, 279-279.
39. M. B. Koryckadahl and T. Richardson, *Crc Cr Rev Food Sci*, 1978, **10**, 209-241.
40. M. Yang, C. Batchelor-McAuley, L. Chen, Y. Guo, Q. Zhang, R. E. M. Rickaby, H. A. Bouman and R. G. Compton, *Chem Sci*, 2019, **10**, 7988-7993.
41. G. Buonocore, S. Perrone and M. L. Tataranno, *Semin Fetal Neonatal Med*, 2010, **15**, 186-190.
42. J. C. M. Riley and H. R. Behrman, *P Soc Exp Biol Med*, 1991, **198**, 781-791.
43. B. Kalyanaraman, *Redox Biol.*, 2013, **1**, 244-257.
44. J. H. Thaysen, N. A. Thorn and I. L. Schwartz, *The American journal of physiology*, 1954, **178**, 155-159.

45. H. K. Walker, W. D. Hall and J. W. Hurst, in *Clinical Methods: The History, Physical, and Laboratory Examinations*, eds. H. K. Walker, W. D. Hall and J. W. Hurst, Butterworths, Boston, 3rd edn., 1990, ch. 197.
46. F. M. M. Morel, J. G. Rueter, D. M. Anderson and R. R. L. Guillard, *J. Phycol.*, 2008, **15**, 135-141.
47. N. M. Price, G. I. Harrison, J. G. Hering, R. J. Hudson, P. M. V. Nirel, B. Palenik and F. M. M. Morel, *Biol. Oceanogr.*, 1989, **6**, 443-461.
48. K. Shimizu, L. Sepunaru and R. G. Compton, *Chem. Sci*, 2016, **7**, 3364-3369.
49. H. Zhang, C. Lin, L. Sepunaru, C. Batchelor-McAuley and R. G. Compton, *J. Electroanal. Chem.*, 2017, **799**, 53-60.
50. J. M. Savéant and C. Costentin, in *Elements of Molecular and Biomolecular Electrochemistry*, 2019, DOI: 10.1002/9781119292364.ch2, pp. 81-181, 285-381, 383-437.
51. *DigiSim (Professional version 3.0b)*, Bioanalytical Systems, Inc., West Lafayette, 2013.
52. A. J. Bard, *Electrochemical methods : fundamentals and applications*, Wiley, New York, 1980.
53. R. G. Compton and C. E. Banks, *Understanding voltammetry*, Imperial College Press, London, 2011.
54. W. J. Albery and W. Albery, *Electrode Kinetics*, Clarendon Press, 1975.
55. J. H. Baxendale, M. D. Ward and P. Wardman, *Trans Faraday Soc*, 1971, **67**, 2532-2537.
56. W. H. Koppenol, D. M. Stanbury and P. L. Bounds, *Free Radic. Biol. Med.* , 2010, **49**, 317-322.
57. G. Aloisi, A. M. Funtikov and T. Will, *J. Electroanal. Chem.*, 1994, **370**, 297-300.
58. V. I. Birss and C. K. Smith, *Electrochim. Acta*, 1987, **32**, 259-268.
59. B. M. Jović, V. D. Jović and D. M. Dražić, *J. Electroanal. Chem.*, 1995, **399**, 197-206.
60. M. S. Zei, *J. Electroanal. Chem. Interf. Electrochem.*, 1991, **308**, 295-307.
61. B. B. Blizanac, P. N. Ross and N. M. Markovic, *Electrochim. Acta*, 2007, **52**, 2264-2271.
62. Z. Jia, G. Yin and J. Zhang, in *Rotating Electrode Methods and Oxygen Reduction Electrocatalysts*, eds. W. Xing, G. Yin and J. Zhang, Elsevier, Amsterdam, 2014, pp. 199-229.
63. Z. Feng, N. S. Georgescu and D. A. Scherson, *Analytical Chemistry*, 2016, **88**, 1088-1091.
64. S. Nayak, I. J. McPherson and K. A. Vincent, 2018, **57**, 12855-12858.
65. N. A. Shumilova, G. V. Zhutaeva and M. P. Tarasevich, *Electrochim Acta*, 1966, **11**, 967-974.
66. P. Singh and D. A. Buttry, *The Journal of Physical Chemistry C*, 2012, **116**, 10656-10663.
67. B. B. Blizanac, P. N. Ross and N. M. Marković, *The Journal of Physical Chemistry B*, 2006, **110**, 4735-4741.
68. Y. Li, J. Zhao, E. Shang, X. Xia, J. Niu and J. Crittenden, *Environmental science & technology*, 2018, **52**, 4842-4849.

Chapter 5

A Bespoke Chloride Sensor for Seawater: Simple and Fast with A Silver Electrode

The distinctive electrochemical ORR signals on a silver macrodisc electrode were discussed in **Chapter 4**. Herein such signals are introduced in the direct chloride detection of natural seawater samples.

Chloride quantification in natural seawater is important in both oceanography and corrosion science. A bespoke electrochemical method was developed for a facile and accurate chloride sensor specifically for use for the high chloride levels encountered in seawater (ca 0.5 M). This is based on the voltammetric oxidation of a silver electrode over a well-defined potential range corresponding to AgCl nucleation/formation. The peak current for silver chloride formation varies linearly with chloride concentration in the range 0.484 M to 0.624 M provided the electrode is suitably activated. In particular, the reduction of dissolved oxygen was found to clean the surface and also to provide a stable peak potential against which other potentials can be referenced if it is wished to use a quasi-reference electrode. Thus, the overall voltammetric scan embraces first the reduction of oxygen followed by silver chloride formation and stripping. Reliable quantification was achieved in synthetic seawater with this methodology. Furthermore, the chloride anion concentration in three different authentic samples of natural seawater was measured accurately giving excellent agreement with independent analysis.

The work presented in this Chapter has been published as a first author paper in *Talanta*[1] with the help of the gift of a sample of seawater collected near Plymouth from Dr Samuel Barton and

the gift of a sample of Bermuda seawater donated by Prof. Heather Bouman both of the Department of Earth Science, Oxford University.

5.1 Introduction

Seawater compositions vary as a result of their biological content as well as reflecting local coastal industry and geology. **Table 5.1**, in which the number of significant figures presented is the same as reported in the literature[2], shows the typical inorganic composition of surface seawater per kg with 35.00 g total dissolved salts at 293 K (not specific for any particular ocean). From which it can be seen that many ions are present with the chloride anion the dominant species.

Table 5.1 Concentrations of major ions in surface seawater[2]

Composition	**Concentration / mM**
Na^+	4.8061×10^{2}
Mg^{2+}	5.413×10
Ca^{2+}	1.052×10
K^+	1.046×10
Sr^{2+}	9.2×10^{-2}
Cl^-	5.5939×10^{2}
SO_4^{2-}	2.8935×10^{1}
HCO_3^-	1.891
CO_3^{2-}	1.89×10^{-1}
Br^-	8.63×10^{-1}
F^-	7.0×10^{-2}
$B(OH)_4^-$	8.39×10^{-2}
$B(OH)_3$	3.42×10^{-1}

Importantly the local chloride concentration in seawater depends on location and season.[3, 4] In turn the chloride level influences the oxidation of toxic contaminants in marine environments such as Hg^0 and AgNPs.[5-7] At high chloride concentrations, such oxidative dissolution becomes

easier as soluble chloride complexes of Hg(II) and Ag(I) can be formed.[8-10] Further, the marine chloride level is an important factor for electrochemical and atmospheric corrosion in coastal area constructions.[11, 12] The chloride stress affects materials such as steels even inside reinforced concrete structures.[11, 13, 14] Monitoring the specific chloride level in natural seawater systems is of vital importance in both oceanography and corrosion science.

The chloride concentration in seawater has been defined for many years via the term 'chlorinity'.[15, 16] The definition of chlorinity (Cl, g kg^{-1}, ppt or ‰) is the weight in grams of silver that will react with the halides in 328.5233g of seawater.[17] Originally chlorinity was measured to *estimate* the amount of total salts dissolved in seawater. The latter quantity reflects the so-called salinity of the water.[18] Perusal of **Table 5.1** suggests that this is a major approximation! Moreover, measurement of salinity, as is now widely undertaken, necessarily neglects the specific chemical effects of chloride, notably in respect of complexation and in corrosion. For neutral solutions, the traditionally used method for measuring chlorinity is the argentometric method (Mohr's method)[19, 20]; potassium chromate is used to colorimetrically indicate the endpoint of adding silver nitrate. Invented more than a century ago, the method provides good accuracy in skilled hands but uses toxic (and expensive) materials, is time-consuming and is necessarily usually conducted remotely from the point of sampling. Meanwhile, a potentiometric titration method was reported using glass and silver chloride electrodes to detect the end point of the titration of seawater again with silver nitrate solution.[21-23] Potential difference measurements are easier and more precise to determine than colour changes, though both titration methods have the drawbacks of needing large sample volumes and the introduction of toxic chemicals.

Modern approaches to the measurement of chlorinity (Cl, g kg^{-1}, ppt or ‰) prefer instrumental rather than wet methods. This comes at the expense of making the approximation that the

salinity (*S*, g kg^{-1}, ppt or ‰) reflects the chlorinity. Salinity is found using the polynomial conductivity correlation recommended by UNESCO[24, 25] (**Equation 5.1**).

$$S(‰) = a_0 + a_1 K_{15}^{1/2} + a_2 K_{15} + a_3 K_{15}^{3/2} + a_4 K_{15}^{2} + a_5 K_{15}^{5/2} \qquad 2 \leq S \text{ (g kg}^{-1}) \leq 42 \qquad \textbf{(5.1)}$$

where

$$K_{15} = \frac{conductivity\ of\ Standard\ Seawater\ at\ 15°C \text{ and } 1 \text{ standard atmosphere}}{conductivity\ of\ KCl\ solution\ (32.4356 g\ KCl\ per\ kg\ solution) at\ 15°C \text{ and } 1 \text{ standard atmosphere}}$$

and

$a_0 = 0.0080$, $a_1 = -0.1692$, $a_2 = 25.3851$, $a_3 = 14.0941$
$a_4 = -7.0261$, $a_5 = 2.7081$, $\sum a_i = 35.0000$

Then in order to find the chlorinity an empirical conversion from salinity is made using the Knudsen equation (**Equation 5.2**).

$$S(\text{g kg}^{-1}) = 1.80665\ Cl(\text{g kg}^{-1}) \qquad \textbf{(5.2)}^{16}$$

Therefore the inferred chloride concentration relies on salinity data which in turn requires conductivity measurements which necessarily reflect more the total ion content (**Table 5.1**) albeit partly reflecting the different single ion conductivities.[3, 19, 25] Thus ocean salinity indicates approximately the totality of all dissolved salts per kg seawater.[26] It can be either calculated from the electrical conductivity of sample solutions or measured via a salinometer, an instrument that detects and immediately converts the conductivity and temperature of given samples into salinity readings.[27] The conductivity method is portable, but the conversion involves the (extreme) assumption of using potassium chloride (KCl) solutions to approximate seawater[15] and is unable to report specific chloride content.

A new analytical technique that is rapid, simple to use and, if needed, portable with no toxic waste and which directly measures the concentration of chloride is expected to have a major impact. Herein, a fast, robust and facile electrochemical method was presented utilising the

silver chloride (AgCl) formation reaction (**Reaction 5.3**) on a silver macro electrode to sense the chloride concentration accurately.

$$AgCl_{(s)} + e^- \rightleftharpoons Ag + Cl^- \; ; E^o = 0.2223 \text{ V} \quad (\mathbf{5.3})^{28}$$

$$O_2 + e^- \rightleftharpoons O_2^{\cdot -} \; ; E^o = -0.33 \text{ V} \quad (\mathbf{5.4})^{28}$$

$$O_2^{\cdot -} \longrightarrow \text{Bulk (Diffusion)} \quad (\mathbf{5.5})$$

$$O_2^{\cdot -} + H_2O + e^- \rightleftharpoons HO_2^- + OH^-; E^o = 0.20 \text{ V (pH} > 11.6) \quad (\mathbf{5.6})^{28, 29}$$

Amperometric quantification of halides has been previously studied in low analyte concentrations,[30-33] but our new method requires a sample of as little as 3.0 mL filtered seawater and does not require dilution. It is developed specifically for use in undiluted seawater samples. In the method, the oxygen reduction reaction (ORR, **Reaction 5.4–5.6**)[34] is measured voltammetrically and simultaneously with AgCl formation which siutable for seawater. As previously reported[34], oxygen reduction on silver electrodes in chloride rich neutral solutions such as seawater shows clear voltammetric responses, the potentials of which are shown below to be insensitive to salinity or the chloride ion content. The magnitude of the ORR current response gives a measure of the dissolved oxygen content but more importantly, the peak potential provides an 'internal reference electrode' against which the potential range explored can be reproducibly realised. Furthermore, and critically, potential scanning embracing the ORR reaction is shown to activate the electrode surface and to remove any residual AgCl at the electrode surface. Lastly, it is important to clarify that the proposed reactions are based on neutral solutions and are also capable of global seawater pH values in recent decades (8.0 ~ 8.25).[35] As discussed in **Section 2.3** and Pourbaix diagram **Figure 2.4**, the silver chloride deposition and stripping are pH independent so is the oxygen/superoxide redox couple. The only pH sensitive reaction during ORR reaction is described in **Reaction 5.6** where a high local

concentration of hydroxide will build up during the reaction in absence of sufficient buffer ions. Compared to local pH variations, the slight changes in seawater pH value is less significant and will not change the mechanism nor the potential of the superoxide. Consequently, the reported electrochemical method for detecting chloride concentrations provides essential information for the global seawater pH range for seawater chemistry and corrosion analysis.

5.2 Experimental

5.2.1 Chemical Reagents

All chemicals were listed in **Table 2.1**. Natural seawater samples (500 mL, filtered) were each supplied by SAMS (Scottish Marine Institute, Argyll, UK), collected from the L4 station (50° 15.00' N, 4° 13.02' W), off the coast of Plymouth (Western Channel Observatory) or collected from Bermuda 2 km deep in the sea. The spherical citrate-AgNPs ca.100 nm diameter (Nanoxact, 0.02 mg mL^{-1} silver, 2 mM sodium citrate) were purchased from Nanocomposix, USA. For voltammetry analyzing silver chloride peaks in the absence of oxygen, solutions were rigorously degassed with nitrogen gas (N_2, 99.998%, BOC Gases plc, Guildford, UK). The nitrogen flow was sufficiently fast to ensure saturated level of N_2 for voltammetric consistency in each scan with no detectable ORR peaks. For voltammetry analyzing both silver chloride peaks and ORR signals, solutions (3.0 mL) were stirred (400 rpm) in open to air for 15min to ensure saturation of air each time. All the solutions were prepared using Millipore water with a resistivity of 18.2 MΩ cm at 298 K.

5.2.2 Electrochemical Analysis

All electrochemical measurements were performed in a conventional three-electrode cell consisting of a platinum wire counter electrode, a Ag/AgCl reference electrode (in saturated KCl solution) and a working electrode (WE). A glassy carbon macro-electrode (GC, radius 1.49 mm, BAS, Technical, UK) calibrated in **Appendix A** or a silver macro-disc electrode (Ag, homemade, radius 1.13 mm) calibrated as described in **Appendix B** (**Figure B.1**) were used as working electrodes. Both electrodes were polished using a sequence of 1.0, 0.3 and 0.05 micron alumina lapping compounds (Bucher, Germany). Measurements were performed using a μAutolab II potentiostat (Metrohm-Autolab BV, Utrecht, Netherlands) under 298 K. A constant temperature of 298±0.5 K was maintained by a thermostated water bath.

(i) Chloride detection on a silver macro-electrode

First, cyclic voltammetry at various scan rates was performed to monitor both monolayer and bulk silver chloride formation at a macro silver WE. The experiments were conducted in freshly prepared nitrogen saturated 0.564 M sodium chloride (NaCl) solution. The electrode was held at -1.0 V for 1min before each scan. The analysed potential range was -0.15 V to +0.060 V for the monolayer and -0.15 V to +0.086 V for bulk silver chloride formation and stripping peaks.

Next, the silver chloride peak sensitivity to chloride concentration was studied voltammetrically in air saturated NaCl solutions and seawaters. The method was first undertaken with air saturated 0.564 M NaCl at 0.1 V s^{-1} scanning from -0.20 V to -0.75 V then anodically to +0.086 V before returning to -0.20 V and holding for 1min to remove remaining silver chloride. Second, experiments examined freshly prepared sodium chloride solutions (0.500 M to 0.578 M) at a scan rate of 0.02 V s^{-1} using the slightly adjusted potential range of -0.20 V to +0.093 V for direct silver chloride formation and -0.75 V to +0.093 V for silver

chloride formation with a simultaneous ORR measurement. Similarly, voltammetric detections of chloride in synthetic seawater and natural seawater were performed at 0.02 V s^{-1} within a potential range of -1.0 V and +0.10 V. The synthetic seawater of variable salinity (31‰ to 38‰) was prepared using different amounts of sodium chloride following a literature recipe (**Table B.1, Appendix B**).[36, 37] Meanwhile, to investigate if scanning to potentials corresponding to the ORR can activate the electrode surface, three sets of successive experiments were conducted in air-saturated 0.546 M NaCl at 0.02 Vs^{-1} at a temperature of 293 K. Each scan was performed with an air-saturated solution *without* electrode mechanical polishing in between. Seven successive scans each started directly from -0.20 V and swept towards +0.093 V and reversed were conducted in control experiments. Fifteen successive scans each started directly from -0.20 V and swept towards +0.093 V and reversed followed by a 1 min holding at -0.20 V to test the single step potential cleaning method. Last, three successive scans each started from -0.20 V and swept negative to -1.0 V, then reversed to +0.093 V and terminated at -0.20 V were conducted in the depositions after ORR measurements.

(ii) Chloride detection with silver nanoparticles

3.0 mL uniformly dispersed commercial AgNPs solution (0.02 mg mL^{-1}) was washed with ultrapure water twice. The solution was centrifuged at 400 rpm for 10 min and 2.0 mL of the supernatant was removed and replaced with a further 2.0 mL ultrapure water for two repetitions. The final suspension was made up to a total of 3.0 mL to retain the same concentration as that before washing, and the washed AgNPs sample was dispersed by sonication for 1min before drop-casting onto the electrode. Specifically, after polishing the glassy carbon macro-electrode, 7.0 μL of washed AgNPs was applied to the electrode surface and dried at 343 K for 10min

(**Figure 5.1**). The electrode was then used to detect chloride levels in synthetic seawater with a salinity of 31 g kg^{-1} and 38 g kg^{-1}.

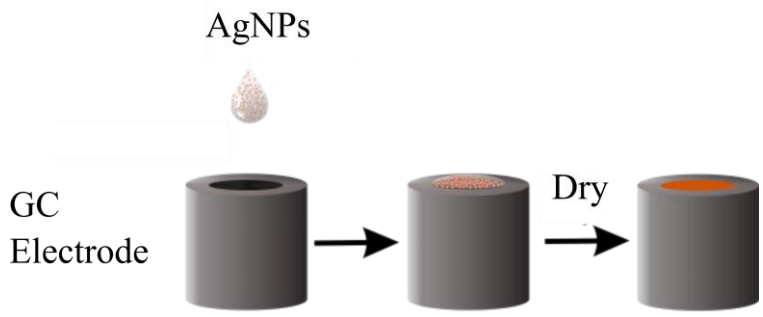


Figure 5.1 Schematic diagram showing drop-casting of silver nanoparticles on a GC electrode surface.

(iii) Chloride titration of natural seawater samples

The so-called argentometric method was performed following a well-established procedure[22]. Silver nitrate solution with a concentration of 0.0141 M was freshly prepared and standardized with 0.0141 M sodium chloride. Natural seawater was diluted 100 times into 50.0 mL and 0.25 M potassium chromate (1.0 mL) was added afterwards. The final solution was stirred at 500 rpm and titrated slowly until the pinkish-yellow end-point.

5.3 Results and Discussions

The possible use of bulk silver chloride formation on silver electrodes for the quantification of chloride at the very high concentration levels present in authentic seawater was explored (see **Table 5.1**). The voltammetric basis for our approach is plotted in **Figure 5.2** which shows a voltammetric scan in 0.564 M NaCl at 0.1 V s^{-1} starting at -0.20 V, sweeping negative to

-0.75 V and then anodically to +0.086 V before returning to the start voltage. Several voltammetric features are observed.

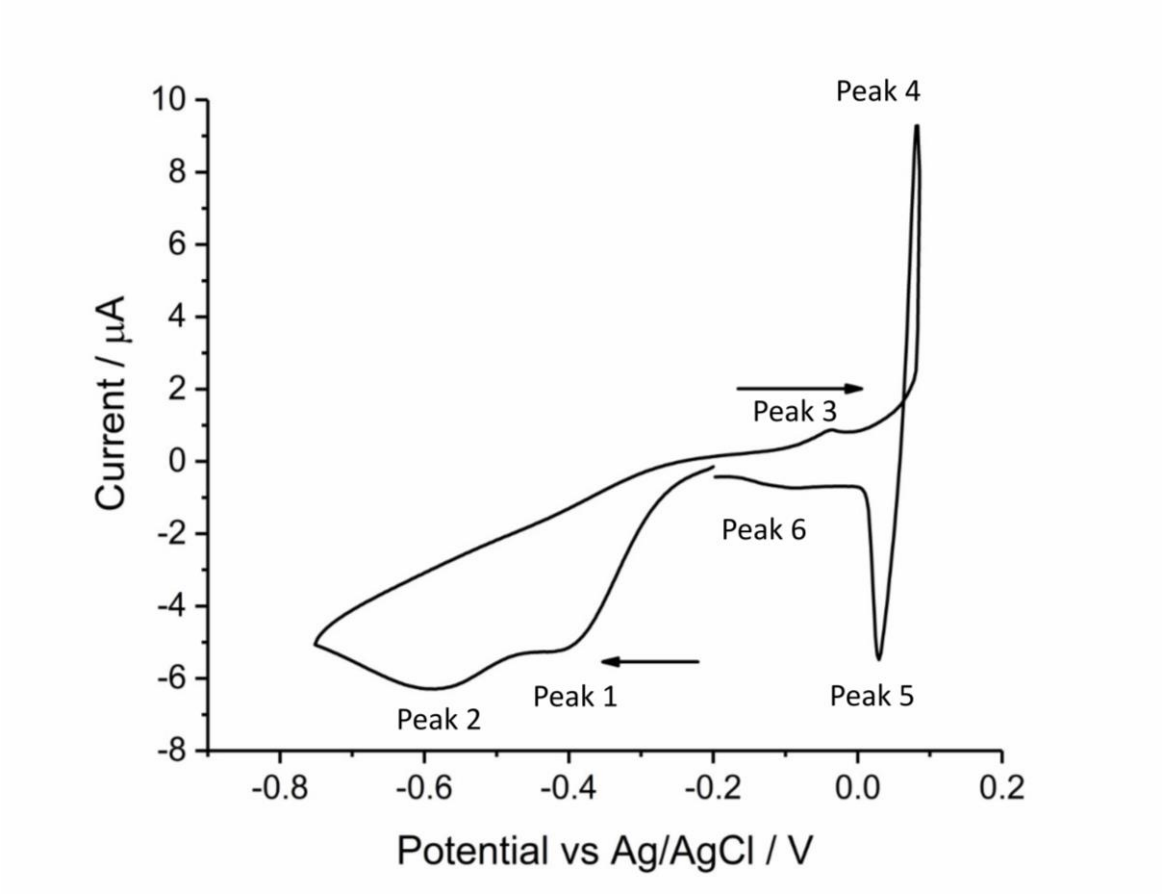


Figure 5.2 AgCl formation and stripping voltammetry after a scan first embracing ORR at 0.1 Vs^{-1} in air-saturated 0.564 M NaCl solution at a silver macro-disc electrode r=1.13 mm at 298 K, scanning from -0.20 V to -0.75 V followed by a reverse scan to +0.086 V then back to -0.20 V.Voltammetric peaks of interests are labelled as peak X (X = 1, 2, 3, 4, 5 or 6).

Firstly **Peak 1** is seen at -0.41 V corresponding to the one electron reduction of oxygen to superoxide (recall **Reaction 5.4**)

$$O_2 + e^- \rightleftharpoons O_2^{\cdot-} \; ; \; E^o = -0.284 \text{ V} \qquad (\mathbf{5.4})^{28}$$

Secondly, the reductive **Peak 2** occurs at a potential of -0.59 V and corresponds to further single electron reduction of superoxide to peroxide (recall **Reaction 5.6**)

$$O_2^{\cdot-} + H_2O + e^- \rightleftharpoons HO_2^- + OH^-;\ E^o = 0.2\ V\ (pH > 11.6) \quad (\mathbf{5.6})^{28}$$

On the oxidative scan, silver oxidation is seen which consists of two processes. Initially, a "monolayer film" of AgCl (**Reaction 5.3**) is formed at **Peak 3** (-0.036 V vs Ag/AgCl) . Next, a much larger oxidative feature **Peak 4** is seen as a result of the formation and partial dissolution of bulk AgCl[38] at 0.083 V in **Figure 5.2**. The reversed sweep direction at **Peak 4** aimed to avoid any irreversible dissolution damage to the silver electrode surface and the choice of the potential window will be gradually optimized in the following sections in this chapter. Corresponding cathodic, reduction features were seen in the scan following the reversal of the sweep direction leading to stripping **Peak 6 and 5** which were observed at -0.095 V and +0.032 V respectively. The monolayer is formed below the thermodynamic potential for the bulk process as expected for an underpotential deposition.[39, 40]

The formation of both forms of AgCl can be further associated with dissolution at high chloride levels.

$$AgCl\ +\ +\ (n\text{-}1)\ Cl^- \rightleftharpoons AgCl_n^{-(n-1)} \quad (\mathbf{5.7})^{38}$$

where n = 2, 3, 4 [41]

In the following the silver chloride formation peaks in oceanic chloride concentration in more detail is addressed prior to the exploration of their response to variable chloride concentrations in pure sodium chloride solution and synthetic seawater. Then the oxygen reduction peaks' stability in synthetic seawater within the common ocean range of chlorinity was focused on. Finally, the overall method was assessed with three natural seawater samples.

5.3.1 Scan Rate Study of AgCl Formation and Stripping Peaks

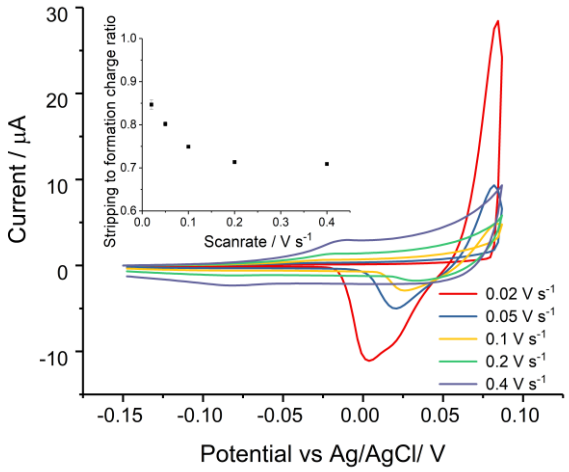


Figure 5.3 AgCl formation and stripping peak at 0.02 Vs^{-1}, 0.05 Vs^{-1}, 0.1 Vs^{-1}, 0.2 $Vs^{-1}$and 0.4 Vs^{-1} in N_2 saturated 0.564 M NaCl solution at a Silver macro-disc electrode r =1.13 mm at 298 K. The inlay shows the ratio of the charges in the stripping to deposition peaks as a function of scan rate.

The scan rate dependency of silver chloride peaks on a silver macro-disc electrode was studied at the oceanic chloride concentration (0.564 M NaCl) over the range 0.02 Vs^{-1} to 0.4 Vs^{-1} (**Figure 5.3**). Each scan consisted of an initial 1min electrochemical cleaning at -1.0 V with cyclic voltammetry swept from -0.15 V and reversed at +0.087 V. The monolayer was formed at -0.013 V and reduced at -0.084 V with peak current proportional (**Figure B.2, Appendix B**) to the scan rate but as expected for the formation of a complete monolayer it did not reflect the bulk chloride concentration of chloride in the range studied[40, 42], although in low halide concentration such pre peak has been used successfully in iodide detection by Malongo *et al.*[33]. Previous work showed the so-called 'monolayer' is in fact formed of silver chloride clusters distributed on the electrode surface rather than a continuous monolayer of AgCl. Prior to the formation of the bulk AgCl the clusters expand and merge with each other.[43, 44] The charge passed in the 'monolayer' was found to be 1.2±0.1 µC cm^{-2} (**Appendix B**) consistent with the literature.[42] The charge passed in the first peak is tiny compared with that of the overall AgCl

formation in peak at +0.084 V (637.7±82.3 μC cm^{-2} at 0.02 V s^{-1}), so does not affect the analysis of the second peak nor does it provide information on solution chloride levels.

The large, bulk AgCl formation feature was observed at higher overpotential. **Figure 5.3** shows that at high scan rates the peak is not seen; rather a signal largely of pseudo capacity, a signal is observed in the range 0.2 Vs^{-1} to 0.4 Vs^{-1} with the current scaling in direct proportion to the scan rate. However, at progressively lower scan rates from 0.1 Vs^{-1} to 0.02 Vs^{-1}, an anodic nucleation loop started to develop at ca +0.084 V on the forward scan associated with an increased signal in the stripping peak on the subsequent cathodic scan. These observations are consistent with those of Pargar *et al*.[45] and confirm that a thicker silver chloride film was built with prolonged reaction time. Mele *et al*[38] developed a detailed mechanism based on progressive nucleation and diffusion-controlled growth in which higher chloride levels promote AgCl formation as well as its subsequent partial dissolution suggesting potential analytical use for chloride determination.[9, 43, 45]

Cathodic stripping signals were observed with decreasing peak potentials from 0.026 V at 0.1 Vs^{-1} to 0.0040 at 0.02 Vs^{-1} and shoulder appeared in the latter case at ca. 0.02 V which is in agreement with literatures.[40, 45] **Figure 5.3** (inlay) shows a plot of the ratio of the charge passed in the silver chloride reduction to that calculated by integrating the oxidation current over the range -0.15 V to 0.087 V (forward sweep) and 0.087 V to 0.055 V (reverse sweep) as a function of the scan rate from 0.02 Vs^{-1} to 0.4 Vs^{-1}. At low scan rates most of the deposited silver chloride is stripped (ratio approaches unity). The apparent inefficiency of stripping at high scan rates reflects the large capacitance response under these conditions. The slower scan rate ie. 0.02 Vs^{-1} was selected for the following determinations of chloride level focusing on the bulk AgCl deposition/stripping.

5.3.2 Chloride Determination in NaCl Solutions

Given the complexity of seawater (**Table 5.1**) initial studies aimed at the determination of chloride in seawater focussed first on aqueous NaCl solutions containing concentrations similar to those found in open oceans. The latter range spans the salinity range from 32 g kg^{-1} to 37 g kg^{-1} [46]. This corresponds to a chloride concentration range of 0.500 M to 0.578 M (**Table 5.2**). The following experiments were conducted to determine whether it is possible to distinguish chloride concentrations with silver chloride voltammetric responses.

Table 5.2 Oceanic chloride concentrations as inferred from salinity values via **Reaction 5.2**

Salinity / g kg^{-1}	**32**	**33**	**34**	**35**	**37**
NaCl / M	0.500	0.515	0.531	0.546	0.578

Silver chloride deposition and stripping were performed at 0.02 V s^{-1} in 0.500 M to 0.578 M air-saturated sodium chloride solutions. **Figure 5.4** shows the study of the deposition/stripping by means of a potential scan from -0.2 V to +0.093 V followed by sweep reversal to -0.2 V. The electrode was held 1min at -0.2 V to remove the remaining silver chloride.

Initially, an experiment was performed to determine silver chloride peak parameters as a function of chloride content without oxygen reduction. **Figure 5.4** depicts two large peaks one measured at ca. +0.050 V for nucleation and another at ca. 0.00 V for cathodic reduction. The broad reduction peak consists of two adjacent peaks at 0.00 V and 0.020 V. The shoulder in the stripping peak has been discussed by Pargar *et al.*[45] and Birss *et al.*[40], the appearance of a peak at 0.020 V may reflect instantaneous nucleation or silver dissolution, but the cause remains open to debate due to the mechanistic complexity of silver chloride formation. Nevertheless, both nucleation and stripping peak heights increased with increased sodium

chloride concentrations. As presented in the inset of **Figure 5.4**, the bulk AgCl nucleation peak current is linearly dependent on the chloride concentration from 0.500 M to 0.578 M although the calibration curve does not pass through the origin indicating a threshold concentration is required for the nucleation process.

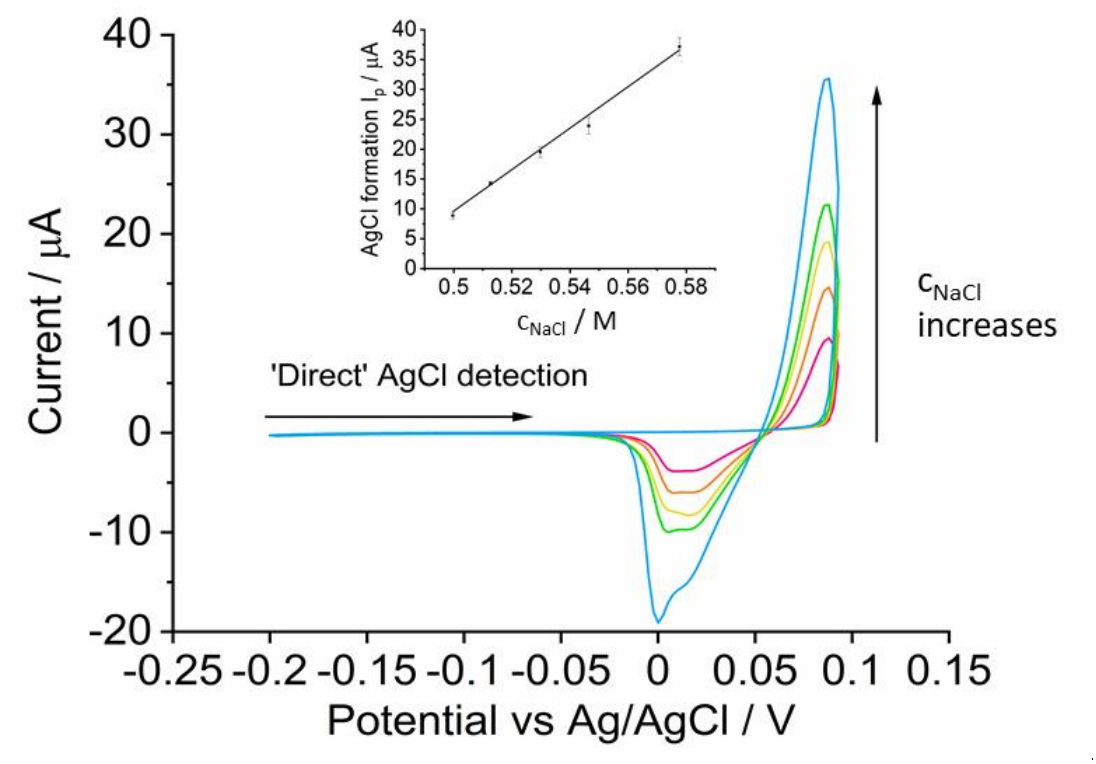
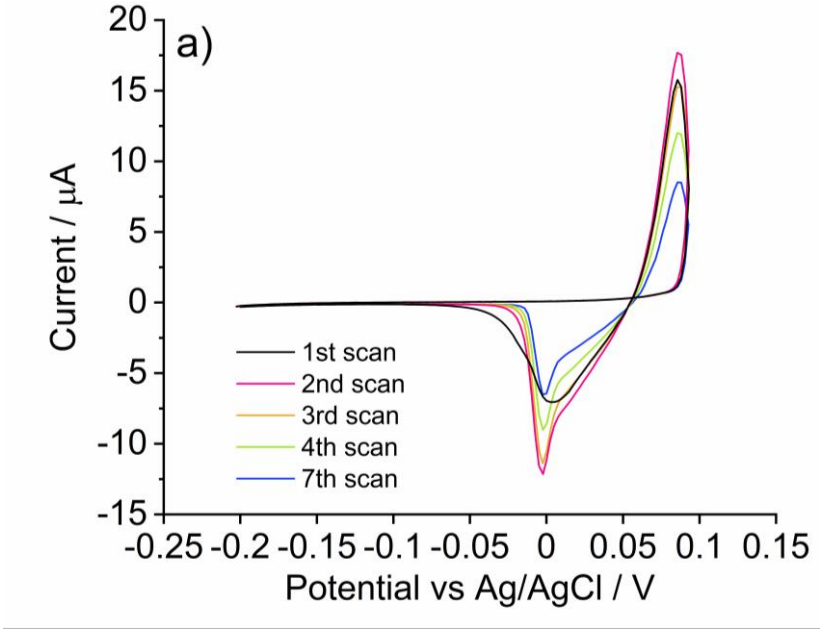


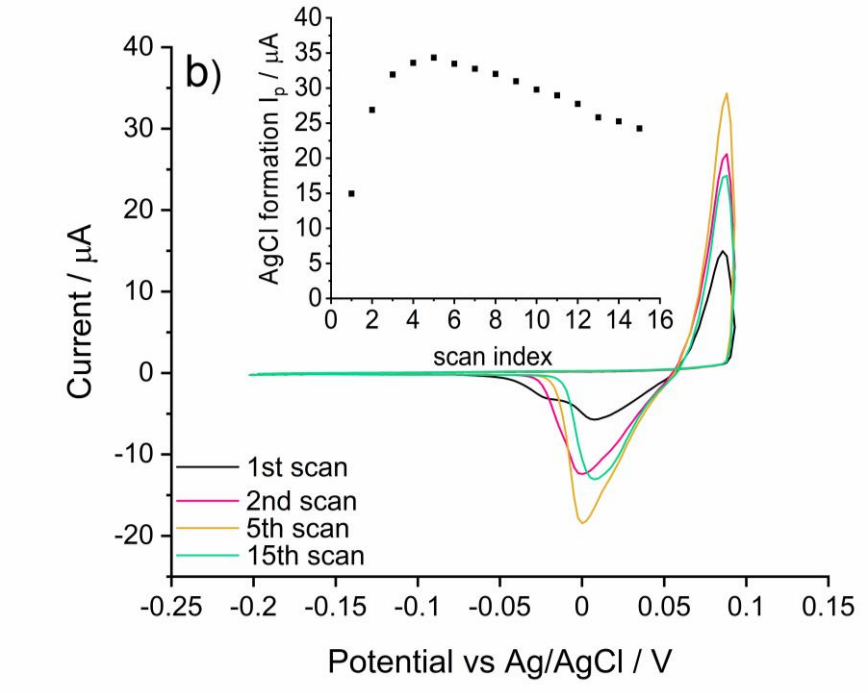
Figure 5.4 The chloride concentration determination conducted voltammetrically at 0.02 V s^{-1} in air saturated NaCl solutions (0.500 M to 0.578 M) measured at a silver macro-disc electrode. Voltammograms for silver chloride formation started from -0.20 V and reversed at +0.093 V. Red: 0.500 M NaCl; orange: 0.515 M NaCl; yellow: 0.531 M NaCl; green: 0.546 M NaCl and blue: 0.578 M NaCl. Inlay: the calibration curve of the silver chloride nucleation peak height against chloride concentration with a regression coefficient R^2 of 0.989, each data point is the average of a minimum of 3 repeats.

The overall charge was evaluated for the deposition/stripping process. For the silver chloride nucleation, the integrated range embraced all potentials where oxidative currents flowed; from -0.20 V to + 0.093 V on the forward scan and, in the reverse, from + 0.093 V to the potential where the oxidative current became zero. In silver chloride reduction, the current was

integrated from the potential corresponding to the onset of reductive currents to -0.20 V. The integration showed that more than 90% silver chloride formed was removed at each experiment, but the remaining silver chloride can deactivate the surface and prevent reproducible measurements from scan to scan (**Figure 5.5 a**). To allow multiple measurements without the need for mechanical cleaning in between, electrochemical cleaning was attempted at -0.20 V for 1min after each scan. However, this unavoidably increased surface roughness, which was indicated in **Figure 5.5 b**. The significantly increased peak current at **Peak 4** and **5** suggested the apparent increase in electrochemically defined electrode surface area. Consequently, prolonged polishing afterwards is required for only a slight improvement (**Figure 5.5 b**). Thus the investigation of a more "gentle" method that removes silver chloride residue and 'activates' the silver surface before the deposition was desired and the attention was turned to the possible use of the oxygen reduction reaction for this purpose whilst noting that an additional advantage of scanning the ORR prior to making analytical measurements using the AgCl features is that it might provide an 'internal reference' potential which would allow the use of a quasi-reference electrode in the analytical measurement by virtue of giving a voltammetric peak(s) against which excursions of a well-defined potential range into the AgCl formation region could be made. This has the advantage that the quasi-reference electrode, could be chosen to avoid a liquid junction potential near a conventional reference electrode due to leakage of its electrolyte and / or ingress of seawater and thus a possible shift in the overall voltammogram in addition to any changes resulting from residual AgCl peaks from previous measurements. To avoid such uncertainty, a stable internal reference potential is desirable and the ORR was explored in these contexts with the further possible advantage that dissolved oxygen is invariably present in seawater samples and so the approach would both exploit this whilst simultaneously avoiding the need for outgassing as is commonly undertaken in voltammetry.

The peak currents associated with the ORR were also explored to see if they could additionally provide a measure of the dissolved oxygen concentration.





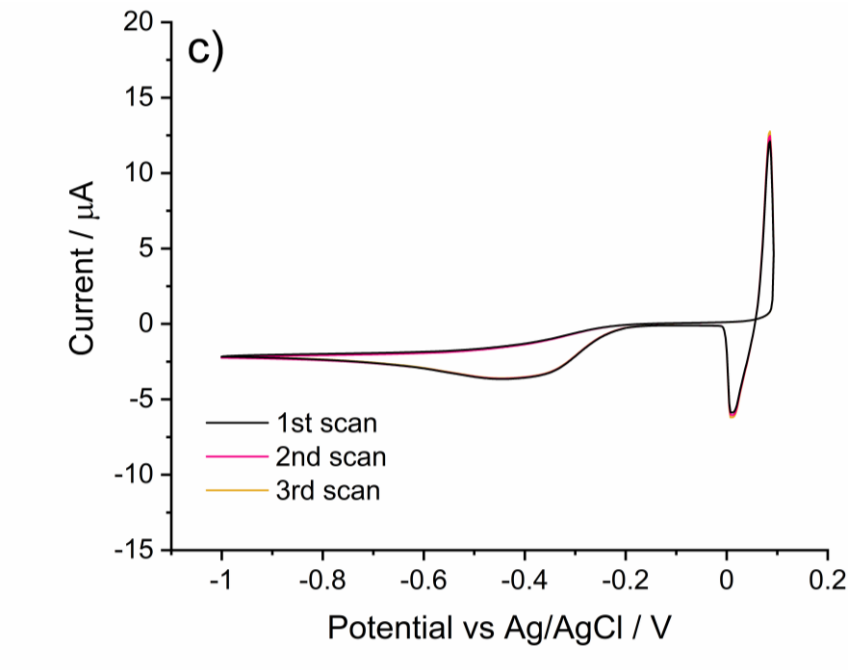


Figure 5.5 Silver chloride deposition reproducibility at 0.02 Vs^{-1} at 293 K in 0.546 M NaCl air saturated solution. a) Seven successive scans each started from -0.20 V to +0.093 V and reversed. b) Fifteen successive scans each started from -0.20 V to +0.093 V and reversed followed by electrochemical cleaning at -0.2 V for 1min, inset shows silver chloride formation peak current as a function of the scan index. c) Three successive scans each started from oxygen reduction at -0.20 V to -1.0 V and reversed at +0.093 V for silver chloride formation.

Accordingly, the oxygen reduction reaction was explored, noting that the oxygen reduction reaction has been studied in chloride rich media and shown to involve two voltammetric features with a first electron transfer at -0.40 V forming superoxide and a second at -0.60 V forming peroxide.[34] The surface activation with ORR was studied voltammetrically in air-saturated 0.546 M NaCl at 0.02 Vs^{-1} (**Figure 5.5**) with three sets of successive experiments. Each scan was conducted with air-saturated solution *without* mechanical polishing of the electrode in between. First, a control experiment involving simply the 'direct' formation of AgCl was made in which the voltammetric scan started from -0.20 V and swept towards +0.093 V at which point it was reversed and a total of seven successive such scans made. Second, the step potential cleaning method was attempted, starting from a cyclic voltammetry between -0.20 V and +0.093 V followed by 1min holding at -0.20 V and a total of fifteen successive such scans made (**Figure 5.5 b**). Third a wider potential window was scanned to

embrace the ORR. These sweeps started from -0.20 V, swept negative to -1.0 V, then reversed to +0.093 V at which potential the scan again reversed terminating at -0.20 V before repeating thrice (**Figure 5.5 c**). The 'direct' reaction shows large peaks for silver chloride formation (0.088 V) and reduction (ca. 0.00 V). Both increased in the second scan but decreased significantly from 15.5 µA to 8.4 µA afterwards due to the loss of active silver sites. The primary electrochemical cleaning at -0.20 V for 1 min follows a similar trend with the control experiment but the initial increase in silver chloride peak height was extended from 15 µA to 34 µA (5^{th} scan) followed by a slower decay to 24 µA in 15^{th} scan. In contrast, in the third type of experiment, when oxygen reduction was first conducted prior to the AgCl formation, a remarkable reproducibility was found in both the single broad ORR feature at ca. -0.40 V and two sharp silver chloride peaks as shown in **Figure 5.4** which is similar to that seen in concentrated KCl solution albeit with the superoxide and peroxide signals more merged. The application of combined ORR and AgCl reactions are discussed afterwards.

To investigate practical benefits of scanning through the ORR voltammetric features prior to the AgCl formation/stripping analysis, the voltammetry shown in **Figure 5.6** were performed and compared to 'direct' AgCl formation/stripping in **Figure 5.4** Each voltammogram was conducted at 0.02 V s^{-1}, and consisted of initial oxygen reductions induced by scanning from -0.20 V to -0.75 V followed by a reverse sweep up to the silver chloride reactions at + 0.093 V and terminated at -0.20 V. The inset of **Figure 5.6** shows single broad ORR peak at ca. -0.40 V instead of two adjacent peaks in **Figure 5.2** at -0.40 V and -0.60 V. This is due to shifting in peroxide peak potential from -0.60 V at 0.1 V s^{-1} to a lower overpotential of ca.- 0.45 V at 0.02 V s^{-1}. A previous study of ORR in pure 0.54 M KCl solution showed a similar shift in peroxide peak potential from -0.6 V at 0.4 Vs^{-1} to -0.5 V at 0.02 Vs^{-1} on the polycrystalline silver electrode in contrast to the relatively constant peak potential for

superoxide formation[34], possibly due to the increased superoxide concentration. Regardless of the changes in peroxide formation, the stability of the superoxide feature implies the advantage of introducing ORR in oceanic chlorinity detections as an internal reference potential.

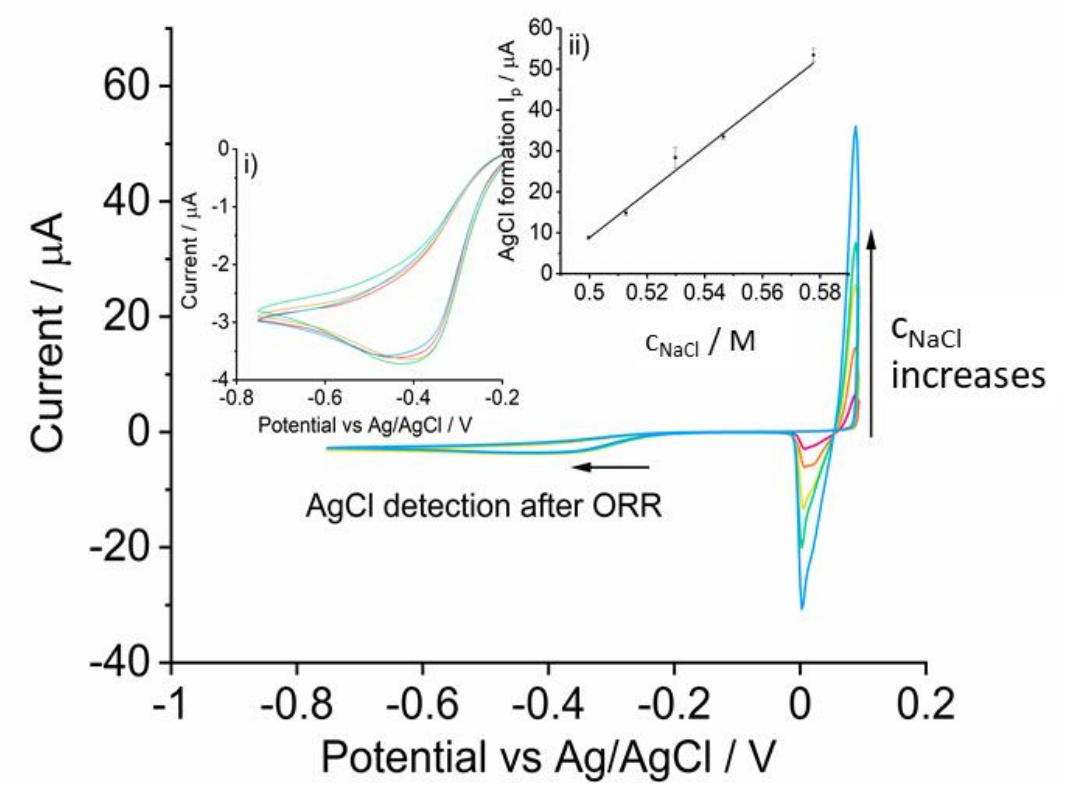


Figure 5.6 The chloride concentration determination conducted voltammetrically at 0.02 V s^{-1} in air saturated NaCl solutions (0.500 M to 0. 578 M) measured at a silver macro-disc electrode. Voltammograms of the first oxygen reduction scanned from -0.20 V to -0.75 V followed by silver chloride reactions reversed at +0.093V; Red: 0.500 M NaCl; orange: 0.515 M NaCl; yellow: 0.531 M NaCl; green: 0.546 M NaCl and blue: 0.578 M NaCl. Inlay i) expanded ORR features; ii) the calibration curve of the silver chloride nucleation peak height against chloride concentration with a regression coefficient R^2 of 0.996, each data point is the average of a minimum of 3 repeats.

Meanwhile, **Figure 5.6** shows silver chloride features after oxygen reduction. From -0.20 V to +0.093 V. Only bulk silver chloride peaks were observed at potentials identical to 'direct' deposition / stripping measurements in **Figure 5.6**, but the nucleation peak is much higher in current than seen in the 'direct' measured signals at the same chloride level. **Figure 5.6** inlay ii) shows a linear calibration curve of silver chloride nucleation peak current against the chloride concentration from 0.500 M to 0.578 M. Particularly, the overall 'sensitivity' was

improved from 10 μA to ca.35 μA in **Figure 5.4** to 10 μA to ca.55 μA in **Figure 5.6**. The significantly enhanced sensitivity to chloride concentrations shows the second advantage of introducing ORR for the silver surface activation.

In summary, the methodology for chloride measurement in pure solution can be improved by first voltammetrically scanning the oxygen reduction reactions before making the silver chloride deposition /stripping measurements at 0.02 V s^{-1} and has been validated in pure sodium chloride solutions within the oceanic chlorinity range using the bulk deposition peak current to determine chloride concentrations. The method was subsequently applied the method in synthetic seawater

5.3.3 Chloride Level Determination in Synthetic Seawater

In the previous section an approach for the accurate electrochemical determination of high chloride concentrations in excess of 0.500 M was established. The next objective is to apply this method to synthetic seawater with a composition within the oceanic salinity range. In order to obtain accurate correlations, synthetic seawater of eight levels of chloride concentrations were studied. The detection range was also extended to salinity values from 31 g kg^{-1} to 38 g kg^{-1} in addition to the usually encountered range of 32 g kg^{-1} to 37 g kg^{-1}. The total chloride concentrations studied thus ranged from 0.484 M to 0. 593 M and were made using varying amounts of sodium chloride to the otherwise standard recipe (**Table B.1 Appendix B**).[36, 37]

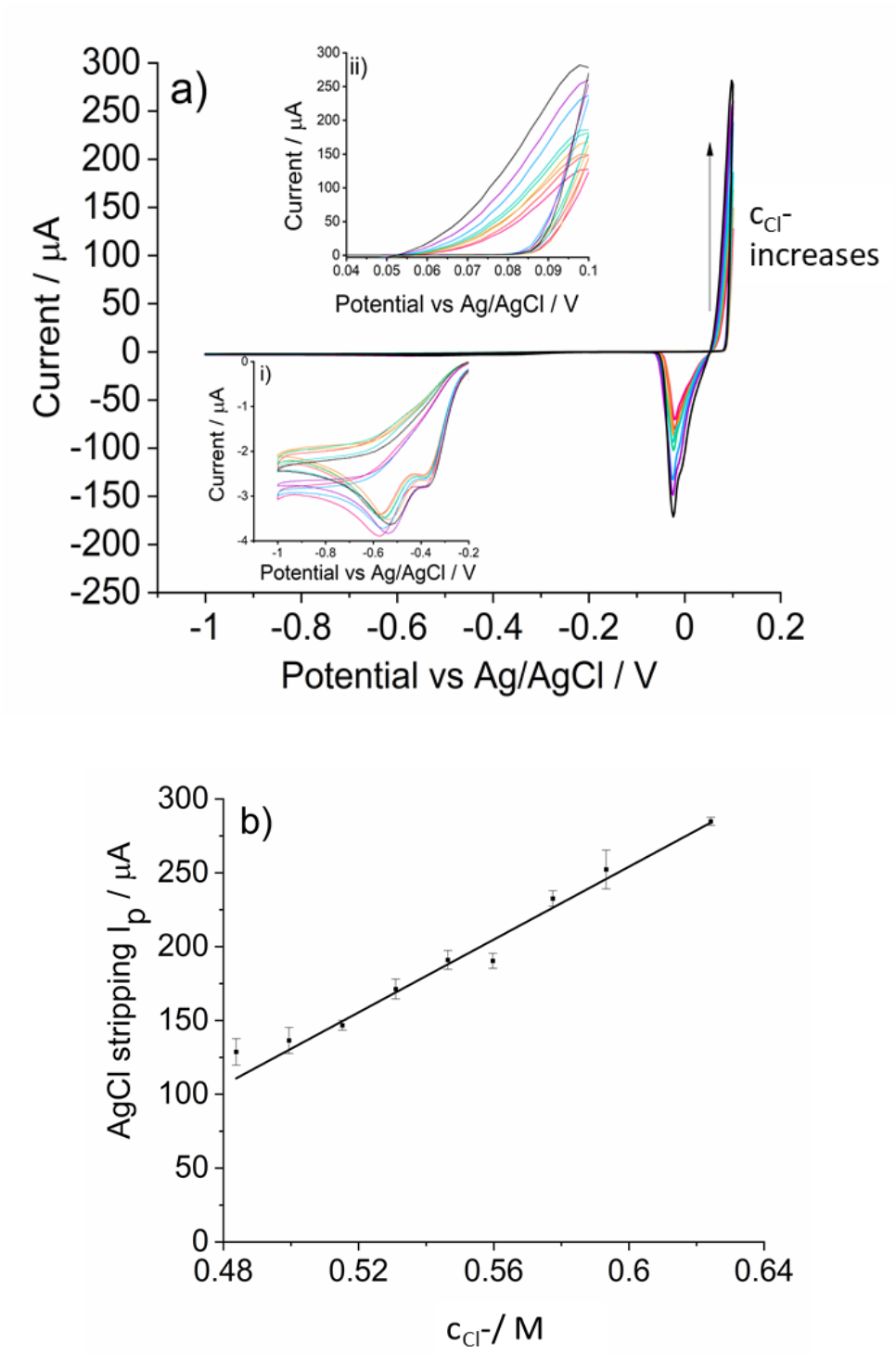


Figure 5.7 The chloride concentration determination conducted at 0.02 Vs^{-1} in air saturated synthetic seawater (0.484 M to 0.624 M) measured at a silver macro-disc electrode. a) Voltammograms consist of first oxygen reduction from -0.20 V to -1.0 V followed by silver chloride reactions reversed at +0.1 V; inlay i) expanded ORR features; ii) expanded silver chloride nucleation peaks; b) the calibration curve of the silver chloride nucleation peak height against chloride concentrations with a regression coefficient R^2 of 0.989, each data point consists of 4 repeats.

The electroanalytical responses of silver chloride at 0.02 Vs^{-1} were explored in air-saturated synthetic seawater. The potential range was extended into -1.0 V to + 0.1 V. **Figure 5.7** shows the voltammogram which consists of oxygen reduction and silver chloride deposition / reduction, scanned first from -0.20 V to -1.0 V then scanned positively to +0.1 V and returned to -0.20 V.

First the ORR features were analysed as providing a possible internal reference potential. **Figure 5.7 a** inset i) shows two clearly separated diffusional peaks during two single-electron transfer reactions of oxygen at ca. -0.40 V and -0.60 V. The first peak refers to the formation of superoxide the potential of which was used as an internal reference. The second peak relates to further reaction to produce peroxide. According to the summarised data in **Appendix B**, **Figure B.3**, the superoxide peak potential and current are almost constant at -0.39±0.01 V and 2.51±0.08 μA over the chloride concentration (0.484 M to 0.624 M). Closely similar superoxide redox potentials were reported in other media by Baxendale *et al.*[47] (-0.395 V *vs.* Ag/AgCl) and Koppenol *et al.*[48] (-0.385±0.02 V *vs.* Ag/AgCl). The constant value of superoxide peak potential confirms the viability of using the superoxide peak as an internal reagent free reference potential in air-saturated seawater. Meanwhile, the constant superoxide peak current is consistent with the findings of Debelius *et al.*[49] who determined oxygen solubility in brine with salinity of 30.77 g kg^{-1} (212.7 μM) and 37.77 g kg^{-1} (203.2 μM) experimentally. The overall difference in current is as little as 4% detected voltammetrically.

Next, silver chloride formation / reduction features were analysed. Both peaks increased clearly along with the chloride increase (**Figure 5.7 a**), similar to the trend observed in pure sodium chloride measurements. The peak height of the AgCl formation varied linearly with chloride concentration from 0.484 M to 0.624 M. The calibration curve is plotted in **Figure 5.7 b**. The methodology with extended potential range of -1.0 V to +0.1 V shows increased sensitivity of

chloride detection from 0.36 mA M^{-1} in **Figure 5.6** to 1.13 mA M^{-1} in **Figure 5.7** even in the presence of other sea salts.

Meanwhile, Toh *et al.*[50] quantified chloride ions in synthetic sweat using silver nanoparticle-modified electrodes. Thus attempts were made to similar use silver nanoparticles to detect chloride ions in synthetic seawater. 1.0 nmole equivalent of silver in the form of washed AgNPs (diameter of 100 nm) was drop casted on a glassy carbon electrode. Cyclic voltammograms were swept at 0.02 V s^{-1} from -0.40 V to +0.90 V and reversed in three different nitrogen saturated solutions; first 0.1 M KNO_3 solution in the control experiment then two synthetic seawater solutions with 0.484 M Cl^- and 0.593 M Cl^- (**Figure B.4 in Appendix B**).

In 0.1 M KNO_3, a broad peak at +0.50 V was observed corresponding to the oxidation of metallic silver. In synthetic seawater solutions, two peaks were observed at ca. +0.11 V and -0.040 V corresponding to silver chloride formation and stripping. By increasing media chloride concentration from 0.484 M to 0.593 M, the silver chloride formation peak was shifted from +0.11 V to +0.10 V with a slight peak current decrease. Similarly, the broad stripping peak was shifted from -0.040 V to -0.033 V. Despite a decreased overpotential with increased chloride concentration seen for both oxidation and reduction features, for the whole detection range the peak potential shifted as little as 0.010 V. This is consistent with the expectation based on the Nernst equation - the range of chloride ions encountered in seawater is too small to be accessed via a peak potential measurement and so quantification of chloride ions using AgNPs was not successful and further experiments focussed on the method developed above using a silver electrode.

5.3.4 Chloride Level Determination in Natural Seawater

To examine the feasibility of real seawater chloride determination, batches of Scottish, Plymouth and Bermuda seawater were tested using the newly developed method. The chloride concentrations of the authentic samples were tested with the well established argentometric method.[22] First 0.0141 M silver nitrate was standardised with sodium chloride solution of the same concentration. Next, 1.0 mL of natural seawater was diluted into 100.0 mL then 1.0 mL of 0.25 M potassium chromate solution was added. Silver nitrate was slowly dropped into the seawater sample until the pinkish-yellow end-point was realized. With three repeats, estimations of the chloride concentration by titration in the Scottish, Plymouth and Bermuda seawater samples were found to be 0.563±0.001 M, 0.582±0.001 M and 0.619±0.001 M respectively.

Next, a cyclic voltammogram was conducted in air saturated natural seawater starting from -0.20 V to -1.0 V with reversal to 0.10 V before finally being returned to -0.20 V at the end of the scan. The experiment was repeated three times. **Figure 5.8** shows the recorded voltammograms for three natural seawater samples. The voltammetric peaks of both oxygen reductions and silver chloride deposition and stripping signals are consistent with each other based on their identical dissolved oxygen concentrations and higher chloride concentration in Plymouth and the extreme salty Bermuda deep seawater. The latter either reflects the depth of sampling or evaporation during transport of the sample. For the ORR features, two large peaks were as expected and discussed above, observed for each sample at -0.39 V and ca. -0.55 V. The peak potential for superoxide formation matches the experimental results in pure sodium chloride and synthetic seawater so that the peak can be used as an internal reference. Meanwhile the concentration of chloride in natural seawaters were calculated via the calibration curve shown in **inset ii)** using the silver chloride formation peak current. For both seawater samples,

with 204±3 µA (Scotland), 228±2 µA (Plymouth) and 280±2 µA (Bermuda) in peak height, the expected chloride concentration is 0.561±0.003 M (Scotland), 0.581±0.002 M (Plymouth) and 0.624±0.003 M (Bermuda) in excellent agreement with the titration result (black, red and blue scatters of **inlay ii)**). In this way the developed method was validated in authentic seawater.

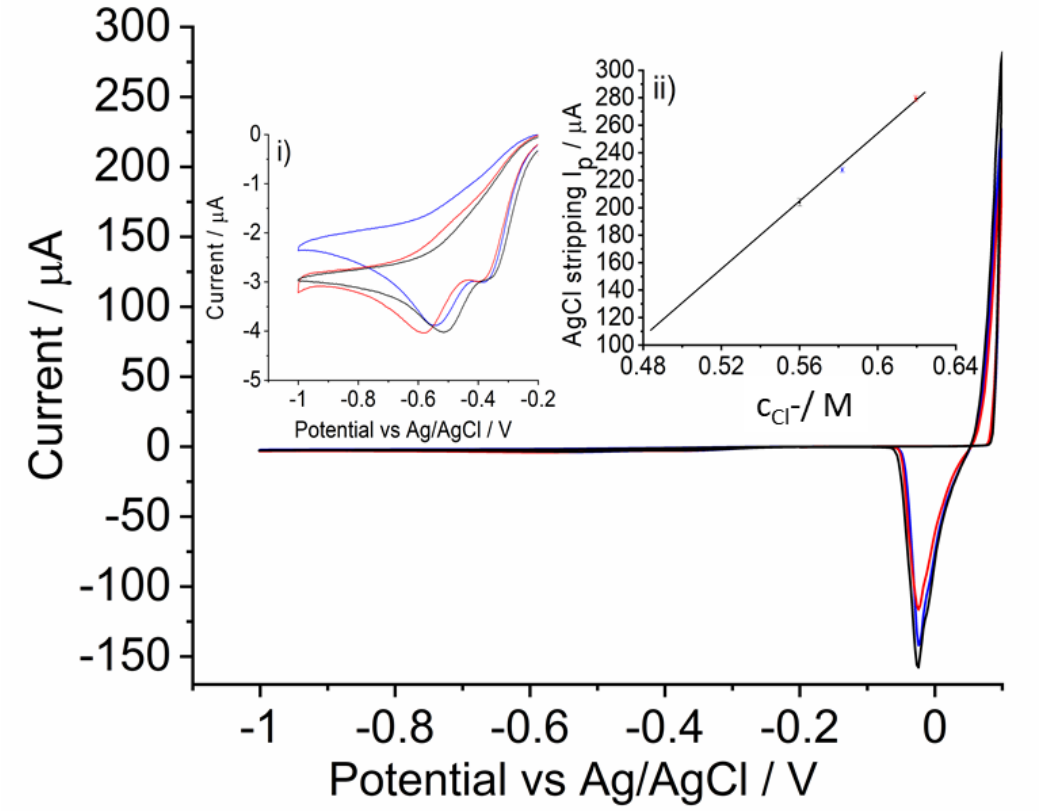


Figure 5.8. The chloride concentration determination conducted at 0.02 V s^{-1} in air saturated authentic seawater samples measured at a silver macro-disc electrode. Black: natural seawater from Scotland, c_{Cl^-} = 0.563 M , blue: natural seawater from Plymouth, c_{Cl^-} = 0.562 M; Red: natural seawater from Bermuda. Inlay i) expanded ORR feature, ii) black line: the calibration plot of peak height of nucleation peak against the concentration of chloride from synthetic seawater data; black scatter: Scottish seawater sample; blue scatter: Plymouth seawater sample; red scatter: Bermuda seawater sample, each data point consists of three repeats.

5.4 Conclusions

This chapter presents a simple and facile chloride detection system for the use in media of high chloride concentration and was specifically developed for the use in seawater in which chloride is the major component and presents over a narrow range of high concentrations of ca. 0.5 M which challenges potentiometric methods. The method uses the currents flowing during the nucleation / growth of AgCl on a bulk silver electrode over a well-defined potential range as a measure of the chloride concentration. In order to realise reproducibly clean electrodes and to facilitate the use of quasi-reference electrodes a prior sweep is used to clean the electrode and permit reproducible measurements even without mechanical cleaning. The method was developed using authentic samples of seawater from Scotland, Plymouth and Bermuda respectively with validation against an independent method.

Bibliography

1. Y. Guo and R. G. Compton, *Talanta*, 2021, **232**.
2. M. E. Q. Pilson, *An Introduction to the Chemistry of the Sea*, Cambridge University Press, Cambridge, 2 edn., 2012.
3. E. L. Lewis, *IEEE J. Oceanic. Eng.*, 1982, **5**, 350-357.
4. G. S. E. Lagerloef, C. T. Swift and D. M. L. Vine, *Oceanography (Wash D C)*, 1995, **8**, 44-50.
5. M. Yamamoto, *Chemosphere*, 1996, **32**, 1217-1224.
6. A. Gupta, M. Maynes and S. Silver, *Appl. Environ. Microbiol.*, 1998, **64**, 5042-5045.
7. C. Batchelor-McAuley, K. Tschulik, C. C. M. Neumann, E. Laborda and R. G. Compton, *Int. J. Electrochem. Sci.*, 2014, **9**, 1132-1138.
8. K. W. Bruland and M. C. Lohan, in *Treatise on Geochemistry*, eds. H. D. Holland and K. K. Turekian, Pergamon, Oxford, 2003, pp. 23-47.
9. C. Levard, S. Mitra, T. Yang, A. D. Jew, A. R. Badireddy, G. V. Lowry and G. E. Brown, *Environ. Sci. Technol*, 2013, **47**, 5738-5745.
10. F. M. M. Morel, A. M. L. Kraepiel and M. Amyot, *Annu. Rev. Ecol. Evol. Syst*, 1998, **29**, 543-566.
11. U. Angst, B. Elsener, C. K. Larsen and Ø. Vennesland, *Cement and Concrete Research*, 2009, **39**, 1122-1138.
12. J. Alcántara, D. d. l. Fuente, B. Chico, J. Simancas, I. Díaz and M. Morcillo, *Materials*, 2017, **10**, 406.
13. K. Y. Ann and H.-W. Song, *Corros. Sci.*, 2007, **49**, 4113-4133.
14. V. Marcos-Meson, A. Michel, A. Solgaard, G. Fischer, C. Edvardsen and T. L. Skovhus, *Cem. Concr. Res.*, 2018, **103**, 1-20.

15. F. J. Millero, R. Feistel, D. G. Wright and T. J. McDougall, *Deep Sea Research Part I: Oceanographic Research Papers*, 2008, **55**, 50-72.
16. W. J. Wallace, *The development of the chlorinity/salinity concept in oceanography*, Elsevier Scientific Pub. Co, Amsterdam, New York, 1974.
17. J. Lyman, *Limnol. Oceanogr.*, 1969, **14**, 928-929.
18. R. H. Stewart, *Introduction to physical oceanography*, University Press of Florida, United States, 2009.
19. K. Grasshoff and A. Wenck, *ICES Journal of Marine Science*, 1972, **34**, 522-528.
20. T.-K. Hong, M.-H. Kim and M.-Z. Czae, *Int. J. Anal. Chem.*, 2010, **2010**, 602939.
21. W. S. Reeburgh and J. H. Carpenter, *Limnol. Oceanogr.*, 1964, **9**, 589-591.
22. L. S. Clesceri, A. E. Greenberg and A. D. Eaton, *Standard Methods for the Examination of Water and Wastewate*, APHA American Public Health Association, USA, 20th edn., 1998.
23. H. H. Willard, J. Merritt, L L, J. A. Dean and J. Settle, F A, *Instrumental methods of analysis, 7th edition*, Florence, KY (US); Wadsworth Publishing Company, 1988.
24. UNESCO, *UNESCO Technical Papers in Marine Science*, 1981, **36**, 24.
25. E. L. Lewis and R. G. Perkin, *Deep Sea Res. Part A Oceanogr. Res. Pap.*, 1981, **28**, 307-328.
26. D. G. Wright, R. Pawlowicz, T. J. McDougall, R. Feistel and G. M. Marion, *Ocean Sci.*, 2011, **7**, 1-26.
27. E. Lewis, *IEEE J. Oceanic. Eng.*, 1980, **5**, 3-8.
28. A. J. Bard, R. Parsons, J. Jordan, P. International Union of and C. Applied, *Standard potentials in aqueous solution*, M. Dekker, New York, 1985.
29. B. B. Blizanac, P. N. Ross and N. M. Markovic, *Electrochimica Acta*, 2007, **52**, 2264-2271.
30. K. Arai, F. Kusu, N. Noguchi, K. Takamura and H. Osawa, *Anal. Biochem.*, 1996, **240**, 109-113.
31. X. Qin, H. Wang, Z. Miao, X. Wang, Y. Fang, Q. Chen and X. Shao, *Talanta*, 2011, **84**, 673-678.
32. J. Bujes-Garrido, D. Izquierdo-Bote, A. Heras, A. Colina and M. J. Arcos-Martínez, *Anal. Chim. Acta*, 2018, **1012**, 42-48.
33. T. K. Malongo, S. Patris, P. Macours, F. Cotton, J. Nsangu and J.-M. Kauffmann, *Talanta*, 2008, **76**, 540-547.
34. Y. J. Guo, M. J. Yang, R. C. Xie and R. G. Compton, *Chem. Sci.*, 2021, **12**, 397-406.
35. L. Jiang, B. R. Carter, R. A. Feely, S. K. Lauvset and A. Olsen, *Scientific Reports*, 2019, **9**, 18624.
36. F. M. M. Morel, J. G. Rueter, D. M. Anderson and R. R. L. Guillard, *J. Phycol.*, 1979, **15**, 135-141.
37. N. M. Price, G. I. Harrison, J. G. Hering, R. J. Hudson, P. M. V. Nirel, B. Palenik and F. M. M. Morel, *Biological Oceanography*, 1989, **6**, 443-461.
38. M. F. L. de Mele, R. C. Salvarezza, V. D. Vasquez Moll, H. A. Videla and A. J. Arvia, *J. Electrochem. Soc.* , 1986, **133**, 746-752.
39. H. Ha and J. Payer, *Electrochimica acta*, 2011, **56**, 2781-2791.
40. V. I. Birss and C. K. Smith, *Electrochim. Acta.*, 1987, **32**, 259-268.
41. R. D. Giles, *J. Electroanal. Chem. Interf. Electrochem.*, 1970, **27**, 11-19.
42. S. Jaya, T. P. Rao and G. P. Rao, *J. Appl. Electrochem.*, 1987, **17**, 635-640.
43. X. Jin, J. Lu, P. Liu and H. Tong, *J. Electroanal. Chem.*, 2003, **542**, 85-96.
44. H. Ha and J. Payer, *Electrochim Acta*, 2011, **56**, 2781-2791.
45. F. Pargar, H. Kolev, D. A. Koleva and K. van Breugel, *J. Mater. Sci.*, 2018, **53**, 7527-7550.
46. C. Elachi, and J. v. Zyl, *Introduction to the Physics and Techniques of Remote Sensing*, John Wiley & Sons, Inc., Canada, 2 edn., 2006.
47. J. H. Baxendale, M. D. Ward and P. Wardman, *J. Chem. Soc. Faraday Trans.*, 1971, **67**, 2532-2537.
48. W. H. Koppenol, D. M. Stanbury and P. L. Bounds, *Free Radic. Biol. Med.* , 2010, **49**, 317-322.
49. B. Debelius, A. Gómez-Parra and J. M. Forja, *Hydrobiologia*, 2009, **632**, 157-165.

50. H. S. Toh, C. Batchelor-McAuley, K. Tschulik and R. G. Compton, *Analyst*, 2013, **138**, 4292-4297.

Chapter 6

Metal Deposition and Stripping under Self-supported Conditions: Experiment and Simulation

Chapter 5 reported the detection of chloride in natural seawater with an extreme high ionic conductivity. The opposite extreme arises in the case of drinking water where the system is less than fully supported. As discussed in **Section 1.3.3** and **1.3.4** previously, voltammetric signals under weakly support systems reflect the migration effect and the result of ohmic drop becomes significant. The voltammetry under such conditions is first studied in this chapter with a theoretical model followed by experimental validations before reporting a bespoke chloride sensor for drinking water in **Chapter 7**.

To what extent does the mass-transport to and from an electrochemical interface change when the dimensions of the electrode are comparable to the Debye length of the system? This chapter develops a theoretical model for the deposition and stripping of a metal from an electrode accounting for finite electrolyte concentrations. When the electrode is large compared to the Debye length electroneutrality holds and migration significantly influences the mass-transport of ions in the vicinity of the electrode, altering the electrochemical current. However, simulations predict that when the electrode is comparable to or smaller than the Debye length of the system then the influence of migration is minimised. In the experiment, the steady-state reductive flux for the deposition of silver to a microelectrode is shown to deviate from that expected on the basis of electroneutrality and is compared with simulation whilst the results

also show an altered rate of metal nucleation in the absence of additional supporting electrolyte. The work presented in this chapter has been published as a first author paper in *Journal of Electroanalytical Chemistry*[1] and was carried out in collaboration with Dr. Minjun Yang and Dr. Christopher Batchelor-McAuley. The simulation models were written by Dr. Christopher Batchelor-McAuley.

6.1 Introduction

At the macroscale electroneutrality dictates that for a system at equilibrium the net charge on a material is zero. The general validity of this statement, in essence, reflects the strength of the Coulomb force; significant charge separation on the macroscale is prohibitively energy expensive.[2] In the modelling of electrochemical systems, electroneutrality is an often invoked *a priori* assumption,[3-8] employed to simplify the required analysis. However, at length scales comparable to or below the Debye length this approximation is not valid.

Since the 1980s a trend in the electrochemical field has been towards the study and investigation of electrochemical reactions at the nanoscale.[9, 10] Early attempts at studying reactions at such length scales focused on the production of nanoscopic electrodes. [9, 11] Although insightful, the widespread uptake and use of such methods continues to be comparatively limited. This arguably predominantly reflects the difficulties associated with electrode fabrication and reproducibility. Moreover, such systems face specific problems, such as having to consider the possible occurrence of redox reactions at the glass/electrode interface.[12] As an alternative approach to the same problem, the use and development of the Nanoparticle impact electroanalysis (NIA) technique has expanded significantly over the previous decade.[13-15] NIA measures electrochemical signals at the of a single nanoparticle and has been widely used in nanoparicles characterization and electroanalysis. From a fundamental

perspective, the interest in these nanoscale systems is that as an electrochemical interface becomes smaller the associated diffusion layer (solution phase depletion zone) correspondingly decreases. Consequently, at the nanoscale the depletion zone surrounding the electrochemical interface is expected to be comparable in length to that anticipated for the electric double layer. Hence, one might expect differing electrochemical behaviour when studying processes at the nanoscale.

For all the theoretical work focused on understanding the structure of the double layer and specifically the Helmholtz layer,[16] the proposed models remain essentially experimentally unvalidated.[17] Purely electrostatic descriptions of the double layer, such as the Gouy-Chapman model, predict that away from the potential of zero charge the capacitance of the double-layer increases exponentially as a function of potential.[18] In reality the electrochemical double layer capacitance of a metallic interface rapidly reaches a near constant maximum value of order of 20 μF cm^{-2}.[19] Any simulations that implicitly or explicitly employ a Gouy-Chapman type electrostatic model for the electrochemical double layer will necessarily overestimate the influence of the double layer on the Faradaic response.[20, 21] Consequently, a possible impasse is reached, without a good molecular model for the electrical double layer how can one start thinking about modelling nanoscale reactions? First, it should be recognised that, most commonly, electrochemical experiments focus on the measurement of the oxidation or reduction of a solution phase redox species. Such Faradaic processes are only measurable when the current is appreciably larger than the background or 'non-Faradaic' current associated with the capacitance of the electrode, that is the signal-to-background ratio is large enough for the process of interest to be studied. Second, in an electrochemical cell, it is the passage of current that causes charge separation which leads to the build-up of an electric field in the solution phase. Consequently, in many experimental cases, it will be the Faradaic current that will be

the most important factor in controlling the extent of the electric field and hence potential drop through the solution phase. When modelling electrochemical reactions at the nanoscale, an arguably suitable first approximation is to assume that the charge on the electrode does not contribute to, or alter, the electric field local to the electrode. This assumption is equivalent to using a zero-field approximation at the electrode surface.[22] The zero-field approximation sets the gradient of the electric field as zero at the electrode interface and uses this expression as a boundary condition for the Poisson equation.

A significant amount of recent work in the literature has focused on the study of the redox properties and the detection of individual silver nanoparticles. This work has included studies both in the presence and absence of excess electrolyte, the results of which indicate that the oxidation of this nanoparticulate material is highly sensitive to the presence of solution phase halide anions. [23-25] However, prior to considering nanoscale electrochemical reactions, this work aims to develop a simple model for the deposition and stripping of silver onto a microelectrode, focusing on first, evidencing how the absence of supporting electrolyte is anticipated to affect the voltammetric behaviour of the system and to ascertain at what length scales the breakdown of electroneutrality needs to be considered. Second, we experimentally turn to focus on determining to what extent this simplified model can be experimentally validated at the macroscale. This experimental data highlight how the nucleation kinetics for the deposition of silver is significantly altered in the absence of electrolyte.

6.2 Experimental

Silver trifluoromethanesulfonate (AgOTf, $\geqslant$ 99.95% trace metals basis, Sigma-Aldrich), sodium perchlorate ($NaClO_4$, ACS reagent, 98.0%, Sigma-Aldrich), hexaammineruthenium(III) chloride ($[Ru(NH_3)_6]Cl_3$, Aldrich, 98%) and potassium chloride (KCl, Aldrich, > 99%) were

used as received without further purification. Solutions were prepared using deionised water (Millipore Water Systems, UK) with instantaneous system measured resistivity of 18.2 MΩ cm and bubbled for at least 5 min with N_2 (99.998%, BOC, U.K.) prior to each experiment.

Silver stripping experiments were performed at 298 K with an in-lab built potentiostat, as previously described.[26] Gold microdiscs (5.4 μm radius from ALS Co. Ltd., Japan and homemade 26 μm radius) were used as working electrodes, a platinum wire and silver wire were used as the counter electrode and the reference electrode, respectively. The radii of the gold microdiscs were determined by Cyclic Voltammetry programme (**Appendix C**) operated through μ-Autolab potentiostat (Eco-Chemie, Netherlands) inside a temperature controlled Faraday cage with 1.0 mM $[Ru(NH_3)_6]Cl_3$/0.10 M KCl solution at 298 K.

6.3 Theory

The voltammetric response associated with metal deposition and stripping was studied under full-support to self-support conditions at a hemispherical microelectrode. The model accounts for a cationic solution phase species, A^+ being reduced via a single electron transfer to a deposited solid species B in the presence of a variable amount of inert supporting electrolyte, as given by:

$$A^+(aq) + e^- \rightleftharpoons B(s) \qquad \textbf{(6.1)}$$

In particular, the model presented in this work accounts for the influence of the electrolyte concentration (species M^{z+} and X^{z-}) on the electrochemical reaction, this is achieved by solving the Nernst-Plank-Poisson equations in the solution phase. The presented model is in part related to approaches provided in the literature[7, 27], specifically that reported by Dickinson *et al.*[28] which focused on the formation of a mercury amalgam and Model B presented in the work of by Ward-Jones *et al.*[29] where a comparable boundary condition was used for metal deposition

and stripping. However, in contrast to the above-mentioned literature, this work particularly considers the deposition of a solid onto the electrode surface rather than amalgam formation where in this latter case the mass-transport of the deposited metal inside the electrode needs to be considered. Furthermore the zero-field approximation has greater accuracy[28] in the low support condition relative to widely used electroneutrality approximation. The used dimensionless parameters are tabulated in **Table 6.1** It was noticed further that in the work of Ward-Jones *et al.* [29] the surface coverage of the deposited material is expressed as a fraction of a monolayer. In the present work the quantity of the deposited material is defined as a dimensionless thickness (relative to the size of the electrode). As the simulation was not limied to only considering sub-monolayer coverages and also study electrodes of relatively small dimensions (μm) it is important to monitor to what extent the deposited layer thickness is comparable to the size of the electrode. In the case that the deposited layer thickness becomes large as compared to the size of the electrode then the assumption that the electrode radius does not change during the course of the voltammetric scan is violated.

Table 6.1 Definitions of the Dimensionless Parameters used in this work, where c* is the standard concentration 1 mol dm^{-3}

Unit parameters	Interpretation	Dimensionless parameters
r (m)	Radius of the electrode	
M (g mol^{-1})	Molecular or atomic mass of the deposited solid	
ρ (g m^{-3})	Density of the deposited solid	
r' (m)	Space coordinate	$R = r'/r$
c (mM)	Concentration	$C_i = c_i / c_*$
D (m^2 s^{-1})	Diffusion Coefficient	$d_i = D_i/D_A$
χ (m)	Deposited layer thickness	$X = \rho \chi / rMc^*$

Table 6.1 (continued)		
t (s)	Experimental time	$T = D_A t/r^2$
***k₀* (m s^{-1})**	Standard electrochemical rate constant	$K_0 = k_0 r/D_A$
ϕ (V)	Electrostatic Potential	$\Phi = \phi F/RT$
E (V)	Electrode Potential	$\Theta = (E-E_f^0)F/RT$
ν (V s^{-1})	Scan Rate	$\sigma = r^2 F\nu/D_A RT$

6.3.1 Nernst Plank Poisson (NPP) Equations

Under spherical coordinates and using dimensionless parameters the *Nernst-Planck* equation are:[27]

$$\frac{\partial C_i}{\partial T} = d_i\left(\frac{\partial^2 C_i}{\partial R^2} + \frac{2}{R}\frac{\partial C_i}{\partial R}\right) + d_i z_i\left(\frac{\partial C_i}{\partial R}\frac{\partial \Phi}{\partial R} + C_i\frac{\partial^2 \Phi}{\partial R^2} + C_i\frac{2}{R}\frac{\partial \Phi}{\partial R}\right) \quad (\mathbf{6.2})$$

Where i stands for any solution phase species A, M and X. Here, A is the redox active analyte as defined in equation 1. M and X are the non-electroactive ionic species. To maintain overall electro-neutrality in the system and given that A is taken to be a singly charged cation then the concentration of the non-electroactive anion (X) is set as equal to $C_{sup} + C_A$ (see below in equation 6), where C_{sup} is the concentration of the supporting electrolyte and the concentration of the non-electroactive cation (M) is equal to C_{sup}.

The Poisson equation is used to relate the dimensionless potential to the local electric charge density, again in dimensionless form the equation is:

$$-{R_e}^2 \sum_i z_i C_i = \frac{\partial^2 \Phi}{\partial R^2} + \frac{2}{R}\frac{\partial \Phi}{\partial R} \quad (\mathbf{6.3})$$

where R_e is related to the systems Debye-length relative to the size of the electrode.

$$R_e = \sqrt{\frac{F^2 c^* r^2}{RT\varepsilon_s \varepsilon_0}} \quad (\mathbf{6.4})$$

ε_0 is the permittivity of free space (8.854x10^{-12} F m^{-1}) and ε_s is the relative permittivity of the solvent.

6.3.2 Boundary Conditions

The model considers a one electron transfer leading to cathodic metal deposition and anodic stripping during the course of a cyclic voltammogram under weak support conditions (limited supporting electrolyte). Boundary conditions were set to solve the NPP equation. Initially at the electrode interface species B is not present, both the concentration and potential profiles are assumed to be uniform. While in the bulk solution after the experiment starts, electroneutrality is maintained and the potential drop approaches zero away from the electrode interface.

Hence, the initial (T = 0, R ≥ 1) and outer boundary conditions (T > 0, R = R_{max}) are

$C_A = c_A/c^*$, $\Phi = 0$ (T = 0, R ≥ 1), (**6.5**)

$$C_M = C_{sup},\ C_X = C_{sup} + C_A,\ \Phi(R=R_{max}) + R_{max}\frac{\partial\Phi}{\partial R}\Big)_{R=R_{max}} = 0 \ (T > 0,\ R = R_{max}). \quad (\mathbf{6.6})$$

where c* is the standard concentration 1 mol dm^{-3}. At the electrode interface (R = 1) the zero-field approximation[22] is used as a boundary condition implying complete decoupling of the double layer from the potential distribution near the electrode. Moreover, the flux of the electrolyte cation and anion are similarly set to zero at the electrode interface as expressed below.

$$\left(\frac{\partial\Phi}{\partial R}\right)_{R=1} = \left(\frac{\partial C_M}{\partial R}\right)_{R=1} = \left(\frac{\partial C_X}{\partial R}\right)_{R=1} = 0 \quad (\mathbf{6.7})$$

The variation of the surface coverage $\sigma(X)$ as expresses as a layer thickness of the deposited material necessarily needs to be accounted for in the simulation model. The Butler-Volmer formalism is used to describe the electron transfer kinetics. However, the overpotential is modified to account for the drop in potential across the solution phase.

$$\left.\frac{\partial C_A}{\partial R}\right)_{R=1} = K_0 \exp\big((\beta-1)(\Theta-\Phi_0)\big)\, C_A - \sigma(X) K_0 \exp\big(\beta(\Theta-\Phi_0)\big) \qquad (\mathbf{6.8})$$

Here β is the transfer coefficient, K_0 is the dimensionless standard rate constant, Θ is the applied dimensionless potential and Φ_0 is the dimensionless solution phase potential adjacent to the electrochemical interface. $\sigma(X)$ varies as a function of the thickness of the deposited layer, in the absence of deposited material on the electrode surface i.e. when X = 0, then $\sigma(X)$ takes a value of zero. Herein, it is assumed that the deposited layer thickness is minimal in comparison to the size of the electrode and hence the electrode radius is taken as a constant during the course of the simulated experiment. In the simplest case where $\sigma(X)$ is binary then this model would be directly comparable to boundary condition used in Model C[29] from the work of Ward-Jones *et al.* However, such a model leads to a singularity in the simulation and has associated convergence issues. Consequently, in this work a smoothed algebraic sigmoidal function is used to transition between a value of unity and zero.

$$\sigma(X) = \frac{X}{X_{ML}\left(1+\left(\frac{X}{X_{ML}}\right)^n\right)^{1/n}} \qquad (\mathbf{6.9})$$

where X_{ML} is the dimensionless thickness of a single monolayer of deposited material and n is an arbitrary smoothing value. For large values of X this function has a value of unity and at small values of X (relative to X_{ML}) the expression has a limiting value of X/X_{ML}. This smoothed function results in a simulation model that is comparable to Model B[29] provided by Ward-Jones *et al.*, except that in this work the full Nernst-Plank-Poisson equation set is solved for as

opposed to the diffusion only simulation provided by Ward-Jones *et al*. The value of n in equation 6 controls the smoothness of the transition of $\sigma(X)$ across the two regime, in this work a value of 4 was used, providing a relatively sharp transition while still allowing the simulation to converge.

Additionally from the conservation of mass:

$$\frac{\partial X}{\partial T}\Big)_{R=1} = \frac{\partial C_A}{\partial R}\Big)_{R=1} \quad \textbf{(6.10)}$$

The resulting Jacobian matrix has 12 diagonals when the unknowns are ordered X^k, $C_{A,0}$, Φ_0, $C_{M,0}$, $C_{X,0}$, $C_{A,1}$, Φ_1, $C_{M,1}$, $C_{X,1}$, ...

6.3.3 Numerical Methods

The NPP set of equations were solved using a finite difference method. Between the electrode surface and a maximum distance away from the electrode[30] ($R_{max} = 1 + 6\sqrt{d_{max}T_{max}}$ (**5.11**)) an expanding grid[31] is used to discretise the space, this grid provides a dense mesh near the electrode surface below a threshold value of R_s+1 and expands at rate proportional to $\gamma_R$beyond R_s+1 as given by;

$$R[i] = R[i-1] + \gamma_R R_s \qquad 1<R< R_s+1 \quad \textbf{(6.12)}$$

$$R[i] = R[i-1] + \gamma_R (R[i-1] - 1) \qquad R_{max}>R>R_s+1 \quad \textbf{(6.13)}$$

here *i* relates to the grid indexing. Optimal grid parameters were found to be $\gamma_R = 5 \times 10^{-3}$and $R_s = 2\times10^{-3}$. The potential of the system was varied linearly with time, a potential step of 2×10^{-4} V between each subsequent simulated time step was used throughout this work.

The discretised set of simultaneous nonlinear equations was solved iteratively via the Newton-Raphson method. The convergence tolerance criterion required that the magnitude of the

correction term in the concentrations must be less than 1×10^{-8}. All simulations were scripted in Python 3.5, CPU intensive routines were precompiled into C using Cython. The diagonally banded matrix system resulting from the Newton-Raphson method was solved using the LAPACK 'gbsv' routine as provided as part of the SciPy package.

6.4 Results and Discussions

First, the theoretical model and present a series of simulation results are discussed. The simulation considers the situation in which the electron transfer is fast so that the electrochemical reaction is ''fully reversible''; consequently, any distortions in the voltammetry are necessarily associated with the occurrence of Ohmic drop through the solution phase rather than a changed electron transfer rate at the electrode-solution interface. The theoretical results enable discussion of both how migration and Ohmic drop alters the voltammetric system and how this influence changes as a function of the electrode size relative to the Debye length of the system.

The voltammetric response for the electrochemical reduction of a solution phase species A^+ (1 mM) to a surface-confined solid B was simulated at a micro-hemispherical electrode (radius = 10 μm) as a function of the supporting electrolyte concentration. The simulated response is depicted in **Figure 6.1 a**, here the scan has been initiated at 0.2 V and the potential swept cathodically at a rate of 0.01 V s^{-1} to -1.0 V before returning to + 0.2 V. The rate of electron transfer has been set arbitrarily high with a k^0 of 1×10^3 cm s^{-1} which is large enough to ensure full electrochemical reversibility. On the forward sweep, the solution phase species is reduced at a mass-transport limited rate, resulting in a steady-state reductive current. The return sweep leads to the oxidative removal (stripping) of the deposited material from the electrode surface.

During this stripping wave, the current increases as a function of potential and then drops rapidly when all of the deposited material has been oxidatively removed from the interface.

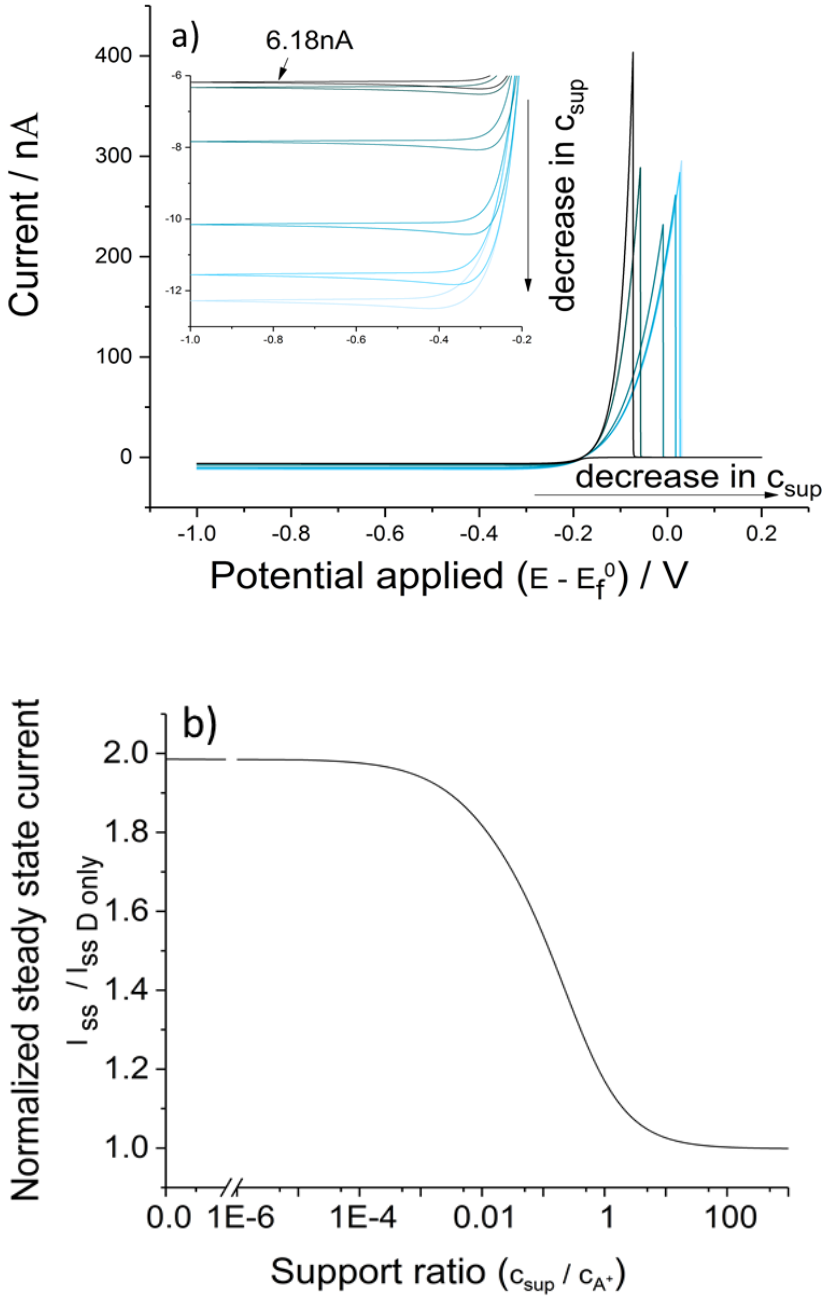


Figure 6.1 Simulation of the voltammetric response for the cathodic deposition and stripping of a mono-valent cation (1 mM) at a 10 µm hemisphere electrode a) as a function of the supporting electrolyte concentration c_{sup}, b) as a function of support ratio (c_{sup} / c_{A^+}). Scan rate = 0.01 Vs^{-1}, 298K, all diffusion coefficients are equal with a value of D $=1\times10^{-9}$ m^2s^{-1}, c_{sup} refers to supporting electrolyte concentration and c_{A^+} refers to the analyte concentration, both in mol dm^{-3}

Here the effect of the supporting electrolyte ratio on the reductive mass-transport limited current was considered. The inlay of **Figure 6.1 a** shows a zoomed-in plot depicting the reductive current and its variation as a function of the supporting electrolyte concentration. In the absence of an electric field extending into the solution phase, as is the case in the presence of an excess of supporting electrolyte, then the second term on the right-hand side of the **Equation 6.2** is essentially zero. Consequently, the mass-transport of the cations can be considered solely in terms of diffusion; **Equation 6.2** is reduced to the diffusion equation. Under these conditions the reductive steady-state diffusion only current ($I_{D,ss}$) at a hemi-spherical electrode is described by:[32]

$$I_{D,ss} = 2\pi nFDcr \qquad (\mathbf{6.14})$$

where D is the diffusion coefficient ($m^2\ s^{-1}$) of the electroactive species, c is the solution phase concentration of the analyte and r is the electrode radius (m). For the above simulated system this results in a predicted current of 6.18 nA as plotted on the inlay of **Figure 6.1 a**. The removal of supporting electrolyte leads to an increase in the steady-state current; here the electric field produced by the occurrence of the electrochemical reaction serves to alter the mass-transport of ions in the vicinity of the electrode. For the present case, the produced net negative charge adjacent to the electrode interface causes an increase in flux of the electroactive cations towards the electrode. This contribution of migration to the flux leads to an increase in the steady-state mass-transport limited current. Whether the electric field induced by the electrochemical reactions cause an increase or decrease in the steady-state current and the magnitude of the effect depends primarily on the charge of the electroactive species and the number of electrons transferred during the course of the electrochemical reaction.[33] The results show that for the one-electron reduction of a mono-valent cation studied here than in the absence of supporting electrolyte the mass-transport limiting current is, under conditions where

electroneutrality holds, two times larger than that expected on the basis of a diffusion-only situation.

Figure 6.1 a shows that with decreasing supporting electrolyte concentration the oxidative stripping wave shifts to more positive potentials. This distortion of the oxidative stripping wave reflects the presence of an electric field extending away from the electrode which necessarily implies the presence of a potential drop in the solution phase. This potential drop serves to decrease the thermodynamic driving force for the electrochemical reaction; consequently, a higher overpotential needs to be applied to the system for the electron transfer to be driven. This distortion of the oxidative stripping wave does not reflect the presence of a charged finite electron transfer rate as the electrochemical rate constant was set sufficiently large to ensure electrochemical reversibility. **Figure 6.1 b** is a working curve which depicts how, for a one-electron reduction of A^+ the steady-state reductive current is predicted to vary as a function of the support ratio. When the supporting electrolyte is in excess then a diffusion only flux is measured, further under self-support conditions, the steady-state current is nearly double that predicted for the diffusion only case. For support ratios in the range of ca 0.1 to 1.0 the steady-state current transitions between these two limits.

The result of **Figure 6.1b** is valid in cases where electro-neutrality holds. The above discussion has focused on using the steady-state current as a parameter to quantify this change from the diffusion only to the low-support regime. However, other parameters such as the peak position for the stripping wave could equally be employed to quantify this transition. The **Appendix C** explores how the peak position for the stripping wave varies as a function of the supporting electrolyte ratio. The following seeks to investigate how this situation differs for this simulation model as the Debye length becomes comparable to or greater than the radius of the electrode.

In order to investigate this transition, the theoretical results focus on the self-supported case, such that the concentration of the supporting electrolyte is zero.

For an ionic solution, the Debye length gives a measure of the distance over which Coulombic charges are screened by the ionic atmosphere. For a mono-valent salt the Debye length (x_{DL}) is:[18]

$$x_{DL} = \frac{1}{F}\sqrt{\frac{\varepsilon\varepsilon_0 RT}{2C}} \qquad \textbf{(6.15)}$$

where $\varepsilon_0$is the permittivity of free space (8.85×10^{-12} C V^{-1} m^{-1}), ε is the relative permittivity of the solvent, C is the concentration (mol m^{-3}) of the salt and all other constants are as before. Consequently, the distance over which a charge is screened is inversely proportional to the square-root of the electrolyte concentration. For a millimolar concentration of salt this distance is of the order of 10 nm. Following sections focus on how the simulated steady-state reductive current varies as a function of the Debye length of the system to the electrode radius.

The voltammetric response for the reduction of a solution phase cation in the absence of supporting electrolyte was simulated for a range of electrode radii and cation concentrations. **Figure 6.2** presents a working curve for the simulated steady-state reductive current normalised against the diffusion only value as a function of the Debye length/electrode radius ratio. For systems either containing a high electroactive species concentration or with a relatively large electrode radius (i.e. for small x_{DL}/r), then the system is well described by the electroneutrality approximation. For this case, as is found for the simulated example in **Figure 6.1**, in the absence of supporting electrolyte the mass-transport limited flux to the electrode is double that expected on the basis of a diffusion-only model. However, as the size of the electrode or similarly the concentration of the electroactive species is decreased – leading to a concomitant

increase in the Debye length of the system – even in the absence of additional electrolyte, the magnitude of the steady-state limited current tends towards that of the diffusion-only response.

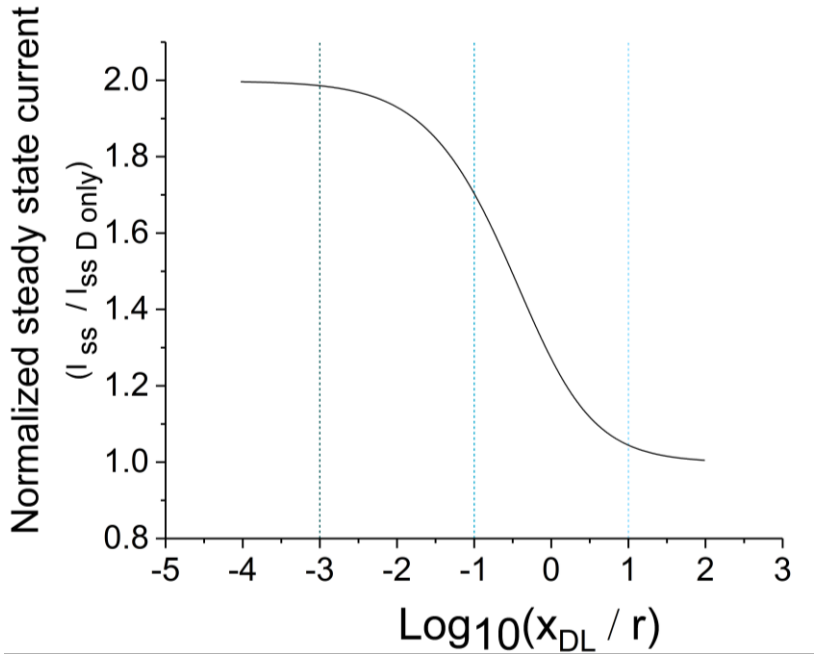


Figure 6.2 Working curve for the magnitude of the simulated steady-state reductive current for a mono-valent cation as a function of the Debye length (x_{DL})/ radius (r) ratio. Vertical dotted lines are representative values of the x_{DL}/r value for electrodes of radius 10 μm for (dark blue dot line); 0.1 μm for (blue dot line); 1 nm for (light blue dot line)

The voltammetric response for the reduction of a solution phase cation in the absence of supporting electrolyte was simulated for a range of electrode radii and cation concentrations. **Figure 6.2** presents a working curve for the simulated steady-state reductive current normalised against the diffusion only value as a function of the Debye length/electrode radius ratio. For systems either containing a high electroactive species concentration or with a relatively large electrode radius (i.e. for small x_{DL}/r), then the system is well described by the electroneutrality approximation. For this case, as is found for the simulated example in **Figure 6.1**, in the absence of supporting electrolyte the mass-transport limited flux to the electrode is double that expected on the basis of a diffusion-only model. However, as the size of the electrode or similarly the concentration of the electroactive species is decreased – leading to a concomitant

increase in the Debye length of the system – even in the absence of additional electrolyte, the magnitude of the steady-state limited current tends towards that of the diffusion-only response.

For a micro-electrode, the length scale over which the concentration of the electroactive species is altered is relative to the electrode radius. When the Debye length is small as compared to the radius of the electrode, then electroneutrality holds across virtually the entirety of the electroactive species depletion layer surrounding the electrochemical interface. Hence, migration influences the mass-transport of charged species to and from the electrode. Conversely, when the Debye length is comparable to, or greater than, the size of the electrochemical interface then electroneutrality does not hold in the depletion layer and the contribution of migration to the mass-transport of ions in the vicinity of the electrode is diminished. Consequently, in this latter case even when the electrochemical reaction is 'self-supported' no significant Ohmic drop occurs through the solution phase and hence the mass-transport regime returns to being diffusional. Overlaid on **Figure 6.2** are three vertical lines representing values for the Debye length/electrode radius ratio where the concentration of the mono-valent electroactive species is 1 mM and the radius of the electrode is 10000, 100 and 1 nm in size. Stated succinctly, at the nanoscale electro-neutrality breaks down, consequently, the influence of migration on such systems is minimised. However, the influence of the break-down of electroneutrality is, on the basis of **Figure 6.2**, anticipated to be experimentally measurable for some experimental conditions even before the electrode becomes nanoscopic in dimension.

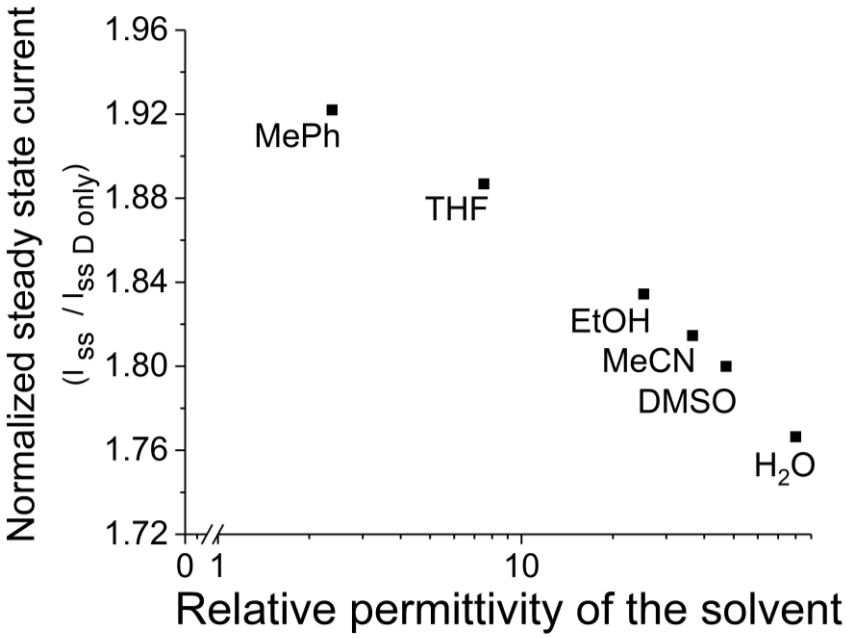


Figure 6.3 Simulation of the mono-charge metal stripping normalized current with relative permittivity of solvent variation at 1µm radius hemisphere electrode. Scan rate = 0.01 V s^{-1}, c_{Sup} = 0.02 mM, 100 mM supporting electrolyte if used, 293 K, D = 1×10^{-9} m^2s^{-1}, E_f^0 = 0.0 V

The extent to which the breakdown of electroneutrality is important is, as shown above, sensitive to the Debye length of the system. Furthermore, as expressed by **Equation 6.14**, the magnitude of the Debye length is proportional to the square-root of the relative permittivity of the solvent. Consequently, the voltammetric response of a self-supported system will depend not only on the concentration of the used electrolyte and the electrode size but will also be influenced to some extent by the electrochemical solvent. To exemplify this point the voltammetric response of a 1 µm radius electrode in a solution containing 20 µM of an electroactive mono-valent species was simulated with a range of relative permittivities representative of those used as electrochemical solvents. **Figure 6.3** depicts for these simulated systems, the expected variation in the magnitude of the reductive current as a function of the solvent. The high relative permittivity of water means that the breakdown of electroneutrality is of greatest influence on aqueous-based systems.

What is the validity of the above simulation model and to what extent can the results be confirmed experimentally? Figure 6.**2** suggests that a plausible route to gaining insight into the behaviour of electrochemical reactions at the nanoscale may be achieved through the investigation of processes at the micron scale but under extreme low-support conditions. The electrochemical behaviour of a 10 μM solution at a 1 micron electrode is anticipated to behave similarly to a 10 nm electrode in a 100 millimolar solution. However, it should be recognised that there are physical limits to the extent to which such an approach is applicable. The above model assumes the presence of no other ions in the solution phase than those of the electroactive salt. Distilled water in the limit of full purity will contain ~0.1 μM of hydroxide and protons (pK_w = 13.996 at 298 K).[18] In actuality the attainment of such a low conductivity is challenging. The presence of dissolved carbon dioxide regularly leads to the presence of micromolar concentrations of carbonate ions in the solution phase.[34] Moreover, care has to be taken due to the ease of adventitiously introducing other ions into the solution. These complexities aside the work now turn to experimentally study the deposition and stripping of silver metal from a planar microdisc electrode instead of the hemisphere microelectrode as simulated.

The cathodic deposition of silver from a solution containing 1 mM silver triflate was studied voltammetrically (from 0.5 to -0.75 V vs Ag) at a 26 μm radius gold disc electrode in both the presence and absence of 100 mM sodium perchlorate. In the presence of supporting electrolyte the diffusion limited reduction current is expected to be 16.5 nA which is calculated from **Equation 6.13** (assuming $D_{Ag+} = 1.65 \times 10^{-9}$ m^2 s^{-1})[35] and is very comparable to the experimentally measured value of 18.2 nA as shown in **Figure 6.4**. In the absence of supporting electrolyte although the reduction of silver onsets at a comparable potential, the current at low overpotentials (ca. -0.1V) does not increase monotonically. Furthermore at high overpotentials no clear steady-state is reached with the current clearly increasing at more reductive potentials

beyond -0.4 V. Moreover, the magnitude of this current is appreciably greater than double that of the diffusion limited reaction rate.

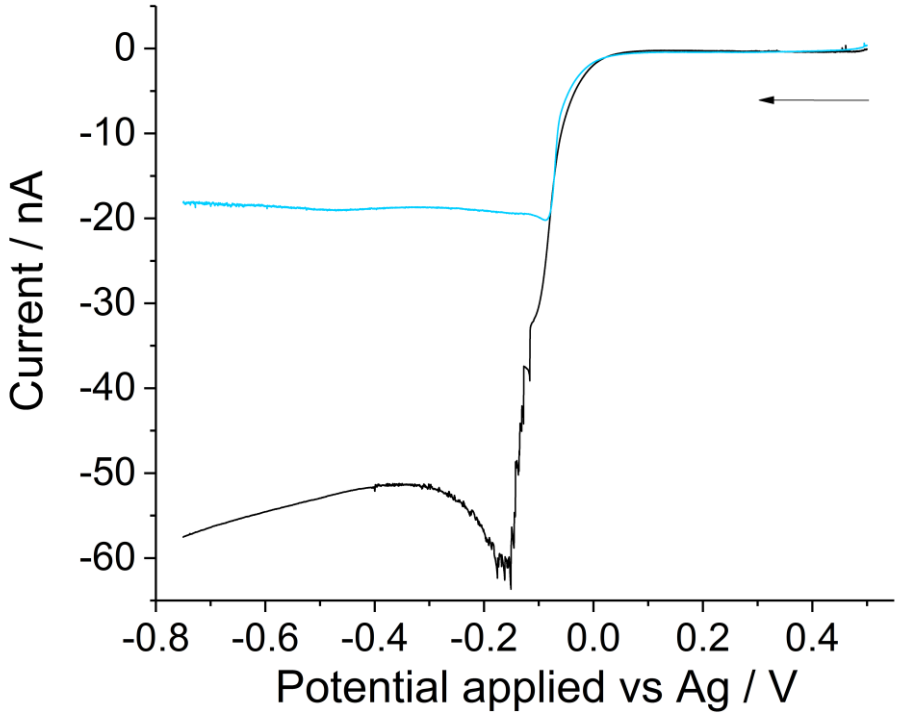


Figure 6.4 Silver deposition with/ without supporting electrolyte. All experiments carried out with 0.1 V s^{-1}, 1 mM AgOTf under 298 K on a gold microdisc where r_{Au} = 26 µm; the blue line represents an experiment with 0.1 M $NaClO_4$ and the black line for the case without.

These deviations of the experiment away from that expected theoretical behaviour reflect the fact that the deposition process is more complex than has been considered in the above theoretical description. First, the above theory assumes the electrode to be uniformly accessible. Second, nucleation of the material on to the electrode surface has not been accounted for. The nucleation rate of the metal to the electrode surface will depend on the magnitude of the applied overpotential[36], the sharp steps in current observed at low overpotentials for the deposition of silver in the absence of additional electrolyte can be interpreted as a slow nucleation of the silver metal on to the gold surface followed by localised rapid growth. This non-homogeneous silver deposition of the metal will lead to dendritic deposition of the metal onto the gold

electrode surface. Consequently, although the amount of metal deposited during the course of the voltammograms presented in **Figure 6.4** is comparatively small, ca. 1.9 pmol which is equivalent of a 9 nm uniform thickness of silver deposition on to a disc of radius 26 µm, the highly non-uniform deposition arising from the mass-transport regime and relatively slow nucleation results in the *effective* size of the electrode increasing during the course of the deposition processes. This increase in the electrode geometry is directly reflected in the deposition current not reaching a true steady-state in the absence of additional electrolyte and becomes significant at high overpotentials. Notably, such nucleation issues were even more pronounced with the use of a carbon electrode (data not shown).

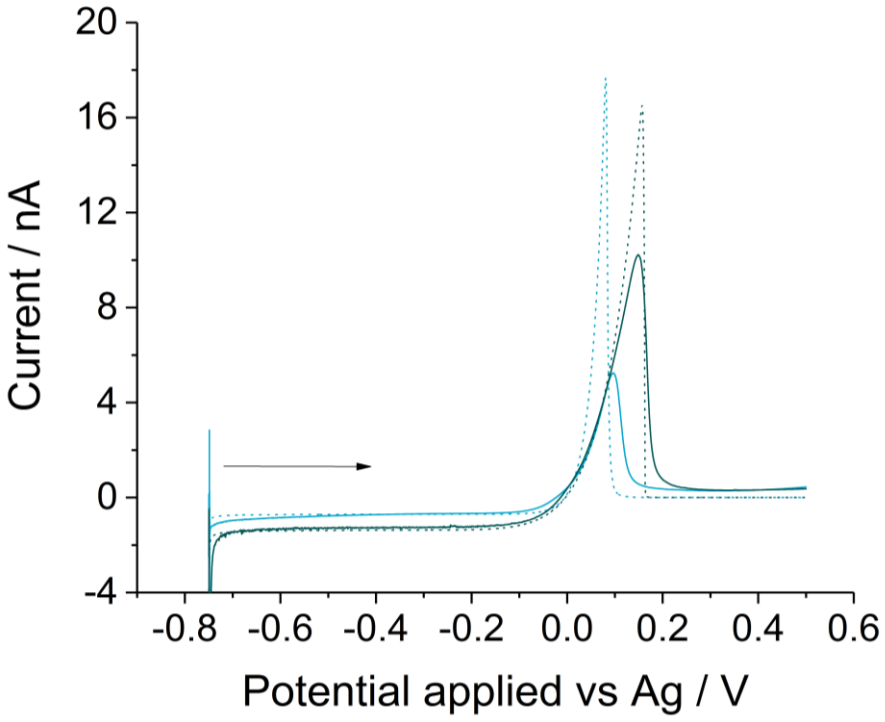


Figure 6.5 Silver stripping with/without supporting electrolyte. All experiments carried out with 0.2 V s^{-1}, 0.2 mM AgOTf under 298 K on a gold microdisc where r_{Au} = 5.4 µm. the light blue line and light blue dots refer to silver stripping without supporting electrolyte, experimental and simulation results representatively; dark blue line and dark blue dots refer to silver stripping with 0.1 M $NaClO_4$, experimental and simulation results representatively, experiment with $NaClO_4$ was done 30s after holding at 0.4 V for 10 s.

In order to, at least in part, overcome these experimental issues, the voltammetric scan was subsequently initiated at a negative potential. At these high overpotentials the nucleation kinetics are expected to be rapid consequently the initially formed silver layer is expected to be more homogeneous. By application of this technique of starting the voltammogram at a high overpotential, these issues associated with non-homogeneous silver deposition could be mitigated. **Figure 6.5** depicts the linear sweep voltammetry for the deposition and oxidative stripping of silver onto and from a gold microelectrode (radius = 5.4 um). The scan is started at -0.75 V and scanned anodically at a scan rate of 0.2 V s^{-1} to 0.5 V. Overlaid in dotted lines is the simulated response for this system as provided by the theoretical model explored earlier in this work. The theoretical model assumes a hemispherical as opposed to a disc electrode geometry. Consequently, for the simulation an effective radius of 3.41 μm was used as opposed to the actual calibrated value of 5.4 μm to ensure the mass-transport limiting current were equal; these two values differ by a factor of $2/\pi$.

For the experimentally used silver ion concentration of 0.2 mM, the Debye length of the systems is on the basis of **Equation 6.14** is 21.3 nm. Taking the electrode effective radius then the log of the ratio and the Debye length to the electrode radius is -2.2. Hence, on the basis of **Figure 6.2** and from the simulations presented in **Figure 6.5**, the mass-transport limited current for the reduction of the metal ion is expected to be marginally less than the value of 2 with a value of 1.94. This lower value is, as discussed due to the limitation of the assumption of electroneutrality. Experimentally the ratio of the reductive current in the presence and absence of supporting electrolyte was found to be 1.9 ± 0.03, which is consistent with the results presented above. As can also be seen in **Figure 6.5** the experimental change in the reductive steady-state current due to the effect of migration is well accounted for by the provided simulation. Moreover, in the absence of electrolyte, the shape and magnitude of the oxidative

stripping peak are also apparently well described by the simulation model. However, the distinctly different voltammetric stripping waveshape predicted by the simulation in the presence of electrolyte was not observed experimentally. This lack of fit plausibly reflects the errors associated with assuming that the disc electrode can be described using a hemispherical geometry. The hemisphere is uniformly accessible as opposed to the disc geometry which is not. This may also be an explanation for why the measured difference in the steady-state limiting currents is actually greater than that predicted theoretically. Consequently, further work in the future may beneficially consider the voltammetric response of a more accurate 2D model of the microdisc electrode system.

The above work has focused on the reduction of a cation to a natural deposited solid (metal). However, the results also have implications for reactions such as the oxidation of silver in the presence of halides. Here although an oxidation is being considered, the half-cell reaction again results in the net removal of charge in the vicinity of the electrode/nanoparticle. Recent work has emphasised, under some circumstances, the *possible* importance of the rate of mass-transport of the halide ions in controlling the rate of the oxidation reaction at the nanoscale. [23, 37] However, for these self-supporting reactions the influence of not only diffusion but also migration and its sensitivity to the Debye length of the system and size of the electrochemical interface needs to be more fully considered.

6.5 Conclusions

The deposition of an electroactive cation to a deposited solid in the presence and absence of additional supporting electrolyte has been studied both theoretically and experimentally. Theoretical models present in the literature that either implicitly or explicitly assume the capacitance of the electrode is well described by an electrostatic Gouy-Chapman type model

and account for the influence of this electric field on the mass-transport of the electroactive ions, necessarily overestimate the importance of the double layer on the resulting voltammetric response. In this work a different approximation was made and the limiting case was studied where the influence of the electrical double layer is assumed to contribute negligibly to the electric field in the vicinity of the electrode. Hence, the theoretical results are modelled on the basis of the electric field being solely related to the separation of charge associated with the occurrence of the (Faradaic) electrochemical process. The first major conclusion of this theoretical analysis is that as expected for the modelled system when the Debye length of the system is comparable to the electrode radius the assumption of electroneutrality breaks down. Consequently, for either low support conditions or for nanoscopic electrodes the influence of migration caused by solution phase potential drop is minimised. Hence, in the limit of a large x_{DL}/r ratio the mass-transport flux to the electrode becomes well described by a diffusion-only model. A further major conclusion from this theoretical model is that this influence of the break-down of electronuetrality is anticipated to become experimentally measurable under some low support conditions even before the electrode becomes nanoscopic in dimension.

Experimentally work focuses on validating these presented results where the deposition and stripping of silver metal are used as an example system. Issues - specifically changes in the metals nucleation rate in the absence of electrolyte-associated with the non-ideality of the system - are highlighted. However experimentally, the steady-state current for the reduction of a 0.2 mM solution of silver ions at a gold microdisc electrode (radius = 5.4 um) in the absence of electrolyte, is less than two times greater than that of the diffusion-only limited flux as predicted by the above model. The limitations of the modelling are understood on the basis of the provided theoretical analysis being predicated on a hemispherical as opposed to a disc electrode geometry.

Bibliography

1. Y. Guo, M. Yang, C. Batchelor-McAuley and R. G. Compton, *J. Electroanal. Chem.*, 2019, **849**, 113370.
2. J. Newman and K. E. Thomas-Alyea, *Electrochemical Systems*, Wiley, 2012.
3. D. Deconinck, S. Van Damme and J. Deconinck, *Electrochim. Acta*, 2012, **69**, 120-127.
4. U. Schroder, K. B. Oldham, J. C. Myland, P. J. Mahon and F. Scholz, *J. Solid State Electrochem.*, 2000, **4**, 314-324.
5. R. Zhang, X. Duan, M. Ding and T. Shi, *J Phys Chem B*, 2018, **122**, 6656-6665.
6. C. Picioreanu, M. C. van Loosdrecht, T. P. Curtis and K. Scott, *Bioelectrochemistry*, 2010, **78**, 8-24.
7. R. G. Compton, E. Laborda and K. R. Ward, *Understanding Voltammetry: Simulation Of Electrode Processes*, World Scientific Publishing Company, 2013.
8. E. J. F. Dickinson, J. G. Limon-Petersen and R. G. Compton, *J. Solid State Electrochem.*, 2011, **15**, 1335-1345.
9. K. R. Wehmeyer, M. R. Deakin and R. M. Wightman, *Anal. Chem.*, 1985, **57**, 1913-1916.
10. R. W. Murray, *Chem. Rev.*, 2008, 108, 2688-2720.
11. Y. Shao, M. V. Mirkin, G. Fish, S. Kokotov, D. Palanker and A. Lewis, *Anal. Chem.*, 1997, **69**, 1627-1634.
12. J. Velmurugan, D. Zhan and M. V. Mirkin, *Nat. Chem.*, 2010, **2**, 498-502.
13. S. V. Sokolov, S. Eloul, E. Kätelhön, C. Batchelor-McAuley and R. G. Compton, *Phys. Chem. Chem. Phys.*, 2017, **19**, 28-43.
14. L. K. Allerston and N. V. Rees, *Curr Opin Electroche*, 2018, **10**, 31-36.
15. K. J. Stevenson and K. Tschulik, *Curr Opin Electroche*, 2017, **6**, 38-45.
16. P. Delahay, *Double Layer and Electrode Kinetics*, John Wiley & Sons, Incorporated, 1965.
17. M. Favaro, B. Jeong, P. N. Ross, J. Yano, Z. Hussain, Z. Liu and E. J. Crumlin, *Nat. Commun.*, 2016, **7**, 12695.
18. W. J. Albery, *Electrode kinetics*, Clarendon Press, 1975.
19. B. B. Damaskin and A. N. Frumkin, *Electrochim. Acta*, 1974, **19**, 173-176.
20. C. P. Smith and H. S. White, *Anal. Chem.*, 1993, **65**, 3343-3353.
21. E. J. F. Dickinson and R. G. Compton, *J. Electroanal. Chem.* , 2011, **661**, 198-212.
22. E. J. F. Dickinson and R. G. Compton, *Chem. Phys. Lett.*, 2010, **497**, 178-183.
23. E. N. Saw, N. Blanc, K. Kanokkanchana and K. Tschulik, *Electrochim. Acta*, 2018, **282**, 317-323.
24. K. J. Krause, F. Brings, J. Schnitker, E. Kätelhön, P. Rinklin, D. Mayer, R. G. Compton, S. G. Lemay, A. Offenhäusser and B. Wolfrum, *Chem. Eur. J.*, 2017, **23**, 4638-4643.
25. K. Ngamchuea, R. O. D. Clark, S. V. Sokolov, N. P. Young, C. Batchelor‐McAuley and R. G. Compton, *Chem. Eur. J.*, 2017, **23**, 16085-16096.
26. C. Batchelor-McAuley, J. Ellison, K. Tschulik, P. L. Hurst, R. Boldt and R. G. Compton, *Analyst*, 2015, **140**, 5048-5054.
27. E. J. F. Dickinson, J. G. Limon-Petersen, N. V. Rees and R. G. Compton, *J Phys Chem C*, 2009, **113**, 11157-11171.
28. J. G. Limon-Petersen, E. J. F. Dickinson, T. Doneux, N. V. Rees and R. G. Compton, *J. Phys. Chem. C*, 2010, **114**, 7120-7127.
29. S. E. Ward Jones, F. G. Chevallier, C. A. Paddon and R. G. Compton, *Anal. Chem.*, 2007, **79**, 4110-4119.
30. O. V. Klymenko, A. I. Oleinick, I. Svir and C. Amatore, *Russ. J. Electrochem.*, 2012, **48**, 593-599.
31. D. J. Gavaghan, *J. Electroanal. Chem.* , 1998, **456**, 1-12.
32. Allen J. Bard and L. R. Faulkner, *Electrochemical methods*, Wiley, 2nd Edition edn., 2001.
33. M. Ciszkowska and Z. Stojek, *J. Electroanal. Chem.*, 1999, **466**, 129-143.

34. X. Li, C. Batchelor-McAuley, E. Laborda and R. G. Compton, *Chem. Eur. J.*, 2017, **23**, 15222-15226.
35. J. R. Rumble, D. R. Lide and T. J. Bruno, *CRC Handbook of Chemistry and Physics*, Taylor and Francis, 86th edn., 2006.
36. E. Budevski, G. Staikov and W. J. Lorenz, *Electrochim. Acta*, 2000, **45** 2559–2574.
37. K. Kanokkanchana, E. N. Saw and K. Tschulik, *ChemElectroChem*, 2018, **5**, 3000-3005.

Chapter 7

A Bespoke Chloride Sensor for Mineral Water

Chloride quantification is important in drinking water quality control. A bespoke, rapid and reagent free electrochemical method is reported for a simple and accurate chloride sensor specifically for mineral water without the need for added electrolytes. The voltammetry used embraces first the reduction of oxygen to clean and activate the electrode surface and ensure reproducibility without the requirement for any mechanical polishing, followed by silver chloride formation and stripping. A linear correlation was found with silver chloride stripping peak currents and chloride concentrations within the range of 0.4 mM to 3.2 mM on a silver macro disc electrode. The chloride concentrations in two different mineral water samples were measured giving excellent agreement with independent analysis.

This work presented in this chapter has been published as a first author paper in the *Analyst*[1].

7.1 Introduction

Chloride is one of the major ionic components of natural water[2] the concentration of which is important to both human health[3] as well as, in the case of drinking water, taste. The WHO recommends 20 mg to 100 mg chloride should be consumed via drinking water per person per day[4] and high chloride mineral water (chloride > 200 mg L^{-1}) is widely used in intestinal, bile duct and liver treatments.[5] The recommended upper limit of chloride levels in potable water is given by WHO as 250 mg L^{-1} (ca. 7 mM), but the actual concentration of chloride in branded mineral waters varies significantly from 0.17 mM to 37.7 mM (**Table 7.1**). If the drinking water

has too high a chloride level, an unpleasant salty taste is detectable and the corrosion of pipes delivering the water is likely to occur, releasing in some cases unwanted toxic lead and copper cations into the drinking water supply [4]. Determination of chloride in drinking water is essential.

Table 7.1 Chloride concentrations in common drinking waters[6, 7]

	mg/L	**mM**
WHO limit	250[8]	7
Mineral waters		
Highland	6.1	0.17
Evian	10	0.28
Tesco	14	0.39
Aqua Pura	15	0.42
Volvic	15	0.42
Nestle Pure Life	18	0.51
Buxton	37	1.04
Natural mineral waters		
Voluvesi	7.3	0.2
Saaremaa Vesi	13.4	0.4
Saku	27.1	0.8
Nabeghlavi	42- 95	1.2 - 2.7
Narzan Kislovodsk	100 - 150	2.8 - 4.2
Smironovskaya	250 - 300	7.1 - 8.5
Borjomi (sparkling)	380	10.7
Jernuk	300 - 400	8.5 -11.3
Varska	444	12.5
Vichy	601.5	17.0
Varska original	1338	37.7

Current chloride detection and quantification techniques for application in drinking water include titration, electrochemistry and chromatography[9-11], where ion chromatography is specifically recommended by CEN and ISO[12] for a large number of samples. Each sample is added to a carbonate-bicarbonate eluant. After ion-exchange the separated chloride ions are directed into a suppressor where the eluant is neutralised. Chloride is identified by retention time standards and quantified via conductivity measurements.[10] Apart from facile analysis for multiple samples, ion chromatography also avoids toxic reagents such as silver nitrate or mercury salts as used in titrimetric analysis and a low detection limit of 4 µg L^{-1} chloride can

be achieved if required using ion chromatography. However, one drawback to the method are the costs of consumables, notably the expensive columns and eluants required.

Meanwhile, electrochemical methods have been applied in chloride detection including potentiometry via the chloride ion-selective electrode (Cl-ISE) based on a silver chloride membrane and the coulometric chloridometer. The Cl-ISE can detect chloride in the range 10 µM to 100 µM accurately, but the addition of nitrate reagent is required to maintain stable performance in very dilute solutions.[13] In the coulometric method applied to chloride its concentration is determined by monitoring the conductivity of the analyte solution whilst it is titrated with in situ generated silver ions.[14] However, the equipment requires trained personnel to operate and the addition of reagents is required. Ideally a direct measure of chloride in drinking water is required which simply and exclusively only needs the introduction of a probe into the solution.

Amperometric quantification via voltammetry opens up a possible alternative inexpensive and robust, reagent free method for halides[15-18]. In particular, silver electrodes are analytically useful for chloride in seawater and sweat[19, 20], utilizing the voltammetric response of metallic silver oxidation in chloride media. Notice that these literature studies were done with excess supporting electrolyte or high ionic strength media ('full support' conditions) in contrast to the low ionic strength solutions found in drinking water ('low support' conditions). The challenge in low support conditions is the distortion of voltammetric signals due to significant attraction /repulsion from the charged electrode surface (migration effect).[21] Recently, the feasibility of making quantitative electrochemical reactions in aqueous media without supporting electrolyte has been demonstrated using microelectrodes by Li *et al.*[21] with ultra-low conductivity H_2O (60 nS cm^{-1}). Silver deposition/stripping voltammetry has also been studied in low support aqueous solutions on gold microelectrodes[22, 23], suggesting that the detection of chloride with

silver electrodes in low support aqueous systems may be possible. This chapter explores the possibility of simple voltammetric analysis directly in bottled mineral and tap water without the addition of any reagents, including the supporting electrolyte commonly added to such experiments.

Herein a chloride sensor for bespoke use in drinking water was presented employing a silver macro electrode and utilizing the formation and stripping of silver chloride (**Equation 6.1**) without any added supporting electrolyte or the need for microelectrode instrumentation. In addition, to avoid the need for the cleaning of the electrode the reduction of oxygen naturally present in the water via air saturation (**Reactions 6.2-6.3**) is used as an 'in situ' activation process[20] to activate the electrode surface in a reproducible manner prior to the analysis.

$AgCl_{(s)} + e^- \rightleftharpoons Ag + Cl^-$; $E^o = 0.2223$ V **(7.1)**[24]

$O_2 + e^- \rightleftharpoons O_2^{-\cdot}$; $E^o = -0.284$ V **(7.2)**[24]

$O_2^{-\cdot} + H_2O + e^- \rightleftharpoons HO_2^- + OH^-$; $E^o = 0.2$ V (pH > 11.6) **(7.3)**[24]

Generically the work suggests the feasibility of electro-analysis beyond the constraints imposed by the usual demands of operating with a fully supported solution phase together with rigorous outgassing of the solution which, whilst essential for quantitative physical electrochemistry is seen to be unnecessary in the context of at least some bespoke electroanalytical contexts even when using macro-electrodes.

7.2 Experimental

7.2.1 Chemical Reagents

All chemicals are listed in **Table 3.1**. Potassium chloride (>99.5%, KCl), silver nitrate (>99%, $AgNO_3$) were received from Sigma Aldrich. Potassium nitrate (≥99%, KNO_3) was obtained from Honeywell Fluka. Ultrapure water (spectrophotometric grade, H_2O) was purchased from Alfa Aesar. Tesco Ashbeck water (2000 mL), Volvic Natural Mineral Water (1500 mL) and Borjomi Sparkling mineral water (500 mL) were used as received with the exception that the Borjomi water was analysed after the release of dissolved gas. Then, the Borjomi water was 10 times diluted with Millipore water. The spherical citrate-AgNPs ca.100 nm diameter (Nanoxact, 0.02 mg mL^{-1} silver, 2 mM sodium citrate) were purchased from Nanocomposix, USA. For voltammetry analysing silver chloride peaks with silver nanoparticles, solutions were rigorously degassed with nitrogen gas (N_2, 99.998%, BOC Gases plc, Guildford, UK) at a sufficient flowrate to ensure nitrogen saturation and exclusion of oxygen. For voltammetry analysing both silver chloride peaks and ORR signals at a bulk silver electrode, solutions (5.0 mL) were stirred (400 rpm) under conditions open to the air for 15 min to ensure saturation of air for each measurement. Solutions were prepared using Millipore water with a resistivity of 18.2 MΩ cm at 298 K unless stated otherwise.

7.2.2 Electrochemical Analysis

All electrochemical measurements were performed in a conventional three-electrode cell in a Faraday cage and a μAutolab II potentiostat manufactured by Metrohm-Autolab BV, Utrecht, Netherlands under 298 K. The experimental temperature was maintained constant at 298±0.5 K by a thermostated water bath and the cell consisting of a platinum wire counter

electrode, a homemade $Ag/AgNO_3$ reference electrode (10 mM $AgNO_3$ and 90 mM KNO_3) and a working electrode (WE). The reference electrode consisted of a silver wire submerged in regularly recharged 10 mM $AgNO_3$, 90 mM KNO_3 solution and was calibrated against a Ag/AgCl [saturated KCl] (+0.20 V vs. NHE) reference electrode via cross referencing with the oxygen reduction peak in 0.1 M KNO_3 air-saturated solution. The peaks were found to reproducibly differ by +0.48 V. Thus, this homemade reference has a potential of +0.68 V vs. NHE, in agreement with the previously reported potential of $Ag/AgNO_3$ reference electrode in 10 mM $AgNO_3$ and 90 mM $NaNO_3$ with a value of +0.69 V vs. NHE.[19]

A glassy carbon macro disc electrode (GC, radius 1.49 mm, BAS, Technical, UK) or a silver macro-disc electrode (Ag, homemade, radius 1.13 mm) calibrated in **Appendix A** and **B** [20, 25] were used as working electrodes. Both electrodes were polished using a sequence of 1.0, 0.3 and 0.05 µm alumina lapping compounds (Bucher, Germany).

7.2.3 Chloride Detection on A Silver Macro-electrode

Cyclic voltammetry was conducted in KCl solutions made with Tesco water (Tesco-KCl solutions) or Millipore water (pure KCl solutions) as a solvent to realise a final chloride concentration range of 0.4 mM - 0.32 mM. Each scan was undertaken in air-saturated solutions at 0.10 V s^{-1} from -0.50 V to -0.90 V then anodically to -0.05 V before returning to -0.50 V and repeated three times.

7.2.4 Chloride Detection with Silver Nanoparticles on a GC Electrode

To allow comparison of the silver chloride stripping features between a bulk silver electrode and a silver nanoparticle modified electrode, a suspension of the as-supplied commercial AgNPs with a volume of 15.0 mL was washed with ultrapure water twice. The solution was then centrifuged at 400 rpm for 10 min and 10.0 mL of the supernatant was removed and replaced with a further 10.0 mL ultrapure water for two repetitions. Finally, 14.5 mL of the supernatant was removed, so that 0.5 mL suspension was obtained at 30 times the stock concentration. Before drop-casting onto the GC electrode, the washed AgNPs sample was dispersed by sonication for 15 min. Specifically, after polishing the glassy carbon macro-electrode, 5.0 μL of washed AgNPs was applied to the electrode surface and dried at 343 K for 10min. The electrode was then used to detect chloride levels in Tesco-KCl solutions and compared to that in a blank scan with 1 mM KNO_3. Each scan was undertaken in nitrogen saturated solutions at 0.10 Vs^{-1} from -0.70 V to +0.50 V then returning to -0.70 V and repeated three times.

7.3 Results and Discussions

The proposed detection method was explore, develop and validate in four steps. First, silver chloride formation and stripping were studied in combination with the ORR reaction under both ‘self-support’ and ‘low support’ solutions. The former relates to the total absence of any deliberately added electrolyte whereas the latter experiments had a low level of intentionally introduced supporting electrolyte for comparative purposes. Experimentally the silver macro-disc electrode was oxidized in the solution of known potassium chloride concentration with

variable potassium nitrate levels to control the ionic strength. Voltammetric peaks associated with silver chloride formation and stripping, along with other observed peaks and their waveshapes were analysed and the feasibility of detection in drinking water discussed in the light of the ionic strength of branded water.

Second, the detection of chloride using a silver electrode was undertaken in pure potassium chloride solutions and Tesco minerial water of chloride concentrations in the range 0.4 mM to 3.2 mM comparable to that in found in typical mineral waters (see Table 1). Linear correlations between the voltammetric peak current of silver chloride formation and chloride concentration were obtained.

Third, detections of chloride concentration in Tesco brand mineral water with varying added chloride concentrations were performed using a silver nanoparticles modified glassy carbon electrode via stripping voltammetry and the results compared with those from the silver macro disc electrode.

Finally, chloride detections of two real samples were performed using the calibration curve obtained in Tesco water with the silver macro disc electrode to validate the analytical procedure for the measurement of the chloride content of authentic samples of mineral waters under self-support conditions and without the addition of electrolyte or other reagents.

7.3.1 Voltammetry under 'Self-support' and 'Low support' Conditions

The voltammetric responses under 'self-support' and 'low support' conditions were analysed with a silver macro-disc electrode (**Figure 7.1**) in air-saturated solutions containing 0.4 mM KCl with 0 mM, 1.0 mM or 4.0 mM KNO_3. Each scan started from -0.50 V, swept negatively at 0.01 V s^{-1} towards -0.90 V to encompass the oxygen reduction reaction (ORR) to remove

absorbed chloride ions before detections and ensure reproducibility of measurements to avoid any need for mechanical polishing of the electrode surface as described previously.[20] Then the potential cycle reversed to +0.05 V and returned to -0.50 V.

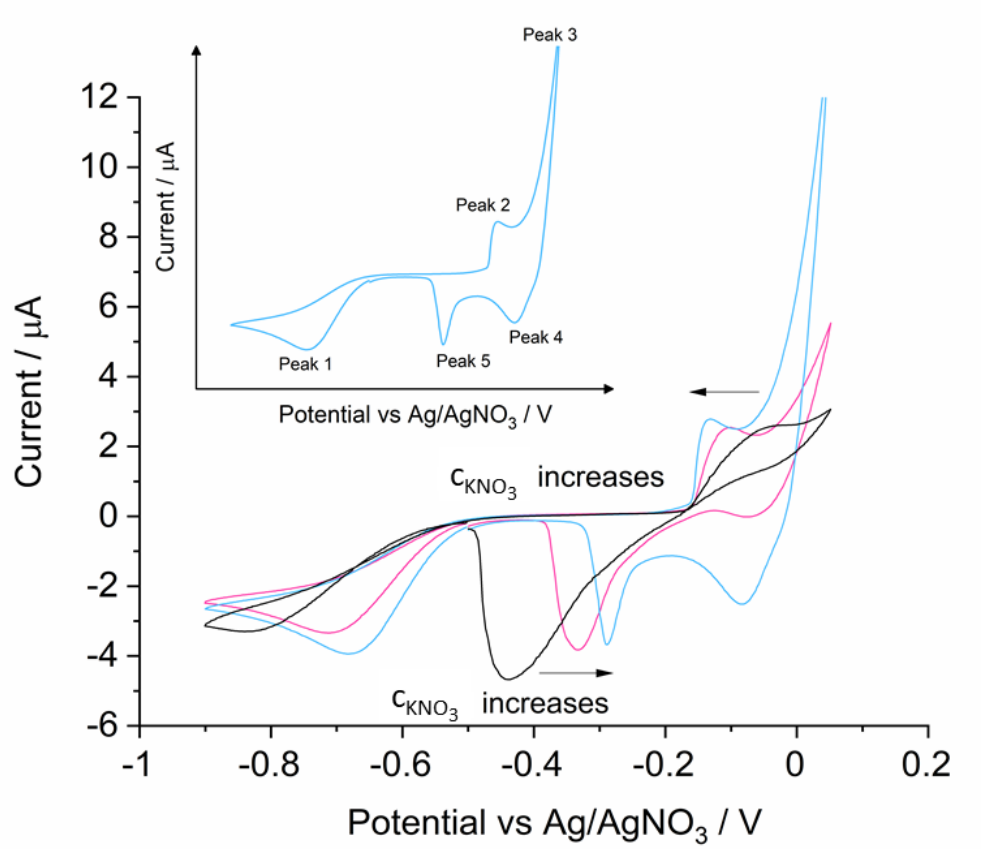


Figure 7.1 The oxidative stripping of silver macro-disc in air-saturated 0.4 mM KCl in KNO_3 solutions at a scan rate of 0.01 V s^{-1}, 298 K. The black line refers to data measured in the absence of KNO_3. The pink and blue lines refer to data with the addition of 1 mM and 4 mM KNO_3 respectively. Voltammetric peaks of interests are labelled as peak X (X = 1, 2, 3, 4 or 5) in the inset using data from the solution of 0.4 mM KCl, 4 mM KNO_3.

Five peaks can be observed in **Figure 7.1**, as labelled schematically in the inset, depending on the concentration of KNO_3 in the solution. First, the large diffusional **Peak 1** in the anodic scan corresponds to the two-electron transfer reduction of oxygen [26](**Reaction 7.2 & 7.3**). **Peak 1** was observed at -0.84 V vs $Ag/AgNO_3$ under 'self-support', which gradually shifted to a more positive potential at -0.68 V with its peak height more than doubled when 4.0 mM KNO_3 was added. The oxygen reduction on silver with 0.1 M $NaClO_4$ at 0.01 V s^{-1} was reported at -0.3 V vs SCE. by Neumann *et al.*[26] which is equivalent to -0.74 V vs $Ag/AgNO_3$. The distortion of

the ORR peak under the 'low support' condition as compared to that in the 'full support' case is expected and the low conductivity of the medium and additionally may reflect the sensitivity of the formation of peroxide to the more extended and dilute double layer.

In **Peak 2**, silver was oxidized to form silver chloride with a corresponding stripping feature (peak 5) seen on the reverse, cathodic scan. Significantly broadened peaks were observed under 'self-support' conditions regarding silver chloride formation and stripping at -0.04 V and -0.45 V respectively. In the KCl solution with 4.0 mM KNO_3, **Peak 2** and **Peak 5** shifted to -0.13 V and -0.30 V respectively and both of their shapes narrowed. The peak potentials are consistent with the values reported by De Mele *et al.*[27] in 0.09 M NaCl, 0.91 M $NaClO_4$ solution at 0.02 V s^{-1}. The formation and stripping of silver chloride on a silver electrode were seen at ca. 0.37 V and ca. 0.15 V vs NHE respectively, which are -0.11 V and -0.33 V vs the Ag/Ag^+ reference electrode used in the present study.

Peak 3 and **Peak 4** were only clearly observed in the potential range studied in 'low support' experiments under conditions where the local chloride ions were significantly depleted via conversion into AgCl in **Peak 2**. This suggests that **Peak 3** represents the onset of the silver oxidation signal leading to Ag^+ and **Peak 4** represents the Ag^+ reduction (**Equation 6.4**). The onset of the silver oxidation is consistent with the formal potential of the Ag/Ag^+ couple estimated to be 0.12 V vs the reference electrode used in this study. Comparison of the voltammograms shown in **Figure 7.1** in the absence of added electrolyte and those with low levels of support indicates a more sustained silver oxidation as the level of electrolyte support increases. Notice that when the concentration of KNO_3 increases from 0 to 4.0 mM, the continuous shift in **Peak 3** causes difficulties in the signal subtraction from the AgCl formation process, thus the stripping peak of AgCl is used in chloride determinations as reported below.

$$Ag^+_{(aq)} + e^- \rightleftharpoons Ag \;\; ; E^o = 0.8\text{V vs NHE} \qquad \textbf{(7.4)}^{24}$$

Next, the question is whether one can realistically expect to be able to apply the silver chloride stripping peak current under a certain 'support level' to quantify chloride ions in common drinking waters with varying ionic strength. The compositions of typical commercially available mineral waters were used to generate the conductivity data shown in **Table 7.2**. Estimations were made via the labelled compositions and the literature values for the equivalent molar conductivities.[28] Overall support levels in each sample are listed along with the equivalent potassium nitrate concentrations with the same conductivity. Most branded mineral waters have ionic strengths corresponding to 'low support' conditions and can be approximated as solutions with concentrations in the range of 1 mM to 4 mM KNO_3. As shown in **Figure 7.1**, the AgCl stripping peak current is almost unchanged from solutions with 1 mM to 4 mM KNO_3, suggesting, on the basis of **Table 7.2**, similar voltammetric parameters can permit direct measurements in most drinking waters, though dilutions to reach this range are required in (surprisingly) high salt mineral waters such as Borjomi and Varska waters.

Table 7.2 Conductivities (298 K) and equivalent KNO_3 concentrations in common drinking waters[6, 7]

	Conductivity uS cm^{-1}		**Equivalent KNO_3 concentration/ mM [ii]**	
Mineral waters				
Highland Spring	313[iii]	336[29] [iv]	2.16	2.32
Evian	442 [ii]	600 [v]	3.05	4.14
Tesco	159 [ii]		1.10	
Aqua Pura	218 [ii]		1.50	

[ii] Equivalent KNO_3 concentrations were calculated according to KNO_3 solutions with the same conductivity value. The concentration values in the first column corresponding to the conductivity values in the first column, and so for the second column.

[iii] Conductivity values estimated from compositions labelled on the mineral water package via equation $\Lambda_{total} = \sum_i \nu_i \cdot n_i \Lambda_i$ where ν_i, n_i, $\Lambda_i$refer to the number of charges, the moles, and the equivalent ionic conductivity of species i respectively. The ionic conductivity values are obtained from the literature.28.D. R. Lide, *CRC Handbook of Chemistry and Physics, 86th Edition*, Taylor & Francis, 2005.

[iv] Conductivity values are measured in other literatures.29. A. Alsulaili, M. Al-Harbi and K. Al-Tawari, *Journal of Engineering Research*, 2015, **3**, 2.

[v] Conductivity values are provided in manufacture annual reports.

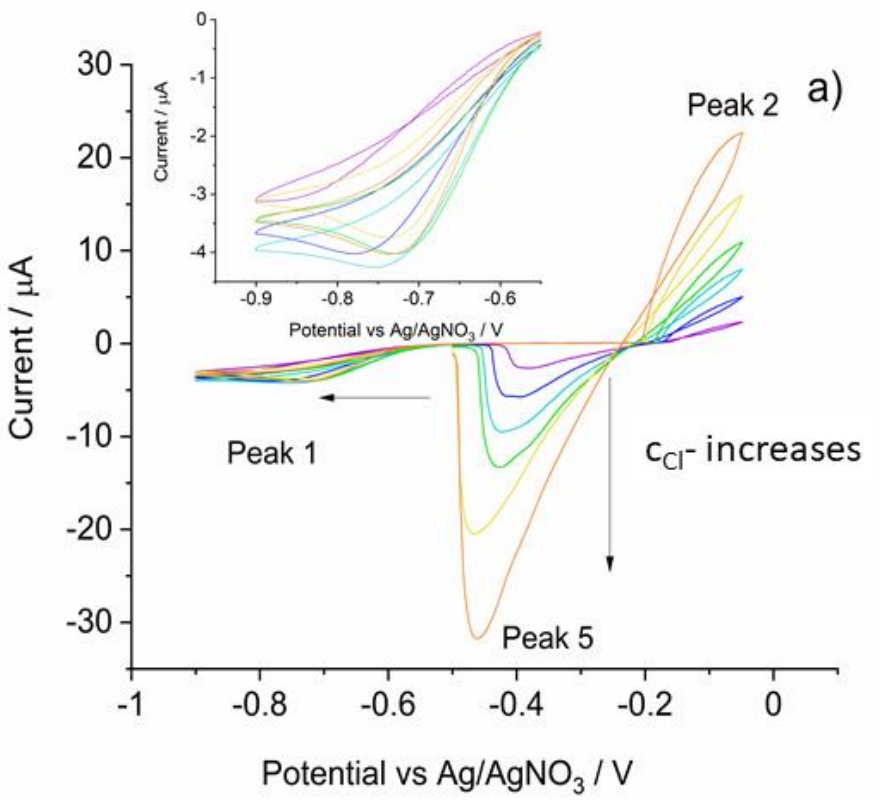
Table 7.2 continued				
Volvic	218 [ii]	220 [iii]	1.50	1.52
Nestle Pure Life	437 [ii]	160-960 [iii]	3.01	1.10-6.63
Buxton	582 [ii]		4.02	
Natural Mineral waters				
Voluvesi	596[6]		4.11	
Saaremaa Vesi	588 [6]		4.06	
Saku	175 [6]		1.21	
Borjomi Sparkling	4114 [ii]		52.27	
Varska	2130 [6]		14.70	
Varska original	4370 [6]		30.16	

7.3.2 Chloride Determination in Pure KCl Solutions and Tesco Mineral Water KCl Solutions (Tesco-KCl Solutions)

To develop the sensor for use in mineral water samples which contain additional ions such as sulfate and carbonate, Tesco mineral water was used to prepare a series of standard solutions spiked with different amounts of KCl so as the create a calibration curve based on the voltammetric method developed in the **Section 7.3.1** above. This was first applied in pure KCl solution and results were used for comparison with Tesco-KCl solutions at the same chloride level.

The electroanalytical responses of the silver/ silver chloride stripping signal measured at a scan rate of 0.01 V s^{-1} were explored in air-saturated pure KCl solutions and Tesco–KCl solutions with chloride concentration ranges from 0.4 mM to 3.2 mM. Figure 2 shows the voltammograms which consist of oxygen reduction (to activate the electrode and ensure reproducibility of the analytical signal) and silver chloride deposition/reduction, scanned from -0.50 V to -0.90 V then scanned positively to -0.05 V and finally swept back to -0.50 V. Three peaks (**Peak 1**, **Peak 2** and **Peak 5** as indicated in **Figure 7.2**) were observed for each scan in all the concentration range studied.

First, the ORR signals (**Peak 1**) in pure KCl solutions were compared to those in Tesco-KCl solutions. In the former medium in the concentration range 0.4 mM to 0.8 mM KCl solution, the peroxide feature shifted from -0.85 V to ca. -0.75 V and the peak current increased from 3 µA to 4 µA, reflecting the increased ionic concentration. In contrast, the ORR signal in Tesco-KCl water was fixed at ca. -0.70 V plausibly due to the higher conductivity in the mineral water. As the ORR signal reflects more the ionic strength instead of the real chloride levels in the solution, it has little analytical value in the present study beyond and very importantly creating a reproducible surface for silver chloride formation and stripping.



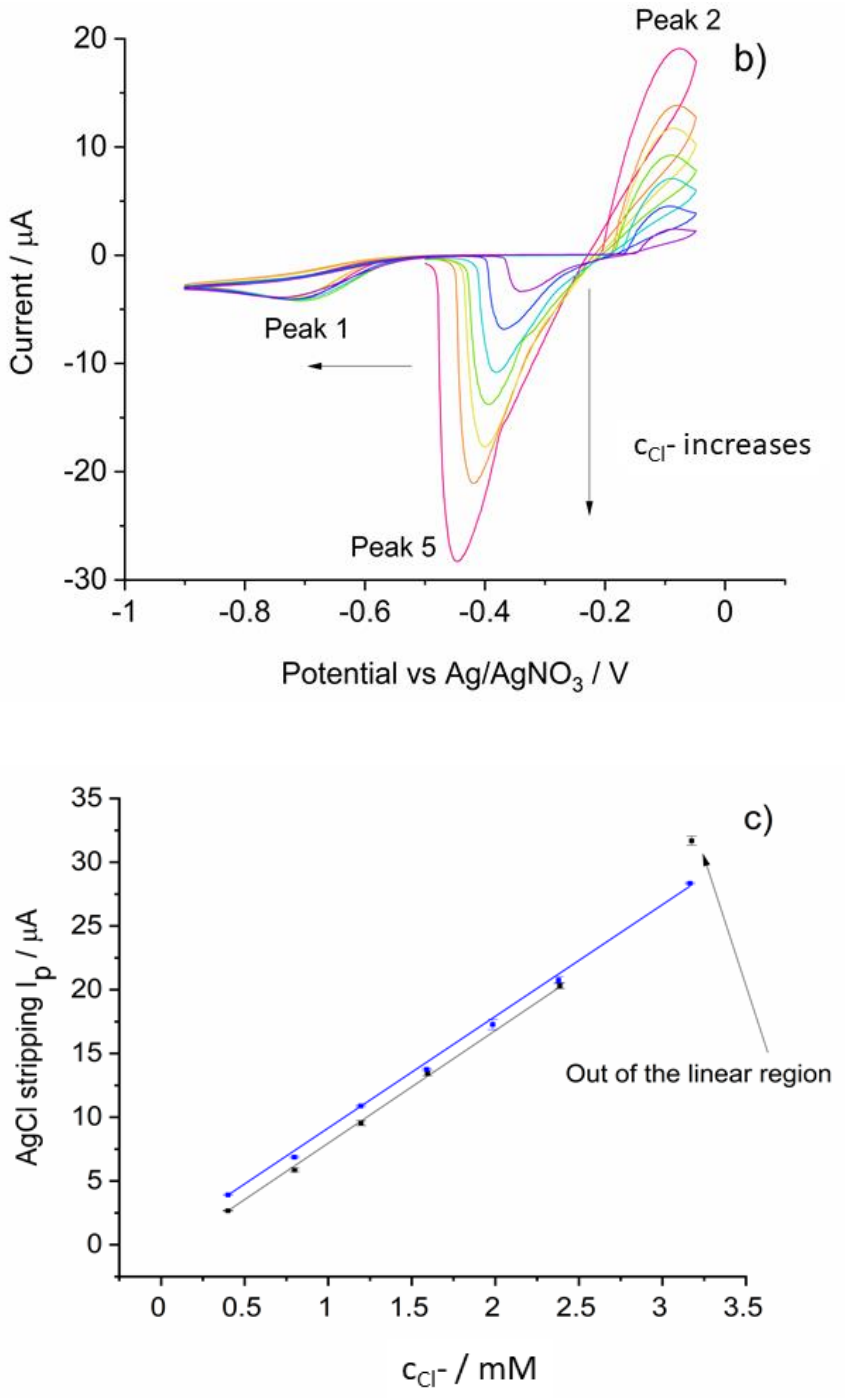


Figure 7.2 The oxidative stripping voltammetry of silver macro-disc electrode at 0.01 V s^{-1}, 298 K in air-saturated solutions. a) Pure KCl solutions of 0.4 mM, 0.8 mM, 1.2 mM, 1.6 mM, 2.4 mM and 3.2 mM. Chloride concentrations increase as indicated by the arrow. b) Tesco-KCl solutions of 0.4 mM, 0.8 mM, 1.2 mM, 1.6 mM, 2.0 mM, 2.4 mM and 3.2 mM supplementing the chloride present in Tesco water which contributes 0.4 mM. Chloride concentrations increased as indicated by the arrow. c) The calibration curves were determined with the silver chloride stripping peak currents. Data in blue shows results from Tesco-KCl solutions, data in black shows results from pure KCl solutions. Each data contains three repeats. The regression coefficient for pure KCl solution and Tesco-KCl solution are both 0.999. The high concentration point is discussed in the text.

Next, silver chloride formation signals (**Peak 2**) were analysed. In pure KCl solutions due to the extreme low ionic strength, the peaks were broad and the current steadily increased within the potential range studies creating a voltammetric 'loop' to be was observed with the highest current at -0.05 V. In the Tesco-KCl solutions, clear silver chloride formation peaks were observed at -0.1 V. In both cases the formation peak currents increased as the chloride concentration increased.

On the cathodic scan, silver chloride stripping peaks (**Peak 5**) were observed during the reverse scans for both pure KCl and Tesco-KCl solutions. As more silver chloride formed on the electrode surface, the peak shifted to more negative potentials and its height increased. Linear relationships were observed between AgCl stripping peak currents and chloride concentrations (**Figure 7.2 c**) for both solutions. The correlation ranges were 0.4 mM to 2.4 mM and 0.4 mM to 3.2 mM for pure KCl solutions and Tesco- KCl solutions respectively with the different intercepts reflecting the different amounts of AgCl formation within the potential window. The extreme data point of 3.2 mM KCl solution deviated from linearity likely due to the increased ionic strength. Most importantly, the calibration curve slope in pure KCl solutions is 8.99 μA mM^{-1}, almost identical to that in Tesco- KCl solutions (8.76 μA mM^{-1}), indicating that the detection sensitivity is not affected by mineral water interferences, validating the use of Tesco mineral water as the solvent in the following sections.

7.3.3 Chloride Determinations in Tesco-KCl Solutions Using Silver Nanoparticle Modified Electrodes

Meanwhile, the analytical methodology developed above with bulk silver was compared to that using silver nanoparticles (AgNPs) seeking enhanced mass transport under low support systems. The oxidative stripping voltammetry was performed in nitrogen saturated Tesco-KCl

solutions with chloride concentrations from 0.4 mM to 3.2 mM on AgNPs modified glassy carbon electrode (GC). The voltammetry started from -0.70 V, scanned positively at 0.1 V s^{-1} to 0.50 V and reversed to -0.70 V.

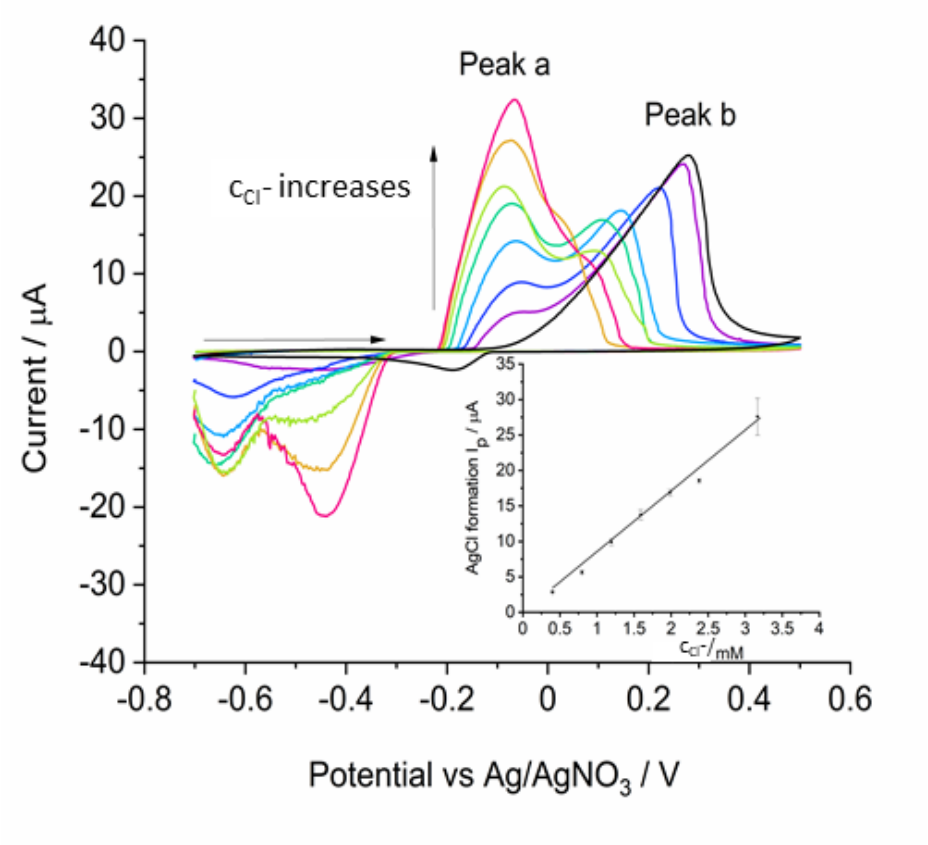


Figure 7.3 The oxidative stripping of AgNPs from a GC electrode at a scan rate of 0.01 V s^{-1}, 298 K in N_2 saturated Tesco-KCl solutions. The blank experiment was performed in 1 mM KNO_3 (black); Chloride detections were performed in Tesco-KCl solutions of 0.4 mM, 0.8 mM, 1.2 mM, 1.6 mM, 2.0 mM, 2.4 mM and 3.2 mM supplementing the chloride present in Tesco water which contributes a further 0.4 mM. Chloride concentrations increase as indicated by the arrow. The inset shows the calibration curve where chloride in Tesco water has also been counted. Each point contains three repeats. Regression coefficient R^2 =0.995

Two broad peaks were observed in the oxidative scan in chloride solutions. As shown in **Figure 7.3**, **Peak a** was observed at -0.10 V, partially overlapping with peak b at a higher potential between 0.05 V and 0.25 V. With a constant amount of AgNPs modified on the electrode, **Peak a** increased in magnitude as the chloride concentration increased in contrast to **Peak b** which

current was gradually decreased and potential shifted to a lower value. A further experiment was performed in 1 mM KNO_3 to exclude the presence of chloride and which has a conductivity identical to that of the Tesco mineral water (see **Table 7.2**). As only **Peak b** was observed in the blank data, **Peak a** possibly correlates to the formation of AgCl whilst **Peak b** is associated with the oxidation of the AgNPs to Ag^+. Similar observations were reported by Toh *et al.*[19] who performed the stripping of AgNPs modified GC in 'full support' conditions using 0.1 M $NaNO_3$ solution with an addition of 2 mM to 40 mM KCl content. Two broad peaks were seen each at -0.2 V (**Peak a**) and 0.2 V (**Peak b**) vs $Ag/AgNO_3$ for the silver chloride formation and the silver cations formation respectively. Compared to results reported in 'full support' conditions, both peaks shifted to more positive potentials in this study probably due to the low ionic strength.

A linear correlation was observed between the current of **Peak a** and the concentration of chloride ions with a slope of 8.57 µA mM^{-1}, which is comparable to that observed with the silver macro disc electrode (8.76 µA mM^{-1}). With sufficient silver deposited (27.8 nmol of Ag) to ensure the sensitivity with AgNPs[19], the similarity in slopes indicates that the reaction of AgCl formation is chloride concentration limited, and the use of a silver macro disc electrode can achieve the same sensitivity as with AgNPs; the analytical signal is controlled in both cases by the diffusion of the chloride to the geometric area of the electrode, either pure silver or the silver nanoparticle modified glassy carbon electrode. Accordingly, the use of the silver electrode was adopted preferentially for reasons of simplicity and speed. In this manner chloride concentrations in real samples were estimated on a bulk silver electrode using the calibration curve evaluated from Tesco-KCl solutions as reported in the next section.

7.3.4 Chloride Determination in Real Samples

To evaluate the feasibility for practical chloride detections in mineral waters, two real samples were tested against the system. Sample 1 was Volvic water used directly as purchased, sample 2 was Borjomi sparkling water which has an unusually high mineral content (and taste!), hence prior to analysis this was diluted with deionized water by a factor of ten after all gases were released. The dilution was essential for the Borjomi water as first, its original chloride concentration was 10.7 mM, beyond the linear sensing range of 0.4 mM to 3.2 mM and second, its conductivity equivalent to 52.3 mM KNO_3 which is far above 'low support' levels so differs from the conditions applied in the construction of the calibration curve. The test with the diluted Borjomi water extended the application of the developed chloride determination methodology from regular to the very highest mineral level drinks.

A cyclic voltammogram was recorded from −0.50 V to -0.90 V before sweeping positively to -0.05 V and returned to -0.50 V at a scan rate of 0.01 V s^{-1}. Each experiment was repeated three times. **Figure 7.4** shows the voltammograms recorded from the mineral water samples. Three peaks were observed. First, the ORR feature (**Peak 1**) was seen at -0.75 V and -0.70 V for sample 1 and 2 respectively, reflecting the conductivity increased from 218 uS cm^{-1} to 411 uS cm^{-1} (recall **Table 7.2**). Second, **Peak 2** was observed at -0.12 V and -0.15V corresponding to the silver chloride formation in sample 1 and sample 2, followed by the generation of Ag^+ at -0.05 V. Finally, silver chloride was removed in the reversed scan, for each solution, a shoulder was observed at ca. -0.32 V before the main peak appeared at ca. -0.36 V. The shoulder in silver chloride stripping peak has been reported[20, 30, 31], possibly reflecting instantaneous AgCl nucleation or silver dissolution.

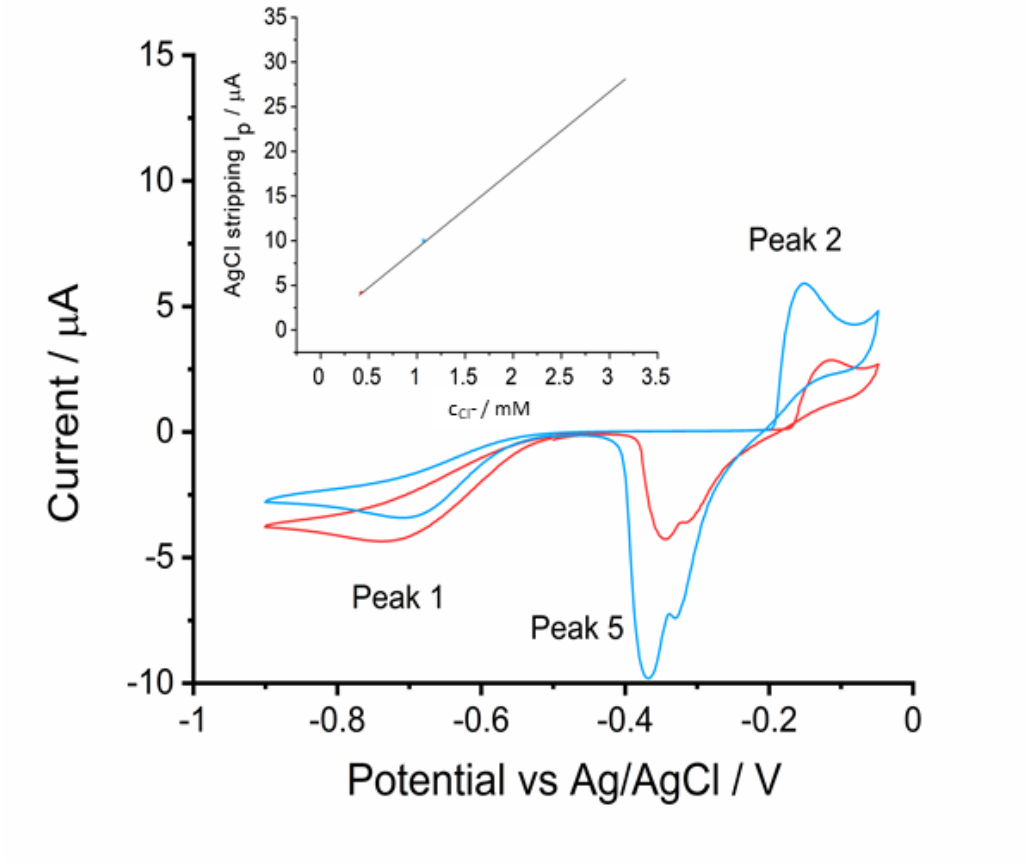


Figure 7.4 Chloride determinations in real mineral water samples at 0.01 V s^{-1}. Red: Volvic water; blue: Borjomi sparkling water diluted with deionized water by a factor of ten. Inset shows the chloride concentration estimated with the calibration curve generated in Tesco-KCl solutions. Each point represents three repeats.

By measuring the current in **Peak 5**, the chloride concentration in samples was estimated. The experimentally measured values were 0.44 ± 0.01 mM and 1.10 ± 0.02 mM for Volvic water and 1/10 Borjomi mineral water respectively and the corresponding manufacturer reported chloride concentrations were 0.42 mM (Volvic) and 1.07 mM (Borjomi). The inset of **Figure 7.4** displays the samples at the expected chloride concentration, showing the measured chloride concentration in examined samples fitted well to the expected values. In this way, the developed method was validated and applied to authentic mineral waters.

7.4 Conclusions

This chapter presents a facile chloride detection method for mineral water samples and was specifically developed for low ionic strength solutions. The method utilizes the peak current of the AgCl stripping process on a silver macro disc electrode over a well-defined potential range as a measure of chloride concentrations while applying the ORR reaction to activate the electrode surface so that reproducible measurements can be realised without mechanical cleaning. The method was validated with chloride ions quantifications in Volvic mineral water and Borjomi sparkling mineral water where results were in agreement with mineral water labelled compositions. More generally quantitative electroanalytical measurements were realised using a macro-electrode under conditions of low electrolyte support so allowing reagent free analysis and the use of conventional voltammetry.

Compared to commercialised techniques that quantify ions in mineral water eg. titration and chromatography, this particular electrochemistry method is fast, low cost and non-toxic. The required sample volume is minimized and can be reused for other composition detection. Moreover, the deposition/stripping methodology can be optimized to distinguish and determine the concentration of bromide and iodide instantaneously.[18] Towards the realisation of such a simple chloride testing system, future experiments regarding interference study are essential. Ions of interest include other halides and, in particular, sulfate which are likely to present as major composition (>200mg L^{-1}) when testing natural high mineral content waters. Furthermore, the use of bulk silver electrodes can be replaced with a disposable print electrode chip as previously reported by Toh *et al.*[19] in which way the preparation and test procedures are largely simplified for end users.

Bibliography

1. Y. Guo and R. G. Compton, *Analyst*, 2021, **146**, 4700-4707.
2. J. D. Hem, *Study and interpretation of the chemical characteristics of natural water*, Report 2254, Reston, VA, 1985.
3. L. McCallum, S. Lip and S. Padmanabhan, *Pflugers Arch*, 2015, **467**, 595-603.
4. World Health Organization, *Guidelines for drinking-water quality*, World Health Organization, Geneva, 4th edn., 2011.
5. S. Quattrini, B. Pampaloni and M. L. Brandi, *Clin Cases Miner Bone Metab*, 2016, **13**, 173-180.
6. L. Bityukova and V. Petersell, *J. Geochem. Explor.*, 2010, **107**, 238-244.
7. V. Gvakharia, A. Jgamadze, J. Gabechava, T. Adamia, D. Chkhaidze, T. Jebashvili, D. Sozashvili, B. Lebanidze and A. Maglakelidze, *Ann. Agrar. Sci.*, 2018, **16**, 27-31.
8. E. Dinelli, A. Lima, S. Albanese, M. Birke, D. Cicchella, L. Giaccio, P. Valera and B. De Vivo, *J. Geochem. Explor.*, 2012, **112**, 368-389.
9. WHO, *Journal*, 2011.
10. L. S. Clesceri, A. E. Greenberg and A. D. Eaton, *Standard Methods for the Examination of Water and Wastewate*, APHA American Public Health Association, USA, 20th edn., 1998.
11. *Department of the Environment*, *Chloride in waters, sewage, and effluents* H.M.S.O., London, 1982.
12. P. Quevauviller and K. C. Thompson, 2006.
13. B. Amra; and O. Amra;, ed. D. E. Ekundayo, 2011.
14. W. Holiczer, *Coulometric method of the chloride ion concentration measurement: mathematical model of the measuring transducer and its experimental verification*, SPIE, 2001.
15. K. Arai, F. Kusu, N. Noguchi, K. Takamura and H. Osawa, *Anal. Biochem.*, 1996, **240**, 109-113.
16. J. Bujes-Garrido, D. Izquierdo-Bote, A. Heras, A. Colina and M. J. Arcos-Martínez, *Anal. Chim. Acta*, 2018, **1012**, 42-48.
17. A. Gupta, M. Maynes and S. Silver, *Appl. Environ. Microbiol.*, 1998, **64**, 5042-5045.
18. X. Qin, H. Wang, Z. Miao, X. Wang, Y. Fang, Q. Chen and X. Shao, *Talanta*, 2011, **84**, 673-678.
19. H. S. Toh, C. Batchelor-McAuley, K. Tschulik and R. G. Compton, *Analyst*, 2013, **138**, 4292-4297.
20. Y. Guo and R. G. Compton, *Talanta*, 2021, **232**.
21. X. Li, C. Batchelor-McAuley, E. Laborda and R. G. Compton, *Chem. Eur. J*, 2017, **23**, 15222-15226.
22. K. Ngamchuea, C. Batchelor-McAuley and R. G. Compton, *J. Electroanal. Chem.*, 2018, **830-831**, 122-130.
23. Y. Guo, M. Yang, C. Batchelor-McAuley and R. G. Compton, *J. Electroanal. Chem.*, 2019, **849**, 113370.
24. A. J. Bard, R. Parsons, J. Jordan, P. International Union of and C. Applied, *Standard potentials in aqueous solution*, M. Dekker, New York, 1985.
25. Y. J. Guo, M. J. Yang, R. C. Xie and R. G. Compton, *Chem. Sci.*, 2021, **12**, 397-406.
26. C. C. M. Neumann, E. Laborda, K. Tschulik, K. R. Ward and R. G. Compton, *Nano Res.*, 2013, **6**, 511-524.
27. M. F. L. de Mele, R. C. Salvarezza, V. D. Vasquez Moll, H. A. Videla and A. J. Arvia, *J. Electrochem. Soc.* , 1986, **133**, 746-752.
28. D. R. Lide, *CRC Handbook of Chemistry and Physics, 86th Edition*, Taylor & Francis, 2005.
29. A. Alsulaili, M. Al-Harbi and K. Al-Tawari, *Journal of Engineering Research*, 2015, **3**, 2.
30. F. Pargar, H. Kolev, D. A. Koleva and K. van Breugel, *J. Mater. Sci.*, 2018, **53**, 7527-7550.
31. V. I. Birss and C. K. Smith, *Electrochim. Acta.*, 1987, **32**, 259-268.

Chapter 8

Conclusions

Electrochemical analysis in natural aqueous media benefits the development of applications from sensors to fuel cells. The complexity in compositions and the wide range of ionic contents levels are particularly challenging within current technique constraints. This thesis has investigated how voltammetric responses in extremely high or low ionic conductivity media can be applied to detect chloride ions in those conditions simple and fast, so going beyond the usual boundaries of electrochemical methodology.

For seawater or similar chloride media, the mechanistic study of the oxygen reduction towards peroxide on a silver macrodisc electrode revealed a 2 step reaction with the quasi reversible formation of superoxide ions. The observation of a voltammetric superoxide peak signalled the local escape of superoxide in contrast to what is seen in the reduction of oxygen in most media and at most electrodes. This difference was tentatively ascribed to chloride adsorption on the silver surface which is significant at chloride concentrations above 0.5 M. The distinct emerge of superoxide peak indicates the possible enhancement of nanotoxicity effects due to superoxide formation in seawater where silver nanoparticles are present in marine environments.

Next, the distinct oxygen reduction signals are applied in the development of a simple and direct chloride detection system, specially designed for the narrow range in high chloride levels (ca. 0.5 M) in natural seawater. The method utilises the peak current during the growth of silver chloride on a bulk silver electrode which linearly correlated to chloride concentration within the seawater chloride range. Particularly, the prior ORR sweep provided both a quasi-reference

electrode and reproducible electrode surface without mechanical polishing for facile measurements.

In contrast to seawater samples analysed above, in low conductivity media where the migration effect becomes significant and voltammetric peaks distorted, the analytical use of voltammetry becomes challenged with little work previously attempted on stripping voltammetry in weakly supported media. The deposition and stripping voltammetry was studied in the presence and absence of additional supporting electrolytes and investigated both theoretically and experimentally. **First**, the theory was developed using the zero-field approximation to avoid overestimations of the electrical double layer effect thus the results solely reflects charge separation during the electrochemical process. When the Debye length of the system is comparable to the electrode radii (a large x_{DL}/r ratio), the migration effect vanishes and the mass transport flux is diffusional controlled. Measurements in such conditions may be experimentally possible under low support conditions with no need for nanoscopic electrodes. Second, experimental validations were performed via silver deposition and stripping voltammetry. Meanwhile, limitations to the developed model were also observed particularly due to changes in the silver nucleation rate but also the difference between the hemispherical geometry in simulation as opposed to a disc electrode one in experiments. Possible future work with 2D models and optimization of voltammetric methods (scan rates and pre-concentration) may be helpful.

Last but not least, a bespoke chloride detection method for application in mineral water samples was specifically developed using a silver electrode for low ionic strength solutions. Likes its counterpart built for seawater, the method embraces prior ORR sweep to the active silver electrode surface followed by silver deposition/stripping reaction, but in an optimized potential range. The silver chloride stripping peak current

correlated linearly to the chloride concentration which calibration curve was validated with real samples. Thus, the reagent free analysis with cyclic voltammetry on a simple macrodisc electrode was achieved.

The above findings in natural aqueous solutions open up electrochemical analysis under extreme support levels without hazardous or expensive reagents and provide physiochemical insights for both electrochemical applications consider realistic ionic complexities such as seawater fuel cell and fundamental studies.

Appendix A

Section 1 Calibration of Electrodes

Electrode radii were confirmed using cyclic voltammetry at variable scan rates from 0.02 V s^{-1} to 0.4 V s^{-1} at 298 K in nitrogen degassed solutions of 0.1 M potassium chloride and 1 mM hexaammineruthenium(III) chloride using the fully electrochemically reversible version Randles–Ševčík equation, where the variation of the peak current (I_p) with the square root of the scan rate (v):

$$I_p = 2.69 \times 10^5 n\, A D_{O_2}{}^{0.5} c_{O_2} v^{0.5} \qquad \textbf{(A.1)}$$

Where n = 1, $c_{O_2} = 1.0$ mol m^{-3},$D_{O_2} = 8.4 \times 10^{-10}$ $m^2 s^{-1}$. [1]

The term $2.69 \times 10^5 n\, A D_{O_2}{}^{0.5} c_{O_2}$ was calculated from the slope of the inlay in **Figure A.1a** and **b**, giving radii of the silver electrode (1.36 mm) and the glassy carbon electrode (1.49 mm)

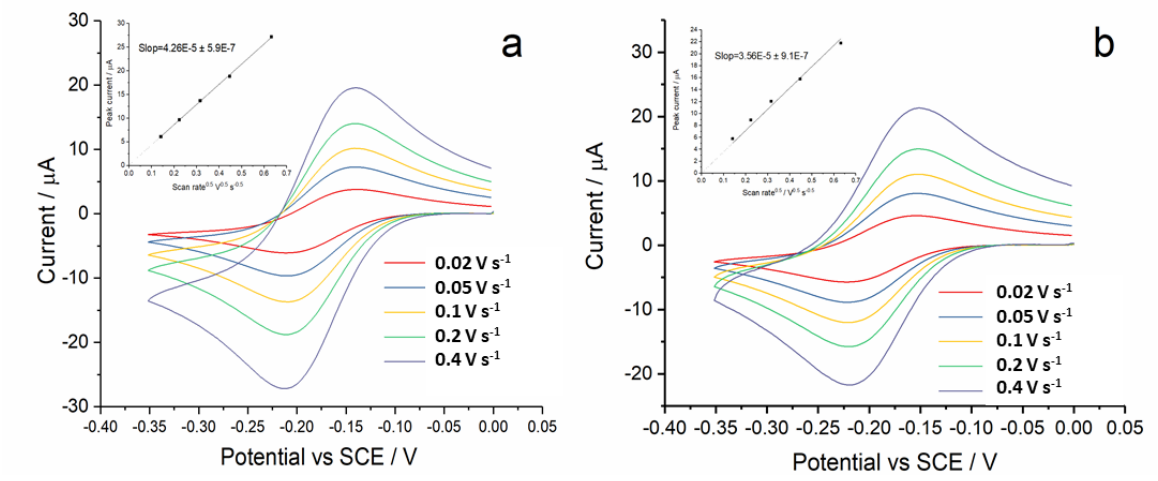


Figure A.1 Calibration of electrodes a) GC, r=1.49 mm, Technical, UK) and b) Ag, homemade, r =1.36 mm.

The measured diameter of GC electrode is 2.97±0.05 mm which is in agreement with electrochemical results, however the measured diameter of Ag electrode (1.98±0.01 mm) is much smaller than that obtained from **Figure A.1b**, possibly due to chloride adsorption on the silver surface.

Section 2 Seawater Composition, Oxygen Solubilities and Diffusion Coefficients

Table A.1 Chemical compositions of synthetic seawater[2, 3] and authentic seawater[4]

Composition	Simple synthetic seawater / mol L^{-1}	Standard synthetic seawater / mol L^{-1}	Standard authentic seawater / mol L^{-1}
Na^+	4.20E-01	4.80E-01	4.69E-01
K^+	9.39E-03	1.02E-02	1.02E-02
Mg^{2+}	5.46E-02	5.46E-02	5.28E-02
Ca^{2+}		1.05E-02	1.03E-02
Sr^{2+}		6.40E-05	9.10E-05
Cl^-	5.39E-01	5.60E-01	5.46E-01
SO_4^{2-}		2.88E-02	2.82E-02
HCO_3^-		2.38E-03	1.72E-03
CO_3^{2-}			2.39E-04
Br^-		8.40E-04	8.42E-04
F^-		7.20E-05	6.80E-05
H_3BO_3		4.90E-05	
$B(OH)_4^-$			1.01E-04
$B(OH)_3$			3.14E-04
OH^-			8.00E-06
CO_2			1.00E-05

Table A.2 Reported diffusion coefficients of oxygen in various solutions.

D_{O_2} ($\times 10^{-9}$) / m^2 s^{-1}	Solution
2.42 [5-7]	H_2O [vi]
1.98 [8]	H_2O [vii]
3.40 [9]	H_2O [vi]
2.26 [10]	H_2O [vi]
1.96 [11]	H_2O [vi]
1.7 [12]	Britton-Robinson buffer solution containing 0.1 M NaCl [vi]
1.9 [63]	0.01M Na_2SO_4 aq [vii]
1.46 [8]	0.552M NaCl aq. [vii]
2.08 [9]	0.5M NaCl aq. [vi]
2.17 [10]	0.5642M NaCl aq. [vi]
1.4 [13]	Seawater [vi]
2.3 [14, 15]	Seawater [viii]
1.26 [16]	0.5M H_2SO_4 aq. [vi]
1.93 [17, 18]	0.1M NaOH aq. [vi]

Table A.3 Reported diffusion coefficients of oxygen in different NaCl concentration aqueous solutions

Literature value reported by	NaCl concentration in M	D_{O_2} ($\times 10^{-9}$) / m^2 s^{-1}
Stroe *et al.* [10 *ix*]	0	2.26
	0.0846	2.2
	0.154	2.22
	0.282	2.21
	0.4231	2.12
	0.5642	2.17
Ju *et al.* [19 *x*]	0	2.08
	0.2	1.80
	0.5	1.60
Jamnongwong *et al.* [8 *xi*]	0	1.98
	0.103	1.44
	0.552	1.46

vi Data obtained for solution at 298 K.
vii Data obtained for solution at 293 K.
viii Data obtained for solution at 297 K.
[ix] Data obtained at 298 K
[x] Data obtained at 295 K
[xi] Data obtained at 293 K

Table A.4 Literature solubility of O_2 in various solutions.

Solubility in mM	Solution
1.15 [20]	H_2O [xii]
1.01[20]	H_2O [xii]
1.26 [21]	H_2O [ix]
1.25 [12]	Britton-Robinson buffer solution containing 0.1 M NaCl[ix]
0.23 [20]	5M NaCl aq.[ix]
1.28 [22]	1mM H_2SO_4 aq.[ix]
1.25 [23]	0.5M H_2SO_4 aq.[ix]
1.43 [16]	0.5M H_2SO_4 aq.[ix]

Table S5. Literature solubility of O_2 in solution with varied salinity at 298 K.

Solubility in mM	Solution
0.2591[20 xiii]	H_2O
0.2791 [20 xii]	H_2O
0.2598 [20 xii]	H_2O
0.2631 [20 xii]	H_2O
1.26 [21 xiv]	20mM KCl aq.
1.25 [12 xiv]	Britton-Robinson buffer solution containing 0.1 M NaCl
1.24 [24 xv]	0.1 M NaCl aq.
1.07 [24 xv]	0.42 M NaCl aq.
1.01 [24 xv]	0.54 M NaCl aq.
0.2508 [20 xiv]	Seawater Salinity = 7.816 g kg^{-1}
0.2350 [20 xiv]	Seawater Salinity = 18.985 g kg^{-1}
0.2226 [20 xiv]	Seawater Salinity = 28.986 g kg^{-1}
0.2054 [20 xiv]	Seawater Salinity = 35.77 g kg^{-1}
0.2096 [20 xiv]	Seawater Salinity = 38.792 g kg^{-1}

[xii] Data obtained at 303 K
[xiii] Data obtained with air saturated solutions
[xiv] Data obtained with oxygen saturated solutions
[xv] Data obtained from Figure 8 in reference cited

Section 3 Oxygen Reduction Reaction on Silver Electrode in KNO_3 and $NaClO_4$

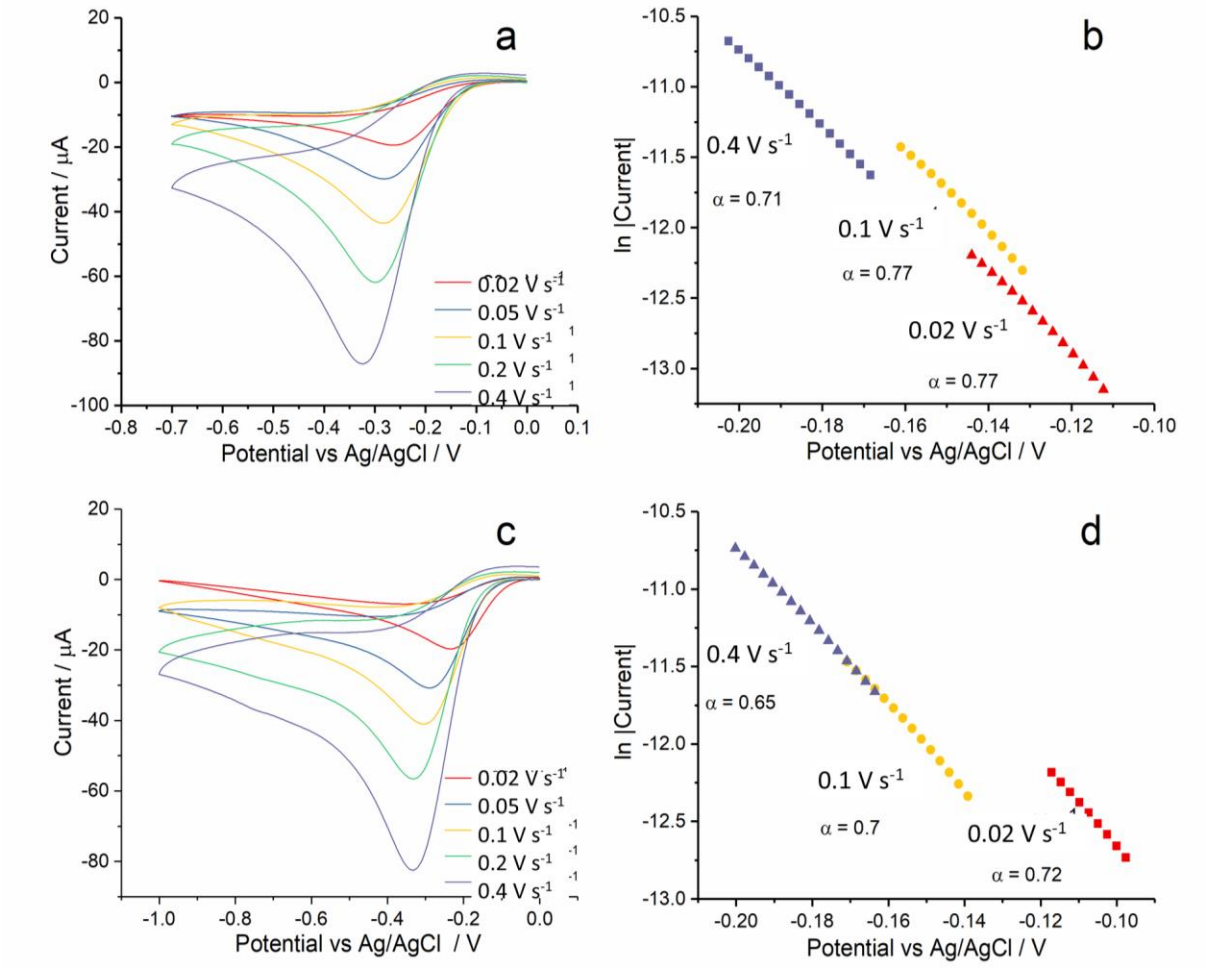


Figure A.2 Reductive voltammetry studies on a silver macroelectrode. a) Voltammagrams in oxygen saturated 0.1 M KNO_3 with varying scan rates from 0.02 V s^{-1} to 0.4 V s^{-1} and Tafel analysis in b); c)Voltammagrams in oxygen saturated 0.1 M $NaClO_4$ with varying scan rates from 0.02 V s^{-1} to 0.4 V s^{-1} and Tafel analysis in d)

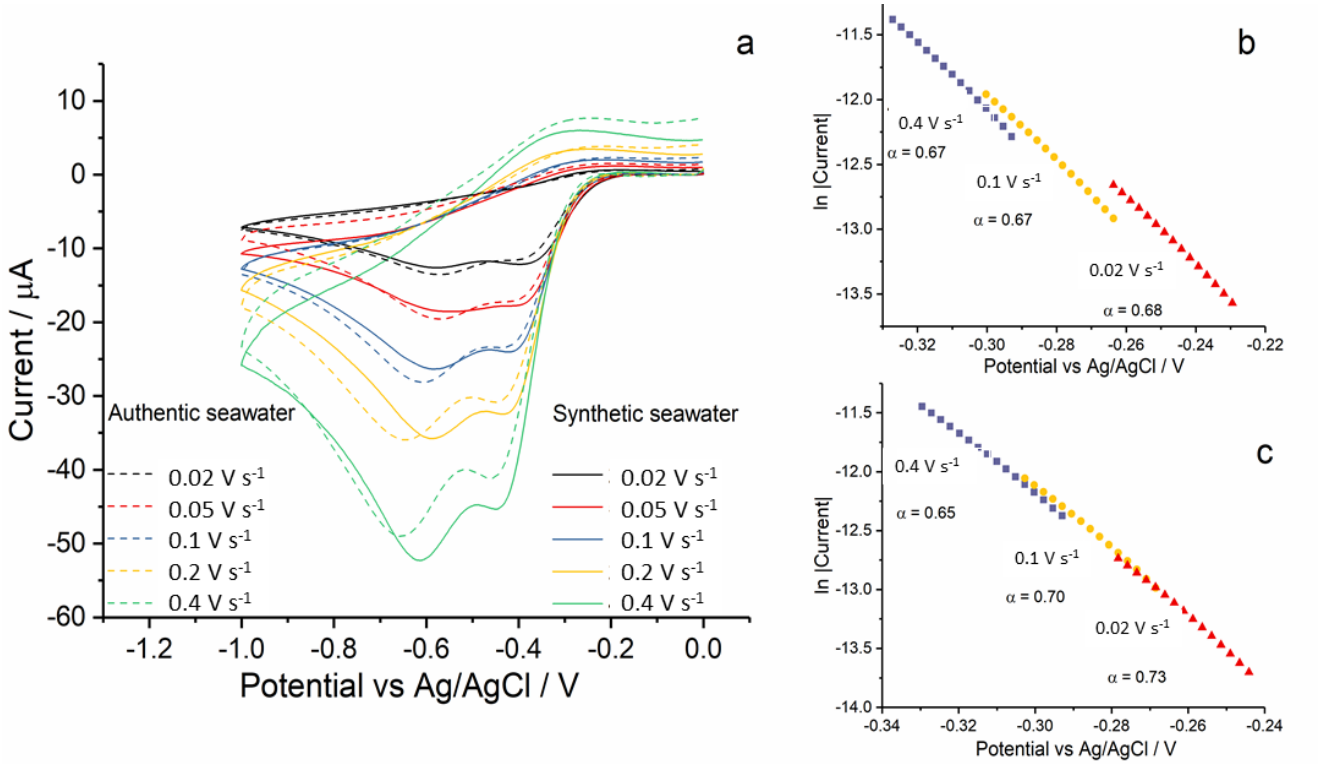


Figure A.3 O_2 reduction in seawater on silver electrode a) Voltammagrams in synthetic seawater (solid line) and authentic seawater (dash line) with varying scan rates from 0.02 V s^{-1} to 0.4 V s^{-1} b) Tafel analysis in authentic seawater and c) Tafel analysis in synthetic seawater

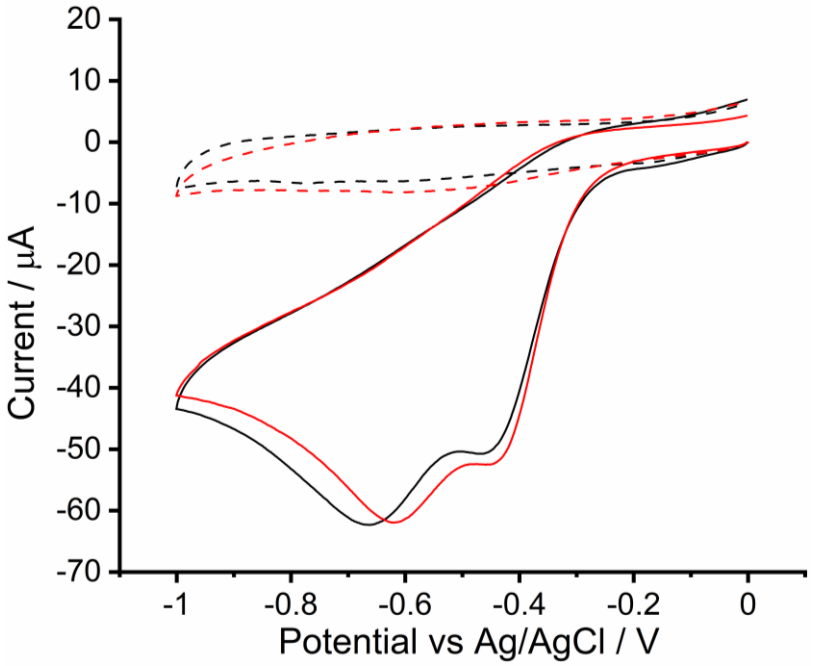


Figure A.4 Cyclic voltammetry in O_2 saturated (solid line) overlaid with that in N_2 saturated (dash line) solutions. Measurements were performed in synthetic seawater (red) and authentic seawater (black) at 0.4 V s^{-1} on the silver macrodisc electrode.

Section 5: Digisim Fitting of Oxygen Reduction Reaction on Silver in Synthetic Seawater

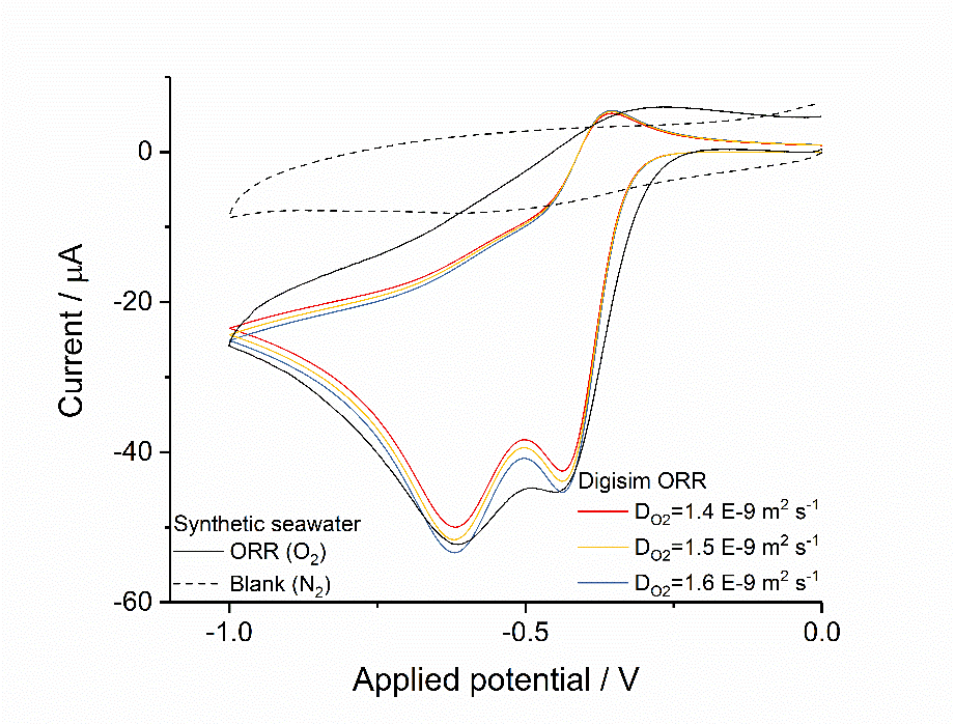


Figure A.5 Digisim analysis of ORR in seawater. The effect of diffusion coefficient and background (experiment in nitrogen saturated seawater) at 0.4 V s^{-1}.

Table A.6 Electron transfer kinetics of the oxygen reduction at bulk silver at 298 K in synthetic seawater. [xvi]

Step 1		**Step 2**	
$\boldsymbol{A + e^- \rightarrow B}$ (quasi-reversible)		$B + e^- \rightarrow P$ (irreversible)	
$\boldsymbol{C_{O_2}}$=1.1 mM		$\boldsymbol{C_{O_2}}$=1.1 mM	
$\boldsymbol{D_{O_2}}$=1.6×10^{-9} m^{2}s^{-1}		$\boldsymbol{D_{O_2}}$=1.6×10^{-9} m^{2}s^{-1}	
$\boldsymbol{\alpha}$	0.5	$k = k_0 \exp\left(\frac{\alpha E_f^0 F}{RT}\right)$ cm s^{-1}	$4.9 \pm 1.8 \times 10^{-11}$
k_0 / cm s^{-1}	1.0		
$\boldsymbol{E_f^0}$ / V	-0.4		

[xvi] k_0 and E_f^0 refer to the kinetic constant and the formal potential of each step; the values of k_0 and α for the first step are arbitrary to model a quasi-reversible behaviour.

Section 6: Oxygen Reduction Reaction on Silver in 0.1 M KCl and 0.42 M KCl

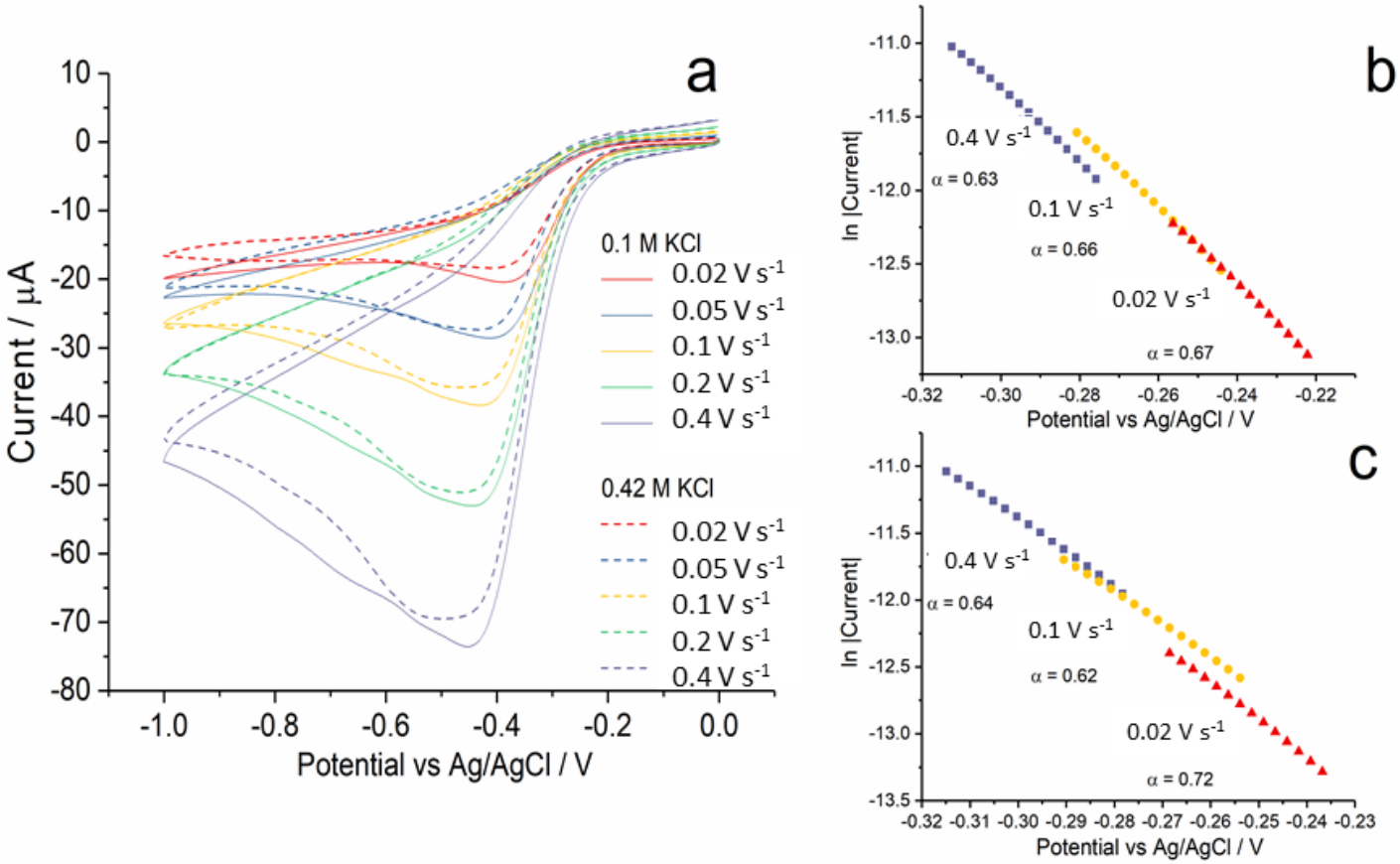


Figure A.6 ORR on silver in potassium chloride solutions a) Voltammagrams in oxygen saturated 0.1 M KCl and 0.42 M KCl with varying scan rates from 0.02 V s^{-1} to 0.4 V s^{-1} b) Tafel analysis for 0.1 M KCl c) Tafel analysis for 0.42 M KCl

Bibliography

1. H. M. A. Amin, Y. Uchida, E. Kätelhön and R. G. Compton, *J. Electroanal. Chem.*, 2019, **836**, 62-67.
2. F. M. M. Morel, J. G. Rueter, D. M. Anderson and R. R. L. Guillard, *J. Phycol.*, 2008, **15**, 135-141.
3. N. M. Price, G. I. Harrison, J. G. Hering, R. J. Hudson, P. M. V. Nirel, B. Palenik and F. M. M. Morel, *Biol. Oceanogr.*, 1989, **6**, 443-461.
4. F. J. Millero, R. Feistel, D. G. Wright and T. J. McDougall, *Deep Sea Res. Part I Oceanogr. Res. Pap.*, 2008, **55**, 50-72.
5. *CRC Handbook of Chemistry and Physics*, CRC Press, Boca Raton, 58 edn., 1977.
6. B. Jahne, G. Heinz and W. Dietrich, *J Geophys Res-Oceans*, 1987, **92**, 10767-10776.
7. D. M. Himmelblau, *Chem. Rev.*, 1964, **64**, 527-550.
8. M. Jamnongwong, K. Loubiere, N. Dietrich and G. Hébrard, *Chem. Eng. J.*, 2010, **165**, 758-768.
9. G. W. Hung and R. H. Dinius, *J. Chem. Eng. Data*, 1972, **17**, 449-451.

10. A. J. Vanstroe and L. J. J. Janssen, *Anal Chim Acta*, 1993, **279**, 213-219.
11. P. Han and D. M. Bartels, *J. Phys. Chem.* , 1996, **100**, 5597-5602.
12. C. Degrand, *J. Electroanal. Chem. Interf. Electrochem.*, 1984, **169**, 259-268.
13. N. Le Bozec, C. Compère, M. L'Her, A. Laouenan, D. Costa and P. Marcus, *Corros. Sci.*, 2001, **43**, 765-786.
14. M. Frank, *Nat. Geosci.*, 2011, **4**, 220-221.
15. H. Elderfield, *Nature*, 1983, **304**, 380-380.
16. Y. Wang, E. Laborda, K. R. Ward, K. Tschulik and R. G. Compton, *Nanoscale*, 2013, **5**, 9699-9708.
17. P. Singh and D. A. Buttry, *J. Phys. Chem. C*, 2012, **116**, 10656-10663.
18. R. E. Davis, G. L. Horvath and C. W. Tobias, *Electrochim. Acta*, 1967, **12**, 287-297.
19. L.-K. Ju and C. S. Ho, *Biotechnol. Bioeng.*, 1985, **27**, 1495-1499.
20. H. L. Clever, R. Battino, H. Miyamoto, Y. Yampolski and C. L. Young, *J. Phys. Chem. Ref. Data*, 2014, **43**.
21. K. Shimizu, L. Sepunaru and R. G. Compton, *Chem. Sci*, 2016, **7**, 3364-3369.
22. T. N. Das, *Ind. Eng. Chem. Res.*, 2005, **44**, 1660-1664.
23. M.-C. Pham and J.-E. Dubois, *J. Electroanal. Chem. Interf. Electrochem.*, 1986, **199**, 153-164.
24. M. Geng and Z. Duan, *Geochim. Cosmochim. Acta*, 2010, **74**, 5631-5640.

Appendix B

Section 1: The Calibration of the Silver Electrode

The silver electrode radius was evaluated using cyclic voltammetry of the two-electron reduction of oxygen. Experiments were conducted using variable scan rates from 20mV s^{-1} to 400mV s^{-1} at 298 K in oxygen saturated solution of pure 0.1M KNO_3 and analysed using the irreversible version of Randles–Ševčík equation (**Equation B.1**) and Tafel analysis. The variation of the peak current (I_p) with the square root of the scan rate (v):

$$I_p = 2.99 \times 10^5 n \sqrt{\alpha} {D_{O_2}}^{0.5} c_{O_2} A v^{0.5} \quad \textbf{(B.1)}[1]$$

where the number of electrons transferred is n = 2, the concentration of saturated dissolved oxygen[2] is $c_{O_2} = 1.26\ \text{mol}\, m^{-3}$, the diffusion coefficient of oxygen in solution[3] is $D_{O_2} = 1.96 \times 10^{-9}\ \text{m}^2\text{s}^{-1}$, the area of electrode is A (m^2). The transfer coefficient obtained at 20mVs^{-1} was α=0.78 from the Tafel plot in **Figure B.1 b**, in agreement with data in previous study[4]. The Tafel analysis was performed on the voltammetry section starting from 10% to 30% of the peak height. The term $2.99 \times 10^5 n \sqrt{\alpha} {D_{O_2}}^{0.5} C_{O_2} A$ was calculated from the slope of **Figure B.1** inset, giving the silver electrode radius of 1.13 mm, very close to the nominal radius of 1.0 mm.

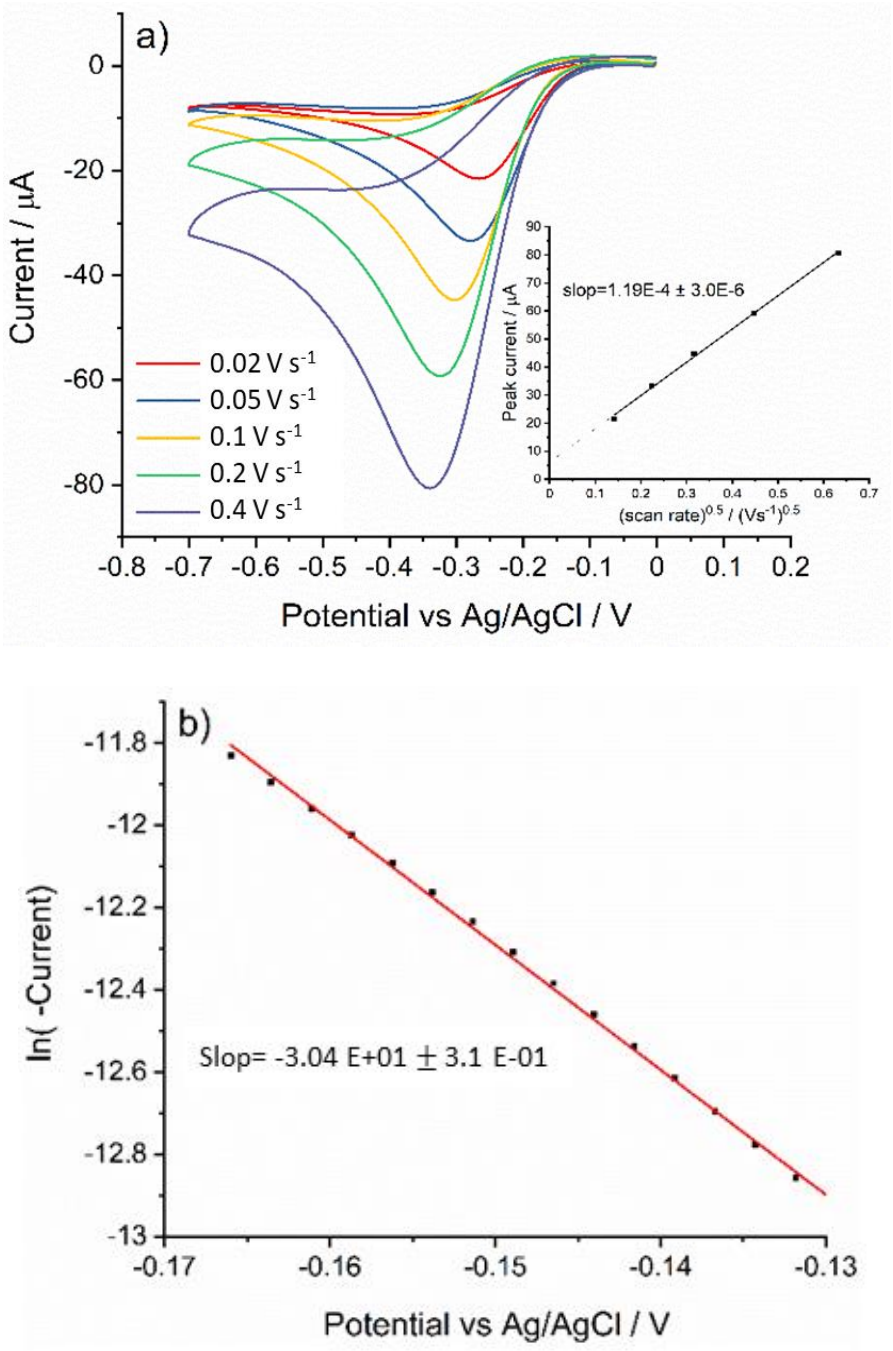


Figure B.1 Calibration of silver electrode in oxygen saturated 0.1M KNO_3 solution at 298 K. a) Voltammetry conducted at 0.02 Vs^{-1} to 0.4 Vs^{-1}, inset: scan rate dependency of the peak current. b) Tafel plot for data at 0.02 Vs^{-1}.

Section 2 Monolayer Peaks of Silver Chloride

Silver chloride monolayer was studied voltammetrically in nitrogen degassed 0.564 M NaCl solutions using a silver electrode. The electrode was first held at -1.0 V for 1min followed by scans from -0.15 V to +0.060 V with reversal at +0.060 V. The scan was conducted at a scanrate ranges from 0.02 Vs^{-1} to 0.4 V s^{-1}. Two peaks were observed, regarding the silver chloride monolayer formation at -0.025 V and stripping at -0.10 V. The peak current of the silver chloride monolayer formation signal is proportional to scanrates (**Figure B.2 a**, inset). The total formation charge of the monolayer was calculated via polynomial baseline subtractions (**Figure B.2 b**). For instance using the data in **Figure B.2 a**, 0.4 Vs^{-1}, the peak between point a and b was first removed from the full voltammogram. Next, a polynomial fitting was conducted on the remaining data (-0.15V to point a, and point b to -0.050V). Then, the fitted polynomial data was subtracted from raw data at 0.4 Vs^{-1} (**Figure B.2 b**). The actual charge of oxidation peaks was calculated as 1.2±0.1μC cm^{-2} via integration of current from -0.10V to +0.060V, consistent with the literature reported by Jaya *et al*. (4.62μC cm^{-2})[5].

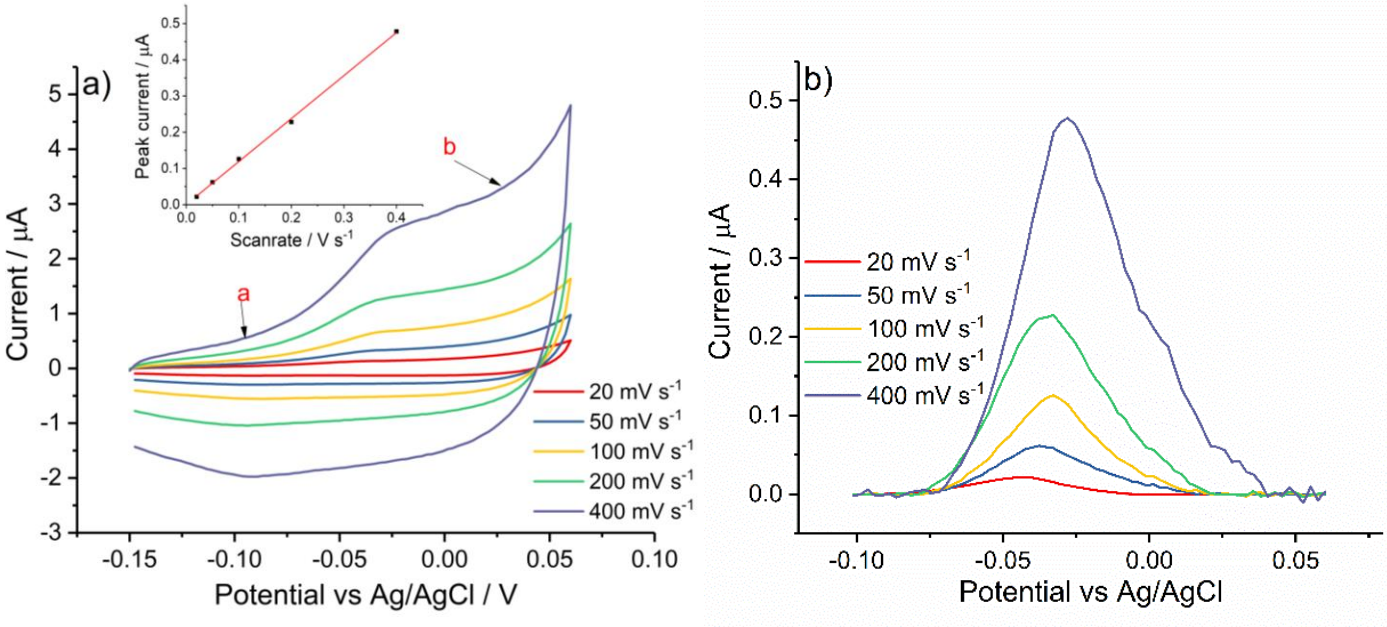


Figure B.2 Scan rate dependency of silver chloride monolayer peaks. a) Raw data with peak current to scanrate dependency in the inset. b) Baseline subtracted data.

Section 3 The Superoxide Peak Studied in Synthetic Seawater

The stability of the superoxide peak in synthetic seawater with chloride concentrations in the range from 0.484M to 0.593M was analysed (**Figure 5.6** in **Chapter 5**). The voltammetry was conducted at 0.02 Vs^{-1} scanning from -0.20V to -1.0V, then scanned positively to +0.1V before returning to -0.2V. Each experiment was repeated four times for every concentration. The superoxide peak was observed at -0.39±0.01V with a peak height of 2.51±0.08μA. Within the range of 0.484 M to 0.624 M both peak potential and peak current of the superoxide feature are almost unchanged, thus the superoxide peak can be used as a stable internal reference potential

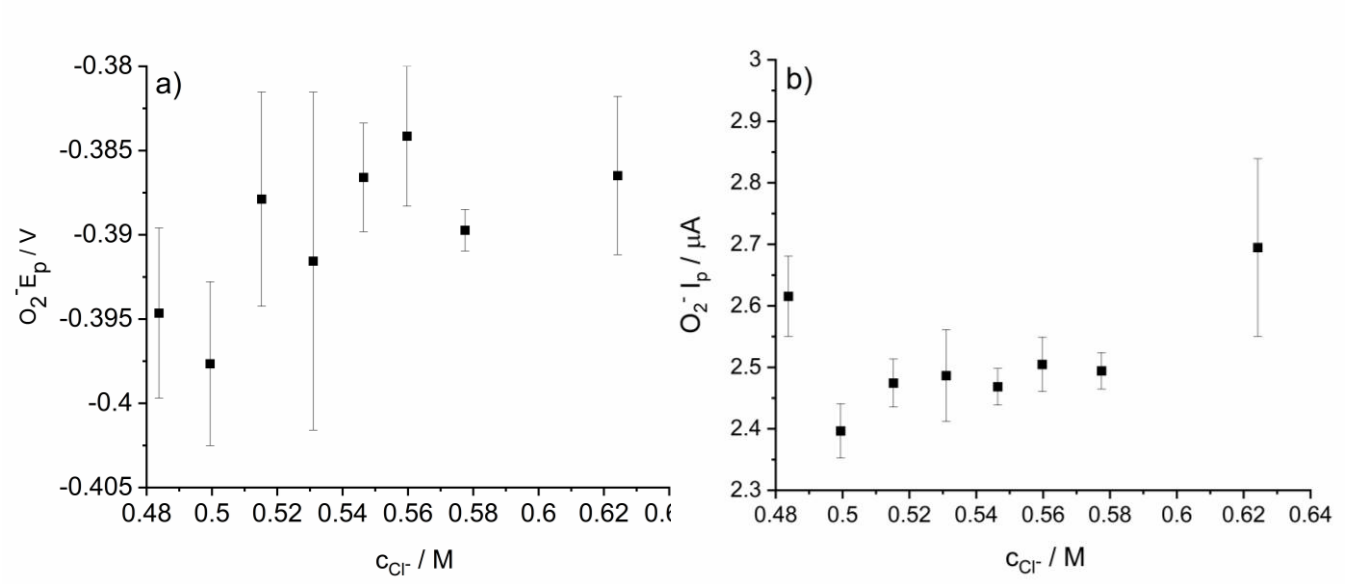


Figure B.3 The superoxide peak in synthetic seawater with the chloride concentration ranges from 0.484 M to 0.624 M a) Peak potentials. b) Peak currents.

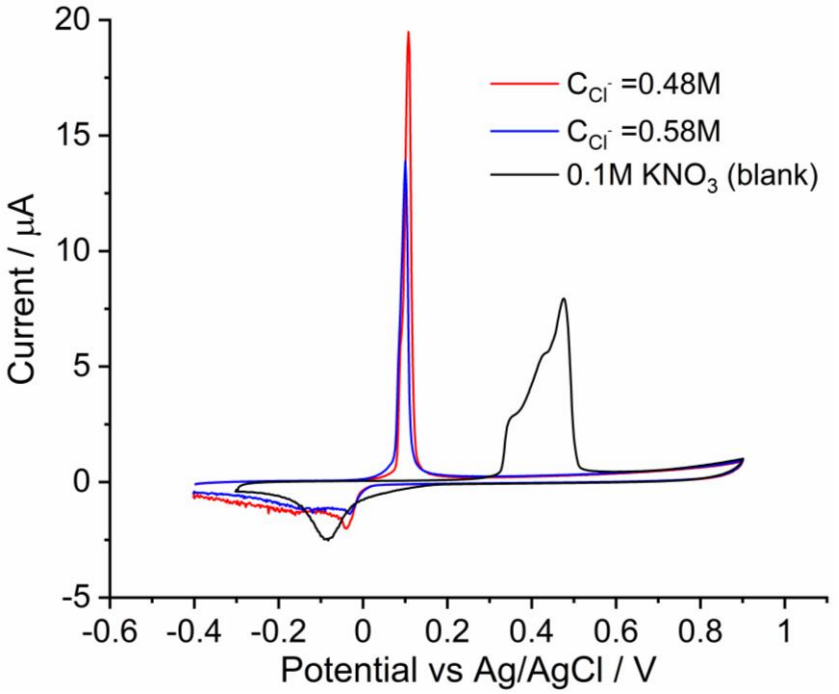


Figure B.4 Detection of chloride with silver nanoparticles in nitrogen saturated synthetic seawater solutions.

Bibliography

1. R. G. Compton and C. E. A Banks, *Understanding Voltammetry*, 2nd edn., 2010.
2. K. Shimizu, L. Sepunaru and R. G. Compton, *Chem. Sci*, 2016, **7**, 3364-3369.
3. C. C. M. Neumann, E. Laborda, K. Tschulik, K. R. Ward and R. G. Compton, *Nano Research*, 2013, **6**, 511-524.
4. Y. J. Guo, M. J. Yang, R. C. Xie and R. G. Compton, *Chem. Sci.*, 2021, **12**, 397-406.
5. S. Jaya, T. P. Rao and G. P. Rao, *J. Appl. Electrochem.*, 1987, **17**, 635-640.

Appendix C

Section 1 The Superimposed Voltammetry

Herein the model with variable supporting ratio is compared to the diffusion only model, the supporting concentration of the former is set 10000 times that of the analyte.

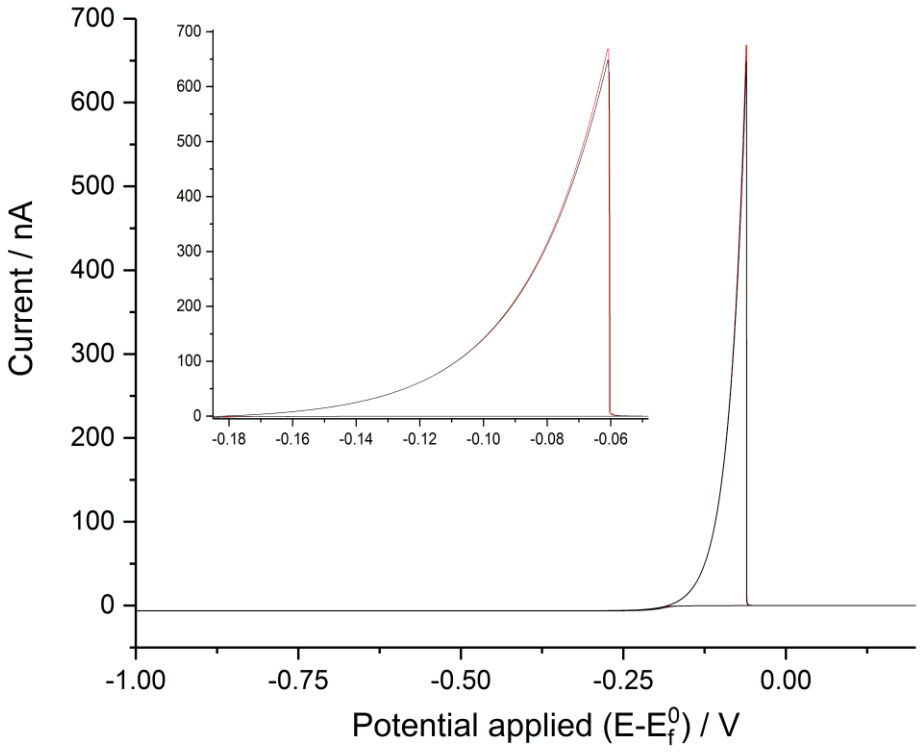


Figure C.1 Simulation of the voltammetric response for the cathodic deposition and stripping of a mono-valent cation (1 mM) at a 10 μm hemisphere electrode. Scan rate =0.01 V s^{-1}, 298K, all diffusion coefficients are equal with a value of D=1×10^{-9} m^2s^{-1}. Red line represents voltammetry for diffusion only model, Black line represents voltammetry with 1M supporting electrolyte.

Figure C.1 presents an overlaid diagram showing the cathodic deposition and stripping of a mono-valent cation by diffusion-only model (red line) and a full *Nernst-Planck-Poisson*

simulation using a high support ratio condition (black line). The good agreement between these two simulations evidences that at high support ratios, that the entire voltammetry is well described by a diffusion only mass-tranport model.

The simulation studied 1mM mono-valent cation and 10 μm hemisphere electrode with a scan rate of 0.01 Vs^{-1}. Diffusion coefficients are equal with a value of $D=1x10^{-9}$ m^2s^{-1} for the cyclic voltammetry under 298 K. Further details of the used simulation model used are provided in the **Chapter 6**.

Section 2 The Simulation Stripping Peak Potential Variation under Different Support Ratios

In **Chapter 6** the transition between the high and low support regimes is quantified by studying the magnitude of the mass-transport limited steady-state reductive current. However, other characteristics parameters relating to the voltammetry can be used to quantify the transition between these two regimes. Here for example, the position of the anodic stripping wave as a function of the supporting electrolyte concentration was studied. **Figure C.2** shows four analyte cation concentrations (0.1-4 mM) and shows that the shift of the voltammetric stripping peak position can be used to quantify the extent to which migration is influencing the voltammetric response. Note to enable direct comparison of this data the change in the equilibrium potential for the redox process as a function of the analyte concentration had to be accounted for. Difference in the cation concentration has negligible effect on the relative peak variation, and within the diffusion only region, the relative peak potential is stabilized.

The simulation studied 1 mM mono-valent cation and 10 µm hemisphere electrode with a scan rate of 0.01 Vs^{-1}. Diffusion coefficients are equal with a value of D =1×10^{-9} m^2s^{-1} for the cyclic voltammetry under 298 K. Four cation concentrations were used, which are 0.1mM (black), 0.4mM (red), 1mM (blue) and 4mM (yellow). The simulation model used is provided in **Chapter 6**.

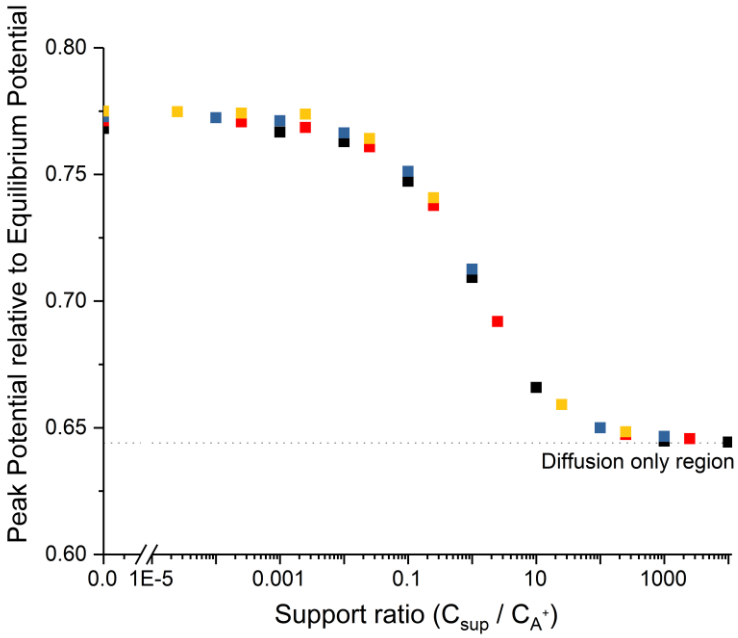


Figure C.2 Simulation stripping peak potential of a mono-valent cation (1 mM) at a 10 µm hemisphere electrode as a function of support ratio (c_{sup} / c_{A^+}). Scan rate =0.01 Vs^{-1}, 298K, all diffusion coefficients are equal with a value of D=1×10^{-9} m^2s^{-1}, c_{sup} refers to supporting electrolyte concentration and c_{A^+} refers to the analyte concentration, both in mol dm^{-3}. Four concentrations of A are simulated, black scatter (0.1mM), red scatter (0.4mM), blue scatter (1mM) and yellow scatter (4mM)